UNIVERSITAT POLITÈCNICA DE VALÈNCIA

DEPARTAMENTO DE COMUNICACIONES

PhD Dissertation

DESIGN OF MICROWAVE FILTERS AND MULTIPLEXERS IN WAVEGUIDE TECHNOLOGY USING DISTRIBUTED MODELS

Departamento de Comunicaciones

Universidad Politécnica de Valencia

Author
María Brumos Vicente

Supervisors
Dr. Vicente E. Boria Esbert
Dr. Santiago Cogollos Borrás

Valencia, December 2014

DESIGN OF MICROWAVE FILTERS AND MULTIPLEXERS IN WAVEGUIDE TECHNOLOGY USING DISTRIBUTED MODELS

DESIGN OF MICROWAVE FILTERS AND MULTIPLEXERS IN WAVEGUIDE TECHNOLOGY USING DISTRIBUTED MODELS

María Brumos Vicente
Universidad Politécnica de Valencia

CONTENTS

ABSTRACT

This thesis introduces new design techniques for microwave filters and multiplexers in waveguide technology. These devices find wide application in communication systems, such as satellite links or wireless base stations.

In particular, the work has been focused in the design of circular-waveguide dual-mode (CWDM) filters. The synthesis technique makes use of distributed models, which are a halfway point between the fast but imprecise lumped circuit models, and the more accurate but costly full-wave electromagnetic models. An automatic software tool to design this type of filters has also been developed, which is able to obtain the physical dimensions of the filter in a matter of minutes.

A new technique to correct manufacturing deviations in CWDM filters is proposed next, which avoids the use of tuning screws. Instead, fixed squared insertions are employed, which can be fabricated in separated pieces. An space mapping technique is used to calculate the dimensions of these pieces and, after few iterations, the procedure is able to achieve the required response.

A systematic method to design manifold-coupled multiplexers is also presented, which also employs distributed models. First, the design of classic multiplexers with CWDM filters is considered. The whole design procedure is thoroughly explained, starting from the required specifications and finishing with the physical dimensions. Finally, the design of a non-conventional wideband multiplexer with a new type of rectangular-waveguide filters is addressed.

RESUMEN

Esta tesis presenta nuevas técnicas de diseño de filtros y multiplexores en guía de ondas. Estos dispositivos son ampliamente utilizados en sistemas de comunicaciones, tales como enlaces por satélite o estaciones base inalámbricas.

En concreto, el trabajo se centra en el diseño de filtros de modo dual (FMD) en guía circular. La técnica de síntesis hace uso de modelos distribuidos, que constituyen un punto intermedio entre los rápidos pero imprecisos modelos de elementos concentrados, y los más exactos pero costosos (en términos computacionales) modelos electromagnéticos. Se ha diseñado una herramienta software capaz de obtener de manera automática las dimensiones físicas del filtro en cuestión de minutos.

Además, se ha propuesto una nueva técnica de corrección de errores de fabricación en FMD en guía circular, que evita el uso de tornillos de sintonía. Éstos son sustituidos por inserciones metálicas fijas, que se fabrican en piezas separadas. El método emplea técnicas de mapeado espacial para calcular las dimensiones de estas piezas y, tras pocas iteraciones, es posible recuperar la respuesta deseada.

A continuación se presenta un procedimiento sistemático de diseño de multiplexores tipo "manifold" (colector). En primer lugar se considera el diseño de multiplexores clásicos con FMD, explicando con detalle el proceso de diseño, partiendo de las especificaciones requeridas y concluyendo con la obtención de las dimensiones físicas. Por último, se aborda el diseño de un multiplexor de banda ancha con un nuevo tipo de filtros en guía rectangular.

RESUM

Aquesta tesi presenta noves tècniques de disseny de filtres i multiplexors en guia d'ones. Aquests dispositius són àmpliament utilitzats en sistemes de comunicacions, com ara enllaços per satèl·lit o estacions base sense fils.

En concret, el treball se centra en el disseny de filtres de mode dual (FMD) en guia circular. La tècnica de síntesi fa ús de models distribuïts, que constitueixen un punt intermedi entre els ràpids però imprecisos models d'elements concentrats, i els més exactes però costosos (en termes computacionals) models electromagnètics. S'ha dissenyat una eina software capaç d'obtenir de manera automàtica les dimensions físiques del filtre en qüestió de minuts.

A més, s'ha proposat una nova tècnica de correcció d'errors de fabricació en FMD en guia circular, que evita l'ús de cargols de sintonia. Aquests són substituïts per insercions metàl·liques fixes, que es fabriquen en peces separades. El mètode empra tècniques de mapejat espacial per calcular les dimensions d'aquestes peces i, després de poques iteracions, és possible recuperar la resposta desitjada.

A continuació es presenta un procediment sistemàtic de disseny de multiplexors tipus "manifold" (col·lector). En primer lloc es considera el disseny de multiplexors clàssics amb FMD, explicant amb detall el procés de disseny, partint de les especificacions requerides i concloent amb l'obtenció de les dimensions físiques. Finalment, s'aborda el disseny d'un multiplexor de banda ampla amb un nou tipus de filtres en guia rectangular.

CHAPTER 1

INTRODUCTION

This first chapter is devoted to an overview of the main subjects considered in this thesis. Some basic concepts such as microwave filters and multiplexers are presented, noting the great importance of these devices in satellite communications systems. A particular type of microwave filter, the circular-waveguide dual-mode (CWDM) filter, is introduced, and the state of the art related to its design is reviewed. The waveguide manifold-coupled multiplexer, which is the multiplexer configuration in which this thesis is focused, is also introduced, going through the main existing design methods. An outline of the rest of this thesis can also be found at the end of the chapter.

Design of microwave filters and multiplexers in waveguide technology using distributed models.
By María Brumos Vicente, Universidad Politécnica de Valencia.

1.1 Microwave Filters and Multiplexers

Microwave filters and multiplexers find wide application in communication systems, such as satellite links or wireless base stations [1]. Microwave filters are passive devices employed to select a specific band of the frequency spectrum. Depending on the spectral region that is selected or rejected, they are classified in low-pass filters, high-pass filters, band-pass filters or band-stop filters. Multiplexers are composed of a certain number of filters, and they are used to split a wideband signal into different channels, or to combine various individual channels to form a multi-channel signal.

In satellite communications, multiplexers are typically employed to split the signal that reaches the satellite, so each channel can be amplified separately. The signals coming from the amplifiers are then combined by an output multiplexer for being retransmitted back to the Earth. Passive devices at the output stage of the satellite communication system must be able to deal with very high power signals. Because of that, waveguide technology is the ideal choice to implement these devices. The purpose of this thesis is to design waveguide filters and multiplexers in an efficient way.

1.2 Circular-Waveguide Dual-Mode Filters

This work has been focused on the design of a particular type of waveguide filter: the circular-waveguide dual-mode (CWDM) filter. These filters are widely used as channel filters in output multiplexers (OMUX) of communication satellite payload systems, due to their compact size, high unloaded quality factor, and flexibility in realizing various required cross-couplings [2], [3]. Since its birth at ComSat Laboratories more than 40 years ago, in response to very stringent performance requirements upon spacecraft microwave equipment, the CWDM filter has become a very important device for implementing OMUXes, mainly at Ku and Ka frequency bands.

1.2.1 Physical Structure and Operation

A CWDM filter is composed of a series of circular waveguide cavities connected through cruciform irises. Figure 1.1 shows the physical structure of a CWDM filter with two cavities. Two orthogonal electromagnetic modes coexist inside each cavity. Indeed, this is the reason why dual-mode filters are more compact (approximately twice) than classic in-line filters, where there is only one excited mode per cavity. Dual-mode filters only need N cavities to produce a 2N-pole filter response.

In order to explain how these filters work, let us consider a two-cavity filter like the one shown in Fig. 1.1. The horizontal input/output irises couple the vertical mode coming through the input/output waveguide with the vertical mode of the circular cavity. The vertical mode in the circular cavity is coupled with the horizontal mode thanks to the oblique screw placed in the middle of the cavity. The horizontal arm of the cross-shaped iris connects the vertical modes of both cavities, while the horizontal modes are coupled through the vertical arm. The vertical and horizontal

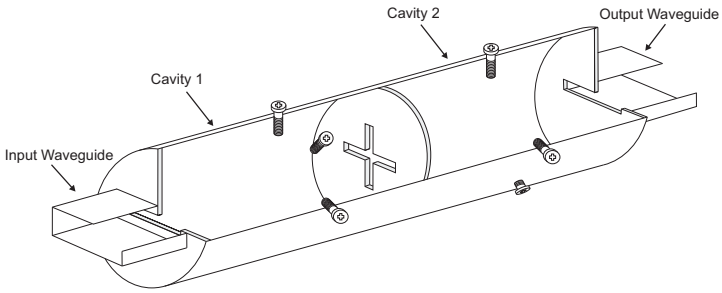

Figure 1.1 Physical structure of a circular-waveguide dual-mode filter.

screws are used to adjust the center frequencies of the vertical and horizontal modes, respectively.

1.2.2 Design of Circular-Waveguide Dual-Mode Filters: State of the Art

The design technique for CWDM filters presented in this work makes use of distributed models, which were originally developed by Cohn [4], and have been applied to the design of single-mode filters in both waveguide and planar technologies [5]. Even though equivalent circuits based on lumped elements are very well suited for the synthesis of narrowband filters [3, 6], distributed models (traditionally composed of inverters and transmission-line resonators) are used in many other practical applications [7–9]. Distributed models have shown very good reliability for dealing with broadband structures, since they can consider the frequency-dependence behavior of real waveguide inverters [10–12], as well as the periodic behavior of the transmission lines and their dispersion.

The most popular methods for the accurate design of single-mode bandpass filters based on equivalent distributed models typically follow one of the two strategies explained below:

- **Stage by stage optimization:** A very flexible procedure, where the electromagnetic (EM) response of a single stage of the filter (i.e., a cavity with its input and output irises) is optimized to match the response of the distributed model representing the same structure [13].

- **Inverse search:** This method is based on a root-seeking routine, which allows to find the physical dimensions of the real structures that match (at certain frequency) the inverter values of the distributed model [14]. In this procedure, the inverter values provided by the corresponding physical structures are derived from EM simulations.

Dual-mode filters have been conventionally designed through coupling matrices (CM), which is equivalent to make use of polynomials or lumped-element circuits [3, 6]. Recently, and with the aim of easing the design procedure of these filter

implementations, more advanced circuit models (some of them including transmission lines) have been reported [15–19]. Even though they can provide better initial solutions, some iterative or optimization-based adjustments are typically needed for recovering the response specifications.

With the recent advent of more powerful EM analysis codes, substantial efforts have been devoted to replace the conventional dual-mode filters (essentially their required tuning and coupling screws) by alternative configurations based on simpler waveguide geometries. For example, new approaches for designing dual-mode rectangular waveguide filters with distributed coupling elements, realized through almost square waveguides with either square-corner cuts [20] or rotated by 45^{o} [21], were proposed. Alternatively, it has been also proved that the tuning and coupling functions (traditionally implemented with screws) can be accomplished through short sections of rectangular waveguides with square-corner cuts [22], short rotated rectangular waveguides [23], and with off-centered circular irises [24], all of them placed in the middle of the dual-mode resonant cavities.

The computer-aided design (CAD) procedure proposed in this thesis is able to systematically design dual-mode filters, with tuning and coupling screws. The design procedure is based on a complete distributed model, which is closely related to the physical geometry of the CWDM filter to be designed [25]. This model is able to account for all required couplings of the filter, which are accurately modeled through adequate K- and J-inverters included in the same equivalent circuit. Once the values of such inverters are derived from the corresponding elements of the standard CM representation, the distributed model is used as an intermediate reference to determine the geometrical dimensions of all irises and screws of the dual-mode filter.

1.3 Waveguide Manifold-Coupled Multiplexers

In this thesis, the design of multiplexers in waveguide technology has been considered. There are several possible configurations for implementing microwave multiplexers [1, 26, 27]. Some of them make use of hybrids or circulators, which provide a high isolation between filters resulting in a relatively easy design and tuning process. However, these configurations also have some drawbacks. First of all, these combining elements introduce losses. Furthermore, these devices are quite bulky, which is always an issue for satellite payloads. Manifold-coupled multiplexers, on the other hand, are preferable in terms of both size and performance [27–29], since they use a simple common waveguide to connect all the filters. Unfortunately, the design and tuning process can be extremely difficult, due to the strong interaction between different channels [27, 28, 30]. This leads to a design process of the structure as a whole, which commonly involves a huge number of variables to be considered at the same time.

1.3.1 Physical Structure and Operation

A manifold-coupled multiplexer is composed of a certain number of channel filters connected through a core waveguide called manifold. Figure 1.2 shows a typical scheme of a waveguide manifold-coupled multiplexer with 5 channel filters.

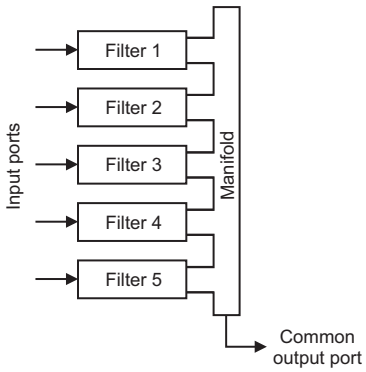

Figure 1.2 Structure of a waveguide manifold-coupled multiplexer with 5 channel filters.

Figure 1.2 corresponds to an output multiplexer, where 5 individual narrowband channels are combined to form a wideband signal. The signals coming from the input ports are filtered by the 5 channel filters, to eliminate undesired out-of-band signal components. Then, the filtered signals are combined inside the manifold and the multi-channel signal comes out through the output common port, usually connected to an antenna system.

The same multiplexer could be used as an input multiplexer. In this case, the multi-channel signal enter the multiplexer through the common port, and the manifold guides this signal to all the filters. Each filter selects the corresponding band of the multi-channel signal, and the individual channel signals come out from each filter through the 5 output ports.

There are several configuration schemes, depending on the position of the filters along the manifold. Three common manifold multiplexer configurations are shown in Figure 1.3, with all channel filters connected to one side of the manifold (comb), to both sides (herringbone), and end-fed (applicable to either of the first two), in which one channel filter is connected at the end of the manifold.

Figure 1.4 shows a real fabrication of a Ku-band 19-channel multiplexer employing a waveguide manifold [27]. The channel filters are CWDM filters. As it can be seen, it presents a herringbone configuration with 10 channel filters on one side, and 9 channel filters on the other side.

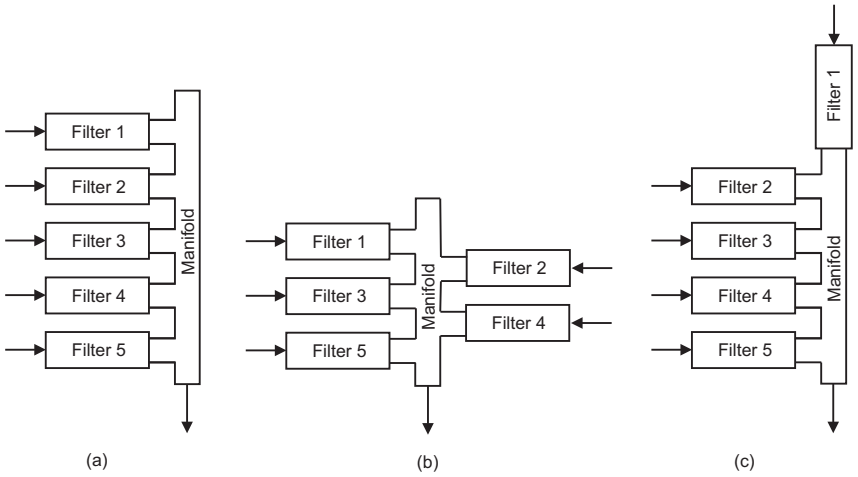

Figure 1.3 Common configurations for manifold multiplexers: (a) comb, (b) herringbone, and (c) one filter feeding directly into the manifold.

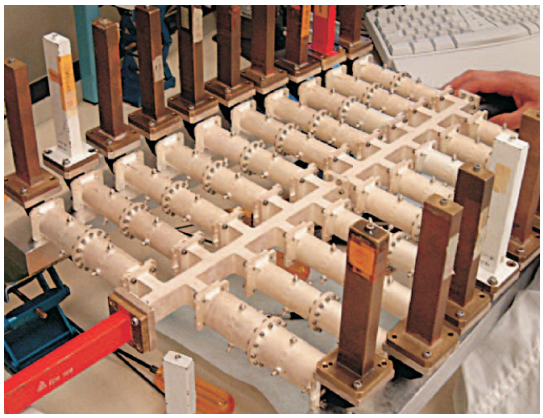

Figure 1.4 A 19-channel Ku-band waveguide multiplexer with CWDM filters [27].

1.3.2 Design of Waveguide Manifold-Coupled Multiplexers: State of the Art

The design of multiplexing networks is particularly important in satellite applications. For example, an increase in the insertion loss of the channel filters in an output multiplexer results in a reduction of the Effective Isotropic Radiated Power (EIRP) emitted by the satellite, and accordingly a reduction in the amount of radio frequency (RF) transmission power. Rejection between channels must be able to remove the high frequency harmonics generated by the power amplifiers that are connected at the input ports of the filters. For space applications, a multiplexer must

comply with stringent RF in-band and out-of-band characteristics, such as passband gain, group delay flatness and stopband rejection. These devices must also be able to cope with a wide environmental temperature range, while dealing with high power input signals [31].

In manifold-coupled multiplexers, the virtually lossless direct connection of channels through the common transmission line, and the large number of design variables involved, make the design of multiplexing networks difficult. Interactions among channel filters need to be taken into account in order to achieve channel performance close to a stand-alone filter [27, 28, 30, 32].

Multiplexers have been conventionally designed using analytical models for the channel filters, such as the CM approach [3, 28]. Some techniques have also been developed to obtain a good initialization for the manifold dimensions in the circuit model [33]. However, these models do not take into account many effects of the real structure, which normally leads to a deficient starting point in the EM model, thus commonly requiring a cumbersome and time-consuming optimization driven by a skilled designer. In order to achieve a more realistic prototype, hybrid procedures have been introduced, where some parts of the structure are replaced with full-wave electromagnetic (EM) models [34–36]. Alternatively, space mapping techniques (linking circuital models with full-wave EM simulations) have also been used [27, 37–39]. The aim of all these techniques is to compensate the weaknesses of the traditional circuit models, in order to design a real multiplexer in a more efficient way.

This thesis is focused on the design of manifold multiplexers with CWDM filters, even though it could be extended to multiplexers with other type of channel filters. The procedure presented uses a distributed model of the individual filters, which allows to fill the gap between the lumped model based on the CM, and the EM model. The main advantage of the distributed model is that it can take into account not only the periodic behavior of the transmission lines included in the model, but also the modal dispersion of the fundamental mode. An efficient systematic technique to design that kind of multiplexers has been developed, which starts from the frequency specifications and finishes with the physical dimensions of the whole multiplexer.

1.4 Thesis Outline

The rest of the thesis report is organized as follows:

- Chapter 2 presents a new design technique for CWDM filters, which makes use of distributed models. It comprehensively explains the whole design method for different filter orders and configurations, giving also some design examples.
- Chapter 3 provides an alternative method to correct manufacturing deviations in waveguide filters, without using tuning screws. The technique is particularized for CWDM filters, but could be easily extended to other filter configurations.
- Chapter 4 describes a systematic design method for manifold multiplexers with CWDM filters. It extends the design technique developed for individual filters,

so it can take into account the interactions between different channels. Design examples of both contiguous and non-contiguous channel multiplexers are provided.

- Chapter 5 accomplishes the design of a non-conventional wideband multiplexer, with a new topology of rectangular waveguide filters, to be employed as part of a test bed to measure passive intermodulation effects. The designed device has been manufactured, and its measured performance validates the proposed design technique.
- In chapter 6, the main conclusions of the work are summarized and discussed, and some suggestions for future work are proposed.
- Appendix A describes an automatic design tool for CWDM filters, which has been successfully incorporated into the commercial EM solver FEST3D [40]. The algorithm uses the synthesis technique introduced in chapter 2.
- In appendix B, the procedure to design doubly and singly terminated filter networks is outlined, starting from the filter specifications and finishing with the synthesis of the required coupling matrix, which is the starting point to design the filters considered in chapters 2 and 4.
- Finally, appendix C contains a list of publications covering the most relevant research merits achieved along this thesis work.

REFERENCES

1. R.J. Cameron, C.M. Kudsia, and R.R. Mansour. *Microwave Filters for Communication Systems: Fundamentals, Design and Applications*. Wiley, 2007.
2. A.E. Atia and A.E. Williams. New types of waveguide bandpass filters for satellite transponders. In *Comsat Tech. Rev.*, volume 1, pages 21–43, Fall 1971.
3. A.E. Atia and A.E. Williams. Narrow-bandpass waveguide filters. In *Microwave Theory and Techniques, IEEE Transactions on*, volume 20, pages 258–265, Apr 1972.
4. S. B. Cohn. Direct-coupled-resonator filters. In *Proceedings of the IRE*, volume 45, pages 187–196, Feb 1957.
5. G.L. Matthaei, L. Young, and E.M.T. Jones. *Microwave Filters, Impedance-Matching Networks, and Coupling Structures*. Artech House. McGraw-Hill, 1964.
6. A.E. Atia, A.E. Williams, and R.W. Newcomb. Narrow-band multiple-coupled cavity synthesis. In *Circuits and Systems, IEEE Transactions on*, volume 21, pages 649–655, Sep 1974.
7. L. Young. Direct-coupled cavity filters for wide and narrow bandwidths. In *Microwave Theory and Techniques, IEEE Transactions on*, volume 11, pages 162–178, May 1963.
8. J.D. Rhodes. The generalized direct-coupled cavity linear phase filter. In *Microwave Theory and Techniques, IEEE Transactions on*, volume 18, pages 308–313, Jun 1970.
9. J.D. Rhodes. *Theory of Electrical Filters.* Wiley, 1976.
10. R. Levy. Theory of direct-coupled-cavity filters. In *Microwave Theory and Techniques, IEEE Transactions on*, volume 15, pages 340–348, Jun 1967.

11. F.M. Vanin, D. Schmitt, and R. Levy. Dimensional synthesis for wide-band waveguide filters and diplexers. In *Microwave Theory and Techniques, IEEE Transactions on*, volume 52, pages 2488–2495, Nov 2004.

12. P. Soto, E. Tarín, V.E. Boria, C. Vicente, J. Gil, and B. Gimeno. Accurate synthesis and design of wideband and inhomogeneous inductive waveguide filters. In *Microwave Theory and Techniques, IEEE Transactions on*, volume 58, pages 2220–2230, Aug 2010.

13. M. Guglielmi. Simple CAD procedure for microwave filters and multiplexers. In *Microwave Theory and Techniques, IEEE Transactions on*, volume 42, pages 1347–1352, Jul 1994.

14. L.Q. Bui, D. Ball, and T. Itoh. Broad-band millimeter-wave E-plane bandpass filters (short papers). In *Microwave Theory and Techniques, IEEE Transactions on*, volume 32, pages 1655–1658, Dec 1984.

15. J.R. Montejo-Garai and J. Zapata. Full-wave design and realization of multicoupled dual-mode circular waveguide filters. In *Microwave Theory and Techniques, IEEE Transactions on*, volume 43, pages 1290–1297, Jun 1995.

16. W. Hauth, D. Schmitt, and M. Guglielmi. Accurate modelling of narrow-band filters for satellite communications. In *Microwave Symposium Digest. 2000 IEEE MTT-S International*, volume 3, pages 1767–1770, June 2000.

17. H. Hu and K.L. Wu. An automated design technique for asynchronously-tuned circular waveguide dual-mode filters. In *Microwave Conference Proceedings (APMC), 2010 Asia-Pacific*, pages 1970–1973, Dec 2010.

18. H. Hu, K.L. Wu, and R.J. Cameron. A design technique for stepped circular waveguide dual-mode filters for broadband contiguous multiplexers. In *Microwave Symposium Digest (MTT), 2011 IEEE MTT-S International*, pages 1–4, June 2011.

19. M. Bekheit, S. Amari, and F. Seyfert. A new approach to canonical dual-mode cavity filter design. In *Microwave Theory and Techniques, IEEE Transactions on*, volume 57, pages 1196–1206, May 2009.

20. X.P. Liang, K.A. Zaki, and A.E. Atia. Dual mode coupling by square corner cut in resonators and filters. In *Microwave Theory and Techniques, IEEE Transactions on*, volume 40, pages 2294–2302, Dec 1992.

21. P. Savi, D. Trinchero, R. Tascone, and R. Orta. A new approach to the design of dual-mode rectangular waveguide filters with distributed coupling. In *Microwave Theory and Techniques, IEEE Transactions on*, volume 45, pages 221–228, Feb 1997.

22. J.F. Liang, X.P. Liang, K.A. Zaki, and A.E. Atia. Dual-mode dielectric or air-filled rectangular waveguide filters. In *Microwave Theory and Techniques, IEEE Transactions on*, volume 42, pages 1330–1336, Jul 1994.

23. L. Accatino, G. Bertin, and M. Mongiardo. A four-pole dual mode elliptic filter realized in circular cavity without screws. In *Microwave Theory and Techniques, IEEE Transactions on*, volume 44, pages 2680–2687, Dec 1996.

24. K.L. Wu. An optimal circular-waveguide dual-mode filter without tuning screws. In *Microwave Theory and Techniques, IEEE Transactions on*, volume 47, pages 271–276, Mar 1999.

25. S. Cogollos, M. Brumos, V.E. Boria, C. Vicente, J. Gil, B. Gimeno, and M. Guglielmi. A systematic design procedure of classical dual-mode circular waveguide filters using an

equivalent distributed model. In *Microwave Theory and Techniques, IEEE Transactions on*, volume 60, pages 1006–1017, April 2012.

26. C.M. Kudsia, J. Dorey, J. Heierli, K. R. Ainsworth, and G. J P Lo. A new type of low loss l4 GHz high power combining network for satellite earth terminals. In *Microwave Conference, 1979. 9th European*, pages 386–391, Sept 1979.
27. R.J. Cameron and M. Yu. Design of manifold-coupled multiplexers. In *Microwave Magazine, IEEE*, volume 8, pages 46–59, 2007.
28. A.E. Atia. Computer-aided design of waveguide multiplexer (short papers). In *Microwave Theory and Techniques, IEEE Transactions on*, volume 22, pages 332–336, 1974.
29. C. Kudsia, K. Ainsworth, and M. O'Donovan. Microwave filters and multiplexing networks for communication satellites in the 1980s. In *Proc. AIAA 8th Communications Satellite Systems Conf.*, Apr 1980.
30. J.D. Rhodes and R. Levy. Design of general manifold multiplexers. In *Microwave Theory and Techniques, IEEE Transactions on*, volume 27, pages 111–123, Feb 1979.
31. S. Lundquist, M. Mississian, M. Yu, and D. Smith. Application of high power output multiplexers for communications satellites. In *Proc. 18th AIAA Int. Commun. Satellite Syst. Conf. Exhibit*, 2000.
32. C. Kudsia, R. Cameron, and Wai-Cheung Tang. Innovations in microwave filters and multiplexing networks for communications satellite systems. In *Microwave Theory and Techniques, IEEE Transactions on*, volume 40, pages 1133–1149, 1992.
33. A. Morini, T. Rozzi, and M. Morelli. New formulae for the initial design in the optimization of T-junction manifold multiplexers. In *Microwave Symposium Digest, 1997 IEEE MTT-S International*, volume 2, pages 1025–1028, June 1997.
34. L. Accatino and M. Mongiardo. Hybrid circuit-full-wave computer-aided design of a manifold multiplexers without tuning elements. In *Microwave Theory and Techniques, IEEE Transactions on*, volume 50, pages 2044–2047, 2002.
35. Y. Wang, S. Li, and M. Yu. Hybrid models for effective design and optimization of large-scale multiplexing networks. In *Microwave Theory and Techniques, IEEE Transactions on*, volume 61, pages 1839–1849, 2013.
36. D. Bariant, S. Bila, D. Baillargeat, S. Verdeyme, P. Guillon, D. Pacaud, and J.-J. Herren. Method of spurious mode compensation applied to manifold multiplexer design. In *Microwave Symposium Digest, 2002 IEEE MTT-S International*, volume 3, pages 1461–1464 vol.3, June 2002.
37. M.A. Ismail, D. Smith, A. Panariello, Y. Wang, and M. Yu. EM-based design of large-scale dielectric-resonator filters and multiplexers by space mapping. In *Microwave Theory and Techniques, IEEE Transactions on*, volume 52, pages 386–392, 2004.
38. M. Yu and Y. Wang. Synthesis and beyond. In *Microwave Magazine, IEEE*, volume 12, pages 62–76, Oct 2011.
39. M.A. Ismail, Y. Wang, and M. Yu. Advanced design and optimization of large scale microwave devices. In *Microwave Symposium Digest (MTT), 2012 IEEE MTT-S International*, pages 1–3, June 2012.
40. FEST3D 6.8.4 Aurora Software and Testing, S.L. (on behalf of ESA/ESTEC), Valencia, Spain, 2013. Available: www.fest3d.com.

CHAPTER 2

DESIGN OF CIRCULAR-WAVEGUIDE DUAL-MODE FILTERS USING DISTRIBUTED MODELS

This chapter explains a design method for circular-waveguide dual-mode (CWDM) filters [1, 2]. Starting from the filter specifications, the first step is to synthesize a lumped model composed of LC resonators and ideal inverters. This model is transformed into a distributed model with transmission lines, which constitutes a halfway point between the lumped model and the more accurate electromagnetic (EM) model. The values of the elements of the distributed model are employed to finally obtain the physical dimensions of the real filter. The proposed technique is applied to design filters with different orders, and the obtained results are here presented.

Design of microwave filters and multiplexers in waveguide technology using distributed models.
By María Brumos Vicente, Universidad Politécnica de Valencia.

2.1 Background

Waveguide dual-mode filters are widely used in payload systems of communication satellites, due to their reduced weight, compact size and electrical performance [3–6]. Their design has been conventionally accomplished by means of polynomials or lumped-element circuits [5, 7]. These classic techniques are very appropriate for the synthesis of narrowband filters [8], but they are not as accurate when dealing with broadband devices, since they do not take into account the frequency-dependence behavior of the real structures.

In order to achieve more realistic models, and with the aim of easing the design procedure of these filter implementations, more advanced equivalent circuits have been recently reported [9–13]. Even though they can provide better initial solutions, some iterative or optimization-based adjustments are typically needed for recovering the response specifications.

The design procedure here proposed employs a distributed model of the CWDM filter structure. The distributed models were introduced by Cohn [14], and since then they have been used for many applications [15–18]. Distributed models have shown very good reliability for dealing with broadband structures, since they can consider the frequency-dependence behavior of the waveguides [19–21], taking into account not only the periodic behavior of the transmission lines included in the model, but also the modal dispersion of the fundamental mode. Therefore, distributed models constitute a convenient half-way point between the fast but imprecise lumped models, and the more accurate but costly full-wave EM models.

2.2 Synthesis of the Lumped Model

The lumped model is a circuit which is equivalent (at the center frequency) to the real filter, and it is composed of ideal inverters, inductors and capacitors.

For the sake of clarity, the theoretical development will be carried out over a four-pole filter with two cavities, like the one depicted in Figure 2.1. Its routing diagram is shown in Figure 2.2. Each circle in the diagram represents one EM mode or resonance. EM modes 1 and 2 are the two degenerated resonant modes inside the first cavity, while modes 3 and 4 correspond to the resonant modes in the second cavity. Modes S and L represent the source and load modes, coming in and out from the filter, through the input/output waveguides. The lines connecting each pair of modes represent the coupling between the two modes. Each coupling is depicted with a solid line for direct couplings, and with a dashed line for cross couplings. This topology excites two degenerate resonances per cavity, and can produce two transmission zeros at real frequencies if the coupling between resonators 1 and 4 is negative, which is the case considered in the example. If this coupling is positive, two imaginary frequency zeros are created, which can be used to flatten the group delay response. These zeros are usually called equalization zeros for this reason.

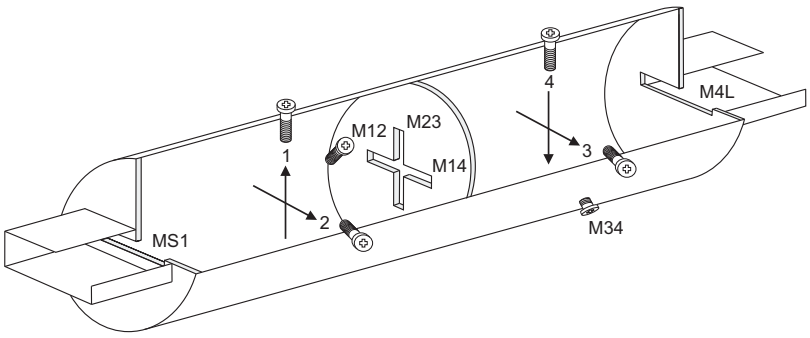

Figure 2.1 Physical structure of a circular-waveguide dual-mode filter with two cavities.

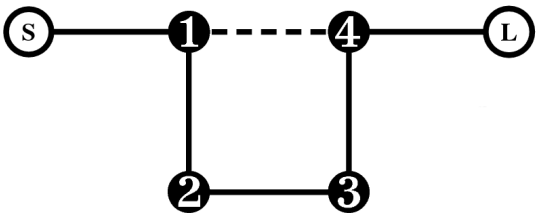

Figure 2.2 Routing diagram for the dual-mode filter shown in Figure 2.1.

Starting from the frequency specifications of the filter, the first step is to synthesize the coupling matrix (CM) in its "folded" form, following the procedure described in [22], and also outlined in appendix B.

Then, the folded matrix must be transformed into another matrix that can be implemented by the filter structure that is being designed. In other words, only the matrix elements which correspond with real couplings in the filter structure can be different from zero. For a four-pole dual-mode filter, the folded matrix already has the correct form, so no further transformations are needed. For other cases, the matrix transformation method will be explained in section 2.6.

The $N + 2$ CM of a four-pole dual-mode filter looks as follows:

$$M = \begin{pmatrix} 0 & M_{S1} & 0 & 0 & 0 & 0 \\ M_{S1} & 0 & M_{12} & 0 & M_{14} & 0 \\ 0 & M_{12} & 0 & M_{23} & 0 & 0 \\ 0 & 0 & M_{23} & 0 & M_{34} & 0 \\ 0 & M_{14} & 0 & M_{34} & 0 & M_{4L} \\ 0 & 0 & 0 & 0 & M_{4L} & 0 \end{pmatrix} \tag{2.1}$$

where M_{ij} represents the coupling between modes i and j (see Figure 2.2).

The values of the elements in the CM are employed to obtain the lumped model. The structure of this model is depicted in Figure 2.3. As it can be seen, it is composed

of ideal inverters and ideal LC resonators. It is easy to see the parallelism between this model and the physical structure. The top branch (S-1-4-L) represents the path of the vertical mode, while the bottom branch (2-3) corresponds to the horizontal mode. The LC resonators model filter cavities. There are two resonators per cavity to represent the two degenerated resonant modes inside each cavity. Inverters J_{S1} and J_{4L} model the input/output irises, inverters J_{12} and J_{34} represent the coupling between the two degenerated modes carried out by the oblique screws, and inverters J_{23} and J_{14} correspond to the cross-iris vertical and horizontal arms, respectively.

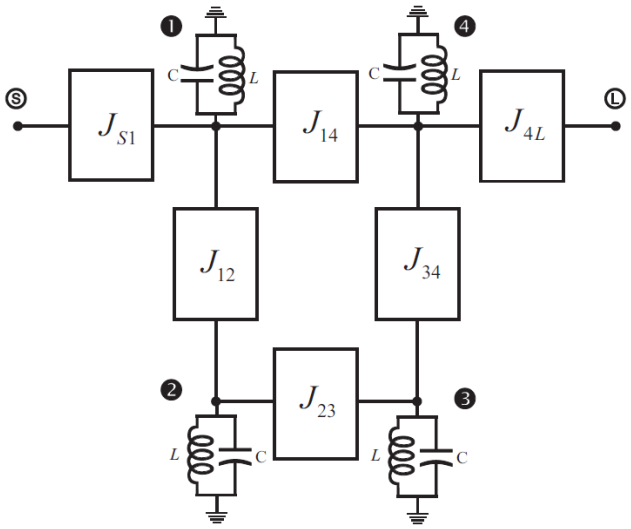

Figure 2.3 Lumped model of a four-pole dual-mode filter with two transmission zeros.

The values of the inverters are directly the values of the corresponding elements in the CM, while the values of the LC resonators can be calculated as follows:

$$L = \frac{\Delta\omega}{\omega_0^2} \tag{2.2}$$

$$C = \frac{1}{\Delta\omega} \tag{2.3}$$

where $\omega_0 = 2\pi f_0$ and $\Delta\omega = 2\pi BW$. The center frequency f_0 and the frequency bandwidth BW are given in the specifications.

2.3 Synthesis of the Distributed Model

The distributed model is composed of transmission lines and ideal inverters. A distributed model of a four-pole dual-mode filter with TE_{113} EM resonant mode (the electrical length of the cavity is $\phi = 3\pi$) has been depicted in Figure 2.4. As it can

be seen, the structure of the distributed-element model is practically the same as the structure of the lumped-element model, but the LC resonators have been substituted by transmission lines. Each transmission line representing one resonant mode inside each cavity has been cut in half in order to model the position of the oblique screw, which, for the TE_{113} mode, is placed in the middle of the cavity.

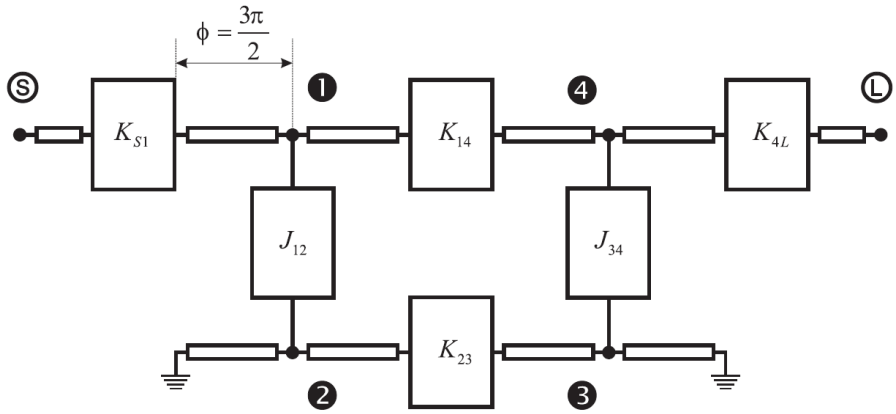

Figure 2.4 Distributed model of a four-pole dual-mode filter with the TE_{113} mode and two transmission zeros.

In the proposed distributed model, all internal lines have the same characteristic impedance. The input/output lines can also have the same characteristic impedance if K_{S1} and K_{4L} are suitably scaled. In fact, the whole circuit can be impedance scaled to have all lines with $Z_0 = 1\Omega$, if required.

The only elements to be designed in this model are the lengths of the transmission lines and the inverter values. The length of each transmission line (equivalent to half a cavity) will be obtained as

$$l = \frac{\phi}{\beta} \tag{2.4}$$

where β is the transmission line phase constant. The electrical length for half a cavity with TE_{113} mode is $\phi = 3\pi/2$.

The inverter values of the distributed model are not the same ones as those in the lumped model. Note also that some of the J-inverters have been substituted by K-inverters. The reason for using both admittance and impedance inverters in the same model is based on the following physical considerations. In the center of the cavity, the tangential electric field is high, so a small coupling value is better represented by an admittance inverter. At the end of the cavities, the tangential electric field is close to zero, and therefore a small coupling value is better represented by an impedance inverter [15].

The procedure to obtain the values for the inverters can be found in [1], and is going to be described below. It consists on simplifying the distributed model, making

use of valid approximations for narrowband applications, until a final lumped circuit is obtained. Identifying then the "collapsed" circuit elements with the ones of the lumped model obtained from the CM, one can easily derive the final expression for the inverters in the distributed model.

2.3.1 Modeling the Transmission Lines

For the sake of simplicity, all transmission lines in Figure 2.4 are assumed to have $Z_0 = 1\Omega$, although any arbitrary characteristic impedance can also be chosen. The first step in the procedure is to obtain a suitable model for a transmission line. The simplest way to proceed is to derive a model using the admittance matrix representation of a transmission line. For a transmission line of electrical length ϕ, the admittance matrix can be written as

$$\begin{aligned} Y &= j\frac{Y_0}{\sin\phi}\begin{pmatrix} -\cos\phi & 1 \\ 1 & -\cos\phi \end{pmatrix} \\ &= \begin{pmatrix} -jY_0\cot\phi & 0 \\ 0 & -jY_0\cot\phi \end{pmatrix} + \begin{pmatrix} 0 & j\dfrac{Y_0}{\sin\phi} \\ j\dfrac{Y_0}{\sin\phi} & 0 \end{pmatrix} \end{aligned} \tag{2.5}$$

The two matrices of the right-hand side of (2.5) are, respectively, parallel admittances ($Y_{11} = Y_{22} = -j\cot\phi$) and an admittance inverter with value $J = 1/\sin\phi$ (if $Y_0 = 1$). The equivalent circuit is displayed in Figure 2.5.

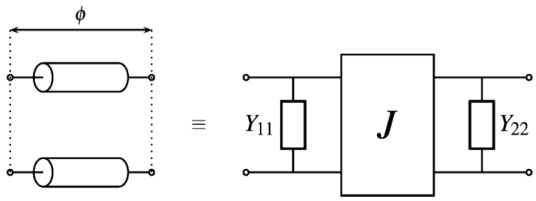

Figure 2.5 Equivalent model for a transmission line of electrical length ϕ.

Near the center frequency, $\phi \approx 3\pi/2$ and the term $\cot\phi$ can be approximated as follows ($\delta \ll 1$)

$$\cot\phi \approx \cot\frac{3\pi}{2}(1+\delta) = \frac{1-\tan\frac{3\pi}{2}\tan\frac{3\pi\delta}{2}}{\tan\frac{3\pi}{2}+\tan\frac{3\pi\delta}{2}} \approx -\tan\frac{3\pi\delta}{2} \approx -\frac{3\pi\delta}{2} \tag{2.6}$$

and therefore

$$Y_{11} = Y_{22} \approx jY_0\frac{3\pi\delta}{2} \tag{2.7}$$

These admittances can be physically approximated by a simple parallel resonator with L_p and C_p

$$\begin{aligned} Y_{11} = Y_{22} &= j\omega C_p + \frac{1}{j\omega L_p} = j\omega_0 C_p \left(\frac{\omega}{\omega_0} - \frac{\omega_0}{\omega} \right) \\ &= j\omega_0 C_p \frac{(\omega - \omega_0)(\omega + \omega_0)}{\omega\omega_0} \end{aligned} \tag{2.8}$$

where $\omega_0 = 1/\sqrt{L_p C_p}$. Near the resonance (or for narrow bandwidths), the next approximations can be introduced

$$\omega \approx \omega_0 \tag{2.9a}$$

$$\omega + \omega_0 \approx 2\omega_0 \tag{2.9b}$$

$$\frac{\omega - \omega_0}{\omega_0} = \delta \ll 1 \tag{2.9c}$$

Therefore, the parallel admittances of (2.8) can be written as

$$Y_{11} = Y_{22} = j2\omega_0 C_p \delta \tag{2.10}$$

and equating now (2.7) to (2.10), the following resonator elements values are directly obtained:

$$C_p = \frac{3\pi Y_0}{4\omega_0} \qquad L_p = \frac{4}{3\pi Y_0 \omega_0} \tag{2.11}$$

For the inverter value near the center frequency, we can write directly

$$J = \frac{Y_0}{\sin\phi} \approx \frac{Y_0}{\sin\frac{3\pi}{2}} = -Y_0 \tag{2.12}$$

After introducing the derived approximations, the final equivalent circuit of the transmission line near the center frequency becomes the one given in Figure 2.6.

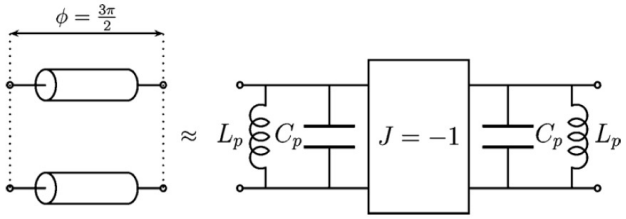

Figure 2.6 Approximate model for a transmission line of electrical length $\phi = 3\pi/2$ at f_0.

As a consequence, the distributed circuit shown in Figure 2.4 can be approximated by substituting the transmission lines (all of them with electrical length $\phi = 3\pi/2$) with the equivalent circuit shown in Figure 2.6.

The equivalent circuit of the short-circuited lines in Figure 2.4 can be obtained from the same model shown in Figure 2.6. Adding a short circuit to one port, the resonator at that port can be removed, and the inverter then transforms the short circuit in an open circuit at the other terminal of the inverter. As a result, the equivalent circuit of the shorted line is a resonator with L_p and C_p in parallel. Finally, grouping cascaded resonators, a lumped but rather complex model is obtained (see Figure 2.7). The procedure to simplify this model, in order to obtain a canonical circuit that can be directly compared to the one obtained from a CM, is explained in the following section.

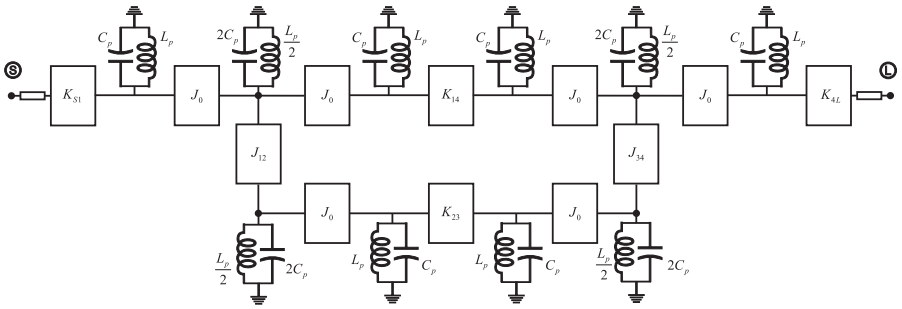

Figure 2.7 Lumped circuit after substituting all transmission lines by the equivalent circuit shown in Figure 2.6.

2.3.2 Simplification of the Model

Once the previous model has been derived, further simplifications have to be applied in order to obtain the desired lumped model (inverters connecting parallel resonators). The first practical consideration regards the low value of the K-inverters. These impedance inverters can be physically replaced by parallel susceptances $j\bar{B}$ and suitable transmission lines with length $\theta/2$ at their ends, thus obtaining

$$\bar{B} = \frac{1-\bar{K}^2}{\bar{K}} \tag{2.13a}$$

$$\theta = -\arctan\frac{2}{\bar{B}} \tag{2.13b}$$

Therefore, if $\bar{K} \ll 1$, then $|\bar{B}| \gg 1$ and $|\theta| \ll 1$ is almost a short circuit. The final conclusion is that any parallel resonator (near resonance) connected at the input/output of a K-inverter (with $\bar{K} \ll 1$) can be neglected. After neglecting the resonators placed at input/output of low K-inverters, combinations of two and three cascaded inverters appear (see Figure 2.8).

The combination of three cascaded inverters (whose combination is depicted in Figure 2.9) can be easily replaced by only one equivalent inverter which value is

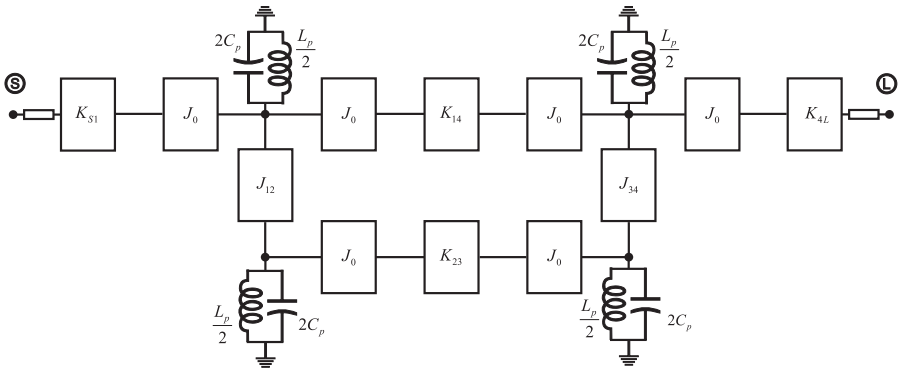

Figure 2.8 Lumped circuit after neglecting resonators adjacent to the K-inverters.

$$J_{eq} = KJ_0^2 \tag{2.14}$$

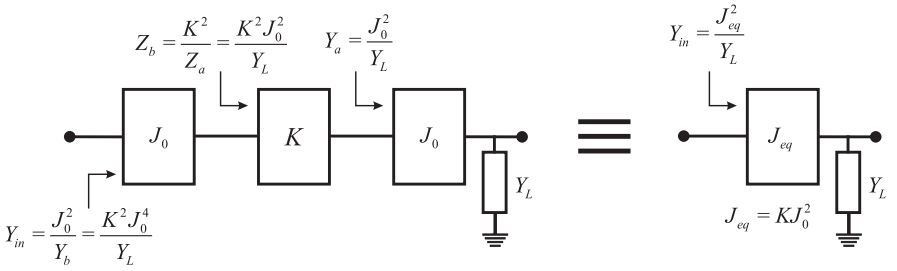

Figure 2.9 Three inverters (an impedance inverter between two admittance inverters) converted into one equivalent inverter.

The last transformation that needs to be done concerns the input/output impedance inverters cascaded with admittance inverters. In this case, they can be replaced by another two inverters in which one of them contains the equivalent inverter value, while the value of the other is equal to one (see Figure 2.10). The value of the equivalent admittance inverter can be calculated as

$$J_{eq} = \frac{KJ_0}{\sqrt{Z_{ref}}} \tag{2.15}$$

Properly scaling the inverter values allows the model to be used with different characteristic impedances for the input/output transmission lines if needed. Furthermore, resonators can be impedance scaled to match the required values of capacitors and inductors in the lumped canonical model.

After the previous replacements, a circuit like the one shown in Figure 2.11 is obtained. Note that this circuit has the same structure as the initial lumped model (see

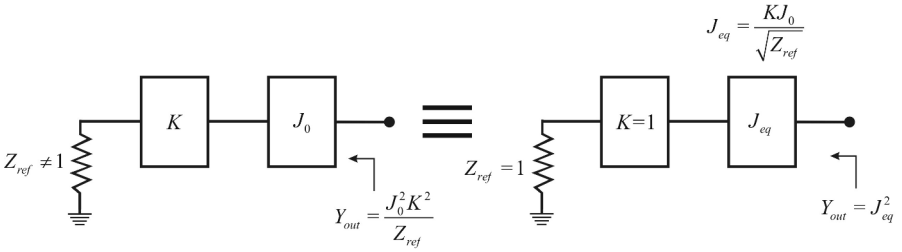

Figure 2.10 Two inverters are substituted by another two in which one of them contains the equivalent inverter value, while the value of the other is equal to one.

Figure 2.3), except for the two unity coupling inverters placed at the input/output ports. Indeed, when two unity inverters are added to both end sides of a certain circuit, its dual circuit is obtained, thus transforming impedances in admittances. However, the fact of adding the two inverters only affects to the phase of the S-parameters, but it does not change their modulus. Therefore, when designing individual filters (i.e. not being part of a multiplexer), the inverters with $K = 1$ connected to the input/output ports can be ignored.

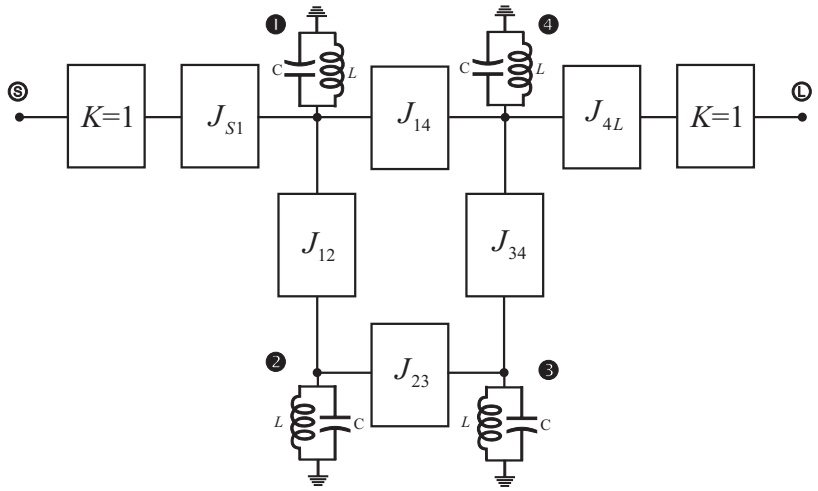

Figure 2.11 Lumped model obtained after the simplification of the equivalent circuit of the distributed model.

Once these unity inverters are removed, the resulting circuit has the same structure as the one shown in Figure 2.3, allowing the direct identification of the inverter values with those given by the CM elements. Following this approach, the normalized expressions are finally obtained, which for the TE_{113} mode are the following

$$\bar{K}_{S1} = M_{S1}\sqrt{\frac{3\pi}{2}\mathcal{W}_\lambda} \tag{2.16a}$$

$$\bar{K}_{4L} = M_{4L}\sqrt{\frac{3\pi}{2}\mathcal{W}_\lambda} \tag{2.16b}$$

$$\bar{J}_{12} = M_{12}\frac{3\pi}{2}\mathcal{W}_\lambda \tag{2.16c}$$

$$\bar{J}_{34} = M_{34}\frac{3\pi}{2}\mathcal{W}_\lambda \tag{2.16d}$$

$$\bar{K}_{14} = M_{14}\frac{3\pi}{2}\mathcal{W}_\lambda \tag{2.16e}$$

$$\bar{K}_{23} = M_{23}\frac{3\pi}{2}\mathcal{W}_\lambda \tag{2.16f}$$

Here, M_{ij} are the inverter values of the lumped model (which are the same as the corresponding elements of the CM) and $\mathcal{W}_\lambda$ is the guide-wavelength fractional bandwidth, and can be calculated as

$$\mathcal{W}_\lambda = \frac{\lambda_{g1} - \lambda_{g2}}{\lambda_{g0}} \tag{2.17}$$

Equations (2.16) can be generalized for TE_{11N} modes as

$$\bar{K}_{S1} = M_{S1}\sqrt{\frac{N\pi}{2}\mathcal{W}_\lambda} \tag{2.18a}$$

$$\bar{K}_{4L} = M_{4L}\sqrt{\frac{N\pi}{2}\mathcal{W}_\lambda} \tag{2.18b}$$

$$\bar{J}_{12} = M_{12}\frac{N\pi}{2}\mathcal{W}_\lambda \tag{2.18c}$$

$$\bar{J}_{34} = M_{34}\frac{N\pi}{2}\mathcal{W}_\lambda \tag{2.18d}$$

$$\bar{K}_{14} = M_{14}\frac{N\pi}{2}\mathcal{W}_\lambda \tag{2.18e}$$

$$\bar{K}_{23} = M_{23}\frac{N\pi}{2}\mathcal{W}_\lambda \tag{2.18f}$$

2.4 Determination of the Physical Dimensions

The final stage in the design process is to find the dimensions of the physical filter, so it can be manufactured. It will be carried out with the support of the previously synthesized distributed model and a full-wave EM simulator. The EM simulator should take into account all the effects of the real waveguide structure shown in Figure 2.1, and at the same time, it must be efficient enough to perform the required simulations in a reasonable time. The full-wave EM solver FEST3D [23] has been chosen in this case. The details of the design procedure are given below.

2.4.1 Iris Dimensions

The first step is to find the dimensions of all the irises in the filter structure. In this case, a T-network has been chosen as the equivalent circuit of an iris with a certain thickness (see Figure 2.12). For the general case, which considers an iris with a different waveguide in each side (like in the input/output irises), the T-network equivalent circuit is the one shown in Figure 2.13 [24].

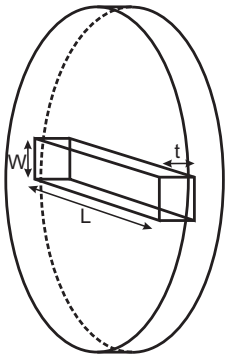

Figure 2.12 Geometry of a rectangular thick iris.

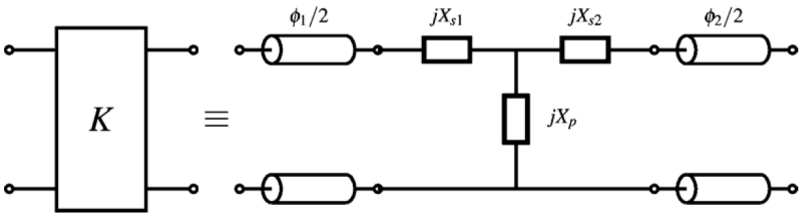

Figure 2.13 Equivalent circuit of a K-inverter with a T-network for modeling a thick asymmetric iris.

The values of all the elements of the equivalent circuit in Figure 2.13 can be obtained from the S-parameters of the iris (obtained with an EM solver) as:

$$jX_{s1} = \frac{(1+S_{11})(1-S_{22})+S_{21}^2-2S_{21}}{(1-S_{11})(1-S_{22})-S_{21}^2} \tag{2.19a}$$

$$jX_{s2} = \frac{(1-S_{11})(1+S_{22})+S_{21}^2-2S_{21}}{(1-S_{11})(1-S_{22})-S_{21}^2} \tag{2.19b}$$

$$jX_p = \frac{2S_{21}}{(1-S_{11})(1-S_{22})-S_{21}^2} \tag{2.19c}$$

$$\phi_1 = -\arctan\left(\frac{\Sigma}{\Pi_-}\right)-\arctan\left(\frac{\Delta}{\Pi_+}\right) \tag{2.19d}$$

$$\phi_2 = -\arctan\left(\frac{\Sigma}{\Pi_-}\right)+\arctan\left(\frac{\Delta}{\Pi_+}\right) \tag{2.19e}$$

where

$$\Sigma = X_{s1}+X_{s2}+2X_p \tag{2.20a}$$

$$\Delta = X_{s1}-X_{s2} \tag{2.20b}$$

$$\Pi_+ = 1+X_{s1}X_{s2}+X_p(X_{s1}+X_{s2}) \tag{2.20c}$$

$$\Pi_- = 1-X_{s1}X_{s2}-X_p(X_{s1}+X_{s2}) \tag{2.20d}$$

which reduces to the well-known equations given in [25] and [22] when symmetrical irises are considered.

The inverter value K produced by the iris can be obtained as

$$K = \sqrt{\left|\frac{1+\Gamma e^{-j\phi_1}}{1-\Gamma e^{-j\phi_1}}\right|} \tag{2.21a}$$

$$\Gamma = \frac{j\Delta-\Pi_+}{j\Sigma-\Pi_-} \tag{2.21b}$$

Using the previous equations, and with the distributed model in hand, the iris dimensions are derived through the following iterative process:

1. Choose the initial dimensions for the iris. They could be, for example, a certain fraction of the width of the adjacent waveguides.
2. Employing an EM solver, perform a simulation of a circuit formed by the iris and the adjacent waveguides with their lengths equal to zero. The simulation is made over a single frequency point, which is the center frequency of the filter, and the S-parameters of the iris are obtained.
3. Calculate the equivalent K of the iris using (2.19) and (2.21).
4. Change the iris dimensions (up or down depending on the comparison of the current and the desired value of K) and go back to step 2. It is possible to vary

only one iris dimension, usually the length L (see Figure 2.12), or more than one dimension at the same time. Repeat the process until the K value of the iris reaches the corresponding K value in the distributed model.

As it can be seen in Figure 2.13, the equivalent circuit of a K-inverter is composed of a T-network and two adjacent transmission lines. However, the equivalent circuit of an iris is just a T-network without the transmission lines, which means that when the designed irises are introduced in the filter structure, the two transmission lines calculated with (2.19d) and (2.19e) must be added at both sides of the iris. Since for this particular case the electrical lengths obtained are always negative, this leads to a length reduction of the adjacent waveguides (i.e. the circular cavities and the input/output waveguides).

All the irises in the filter structure are designed separately, repeating the iterative algorithm explained above as many times as the number of present irises. Note that the cruciform iris can be interpreted as two orthogonal irises, so they can be designed as two independent irises. In practice, in order to increase the accuracy, these irises are first designed as independent irises, and then each of them is re-designed considering the presence of the other one, thus taking into account the small variation introduced in the coupling value.

When the inverter value K is negative, as it is the case of the M_{14} coupling of a 4-pole dual-mode filter with real transmission zeros, the iris is designed as if it were positive, and then the oblique screws of the adjacent cavities will be placed in such a position that there is a difference of 90 degrees between them (see Figure 2.1). Proceeding in that way, the vertical modes inside the two cavities are forced to have opposite sign, thus obtaining the so called virtual negative coupling [22].

2.4.2 Dimensions of Cavities and Screws

The initial length of the cavities is calculated using equation (2.4), and subtracting the corresponding phase values obtained according to (2.19) in both sides of the cavity.

At this point, a problem with the dual cavity length arises. The dual cavity is modeled by two lines in the equivalent distributed model. These lines are equal in electrical length, but once the real irises are introduced, they produce different ϕ values according to (2.19). Therefore, there are several ϕ's to be embedded (one at each end of the cavity for the vertical polarization, and only one for the horizontal polarization) in the cavity length. As a result, the same physical cavity has to show different electrical length for each orthogonal mode. This problem is solved by means of the vertical and horizontal tuning screws (see Figure 2.1). Changing the penetration of the vertical/horizontal screws, the resonant frequency of the corresponding vertical/horizontal mode is shifted. In fact, after increasing the penetration depth of the tuning screw, the corresponding resonant frequency is decreased.

The adjustment of the screws and the cavities is done stage by stage (i.e. one cavity at a time), employing the distributed model. It is carried out by comparing the

responses of the circuits of figures 2.14 and 2.15, which correspond to one stage of the distributed model and one stage of the EM model, respectively.

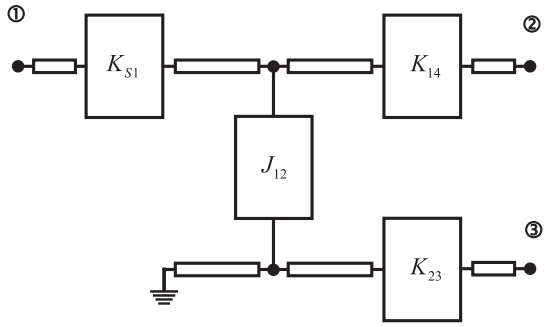

Figure 2.14 One stage (representing one cavity) of the distributed model.

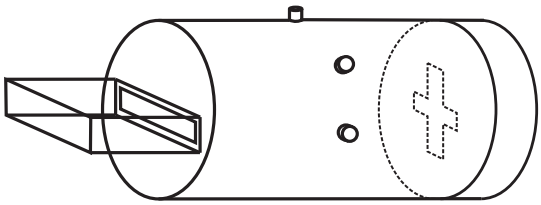

Figure 2.15 One stage (i.e. one cavity) of the EM model.

Figure 2.16 shows a typical response of the circuits of Figures 2.14 and 2.15. Parameter S_{21} represents the path between the input/output iris (vertical mode) and the horizontal arm of the cruciform iris (vertical mode), while S_{31} refers to the path between the input/output iris (vertical mode) and the vertical arm of the cruciform iris (horizontal mode).

The goal here is to match the EM response of each cavity with the response of the corresponding stage of the distributed model. A full-wave EM simulator (FEST3D) is going to be used in order to obtain the response of the structure shown in Figure 2.15. The procedure to design each filter cavity is described below.

1. **Insertion of the vertical tuning screw.** The penetration of the vertical tuning screw is fixed and it will not be modified along the process. The chosen length must be long enough to allow tuning after the fabrication, but not too long either to prevent unwanted high power effects (for example, a penetration of 1.5 or 2 mm would be a good choice for a Ku-band filter). At this point, the lengths of the horizontal and oblique screws are set to zero.

2. **Frequency tuning of the vertical mode.** The group delay of S_{21} (see Figure 2.14) presents a very sharp peak centered at the resonant frequency of the

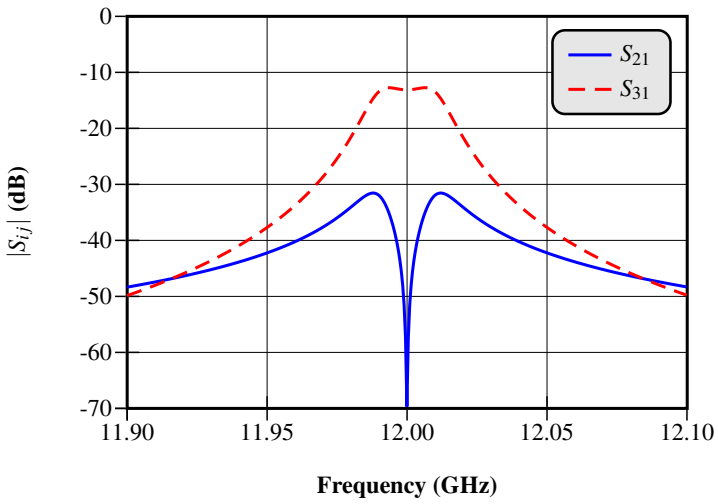

Figure 2.16 Response of one stage of the distributed model (see Figure 2.14).

vertical mode. The cavity length is adjusted so the resonance peak of this parameter is centered at the center frequency of the filter.

3. **Frequency tuning of the horizontal mode.** As it happened with the vertical mode, the group delay of S_{33} presents a very sharp peak centered at the resonant frequency of the horizontal mode. The penetration of the horizontal tuning screw is modified until that peak is centered at the center frequency of the filter.

4. **Insertion of the coupling screw.** The initial penetration of the oblique screw is chosen as the mean value between the penetrations of the other two screws in the cavity. Once this is done, the response of the circuit will already be very similar to the one shown in Figure 2.16.

5. **Balancing the two lobes of S_{21}.** The penetration of the horizontal screw is modified until the two lobes of S_{21} have the same width. While balancing the two lobes of S_{21}, the two lobes of S_{31} are being leveled at the same time.

6. **Adjusting the separation between the two lobes of S_{21}.** The separation between the two lobes is controlled by means of the oblique screw. Therefore, its penetration will be adjusted until the separation between the two lobes in the EM model is the same as in the distributed model. After this step, the balance between the two lobes may have been slightly altered. If this is the case, they can be balanced again by modifying the horizontal screw.

7. **Adjustment of the cavity length.** The cavity length is adjusted until the minimum of S_{21} (the valley between the two peaks) is centered at the center frequency of the filter.

After the process, the response of the EM model will perfectly match the response of the distributed model. The same procedure needs to be repeated for all the cavities composing the filter. Once the individual cavities have been designed, they are assembled together to form the filter, which will have the desired response requested in the filter specifications. A design example of a four-pole CWDM filter with two transmission zeros has been included in section 2.7.1.

2.5 Design of Dual-Mode Filters of Other Orders

The procedure for obtaining the distributed model described in sections 2.2 and 2.3 has been explained over a four-pole filter example. However, even though it is true that the design process is essentially the same for other filter orders, there are some issues like the size and organization of the CM, or the distributed model structure, that will change depending on the case. Therefore, this section is devoted to describe the physical structures, models and matrices of all the filter orders and topologies considered in this work. The four-pole case will be omitted since it has been widely explained in the previous sections.

2.5.1 Five-Pole Filters

The five-pole dual-mode filter is a special case since it has an odd order, and therefore one of the cavities is single-mode. As in the case of the four-pole filter, it can accommodate 2 transmission zeros. The reason why this case has been considered is because it can be useful in practice, and it is indeed employed by the industry. This filters are in fact more selective in frequency than four-pole filters, but its tuning is considerably easier than with six-pole filters.

The five-pole filter structure has three cavities, of which the first two have two orthogonal resonant modes, while the third one only has one resonant mode. Figure 2.17 shows the physical implementation of a five-pole filter. As it can be seen, cavities 2 and 3 are connected through an horizontal iris instead of a cruciform iris, so only the vertical mode will be able to pass from cavity 2 to cavity 3.

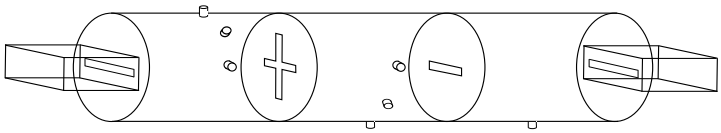

Figure 2.17 Physical structure of a five-pole dual-mode filter.

The corresponding distributed model must be accommodated to the physical implementation of the filter, so it will have the structure shown in Figure 2.18.

The inverter values are obtained in the same way as for a four-pole dual-mode filter, and the specific formulas are (considering TE_{11N} resonant modes)

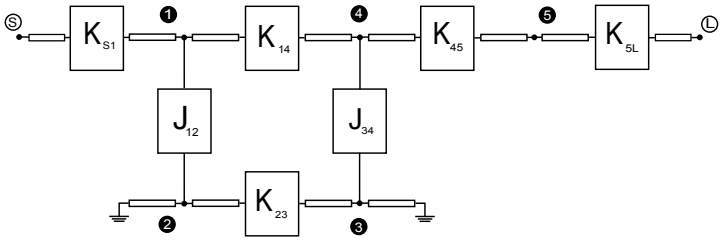

Figure 2.18 Distributed model of a five-pole dual-mode filter.

$$\bar{K}_{S1} = \bar{K}_{5L} = M_{S1}\sqrt{\frac{N\pi}{2}\mathcal{W}} \tag{2.22a}$$

$$\bar{J}_{12} = M_{12}\frac{N\pi}{2}\mathcal{W} \tag{2.22b}$$

$$\bar{K}_{14} = M_{14}\frac{N\pi}{2}\mathcal{W} \tag{2.22c}$$

$$\bar{K}_{23} = M_{23}\frac{N\pi}{2}\mathcal{W} \tag{2.22d}$$

$$\bar{J}_{34} = M_{34}\frac{N\pi}{2}\mathcal{W} \tag{2.22e}$$

$$\bar{K}_{45} = M_{45}\frac{N\pi}{2}\mathcal{W} \tag{2.22f}$$

where M_{ij} are the values of the five-pole filter CM (2.23), which, as happened with the four-pole filter, is the same as the folded CM.

$$M = \begin{pmatrix} 0 & M_{S1} & 0 & 0 & 0 & 0 & 0 \\ M_{S1} & 0 & M_{12} & 0 & M_{14} & 0 & 0 \\ 0 & M_{12} & 0 & M_{23} & 0 & 0 & 0 \\ 0 & 0 & M_{23} & 0 & M_{34} & 0 & 0 \\ 0 & M_{14} & 0 & M_{34} & 0 & M_{45} & 0 \\ 0 & 0 & 0 & 0 & M_{45} & 0 & M_{S1} \\ 0 & 0 & 0 & 0 & 0 & M_{S1} & 0 \end{pmatrix} \tag{2.23}$$

The extraction of the dimensions of the first two cavities of the filter (see Figure 2.17) is exactly the same as for the four-pole filter case explained in the previous sections. The design of the single-mode cavity is simply done by fixing the penetration of its only screw and adjusting the cavity length to adjust the resonant frequency of the vertical (and only) mode.

2.5.2 Six-Pole Filters

A six-pole dual-mode filter is composed of 3 cavities, with two orthogonal modes inside each cavity. As in the previous cases, its frequency response is able to accommodate 2 transmission zeros. Its physical structure is depicted in Figure 2.19.

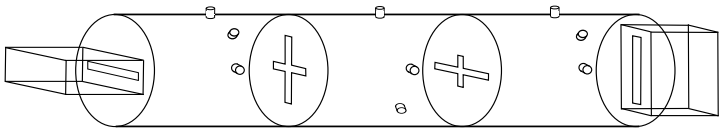

Figure 2.19 Physical structure of a six-pole dual-mode filter.

The distributed model corresponding to the previous physical structure is shown in Figure 2.20, and its inverter values are calculated according to (2.24).

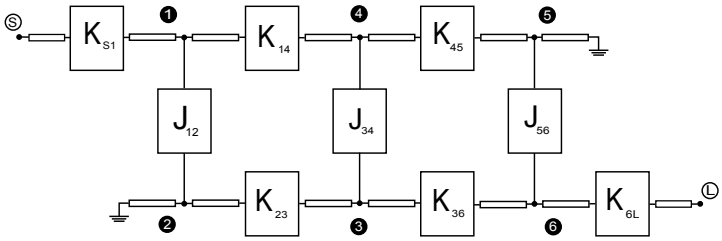

Figure 2.20 Distributed model of a six-pole dual-mode filter.

$$\bar{K}_{S1} = \bar{K}_{6L} = M_{S1}\sqrt{\frac{N\pi}{2}\mathcal{W}} \tag{2.24a}$$

$$\bar{J}_{12} = \bar{J}_{56} = M_{12}\frac{N\pi}{2}\mathcal{W} \tag{2.24b}$$

$$\bar{K}_{23} = \bar{K}_{45} = M_{23}\frac{N\pi}{2}\mathcal{W} \tag{2.24c}$$

$$\bar{J}_{34} = M_{34}\frac{N\pi}{2}\mathcal{W} \tag{2.24d}$$

$$\bar{K}_{14} = \bar{K}_{36} = M_{14}\frac{N\pi}{2}\mathcal{W} \tag{2.24e}$$

In this case, unlike it happened for the four and five-pole filters, the CM whose elements are employed to calculate the inverter values is not the same as the folded CM, but it needs to be suitably reconfigured. This will also occur for the rest of the filter orders considered below. The transformation procedure will be explained in section 2.6. After the reconfiguration, the CM will have this structure:

$$M = \begin{pmatrix} 0 & M_{S1} & 0 & 0 & 0 & 0 & 0 & 0 \\ M_{S1} & 0 & M_{12} & 0 & M_{14} & 0 & 0 & 0 \\ 0 & M_{12} & 0 & M_{23} & 0 & 0 & 0 & 0 \\ 0 & 0 & M_{23} & 0 & M_{34} & 0 & M_{14} & 0 \\ 0 & M_{14} & 0 & M_{34} & 0 & M_{23} & 0 & 0 \\ 0 & 0 & 0 & 0 & M_{23} & 0 & M_{12} & 0 \\ 0 & 0 & 0 & M_{14} & 0 & M_{12} & 0 & M_{S1} \\ 0 & 0 & 0 & 0 & 0 & 0 & M_{S1} & 0 \end{pmatrix} \tag{2.25}$$

Here, the process to extract the physical dimensions of the lateral cavities is the same as for four-pole filters. The central cavity, however, is slightly different to the previously considered cavities, since it has cross-irises in both sides of the cavity (see Figure 2.19). Consequently, the corresponding stage of the distributed model has four accesses instead of three. Nevertheless, the port of the distributed model corresponding with the vertical arm of one of the cross-irises (it does not matter which one) is ignored (i.e. the distributed model is simulated with the four ports, but one of them is not used). Hence, the tuning process to obtain the dimensions of the screws and the length of this cavity is performed with the remaining three ports, following the same procedure as for the lateral cavities. The same strategy has also been applied for the rest of the filters with central cavities with two cross-irises considered along this section.

2.5.3 Eight-Pole Filters with Symmetric Structure

An eight-pole dual-mode filter is composed of 4 cavities and can incorporate 4 transmission zeros. Two different realizations have been considered: eight-pole filters with symmetric structure and eight-pole filters with asymmetric structure. It is important not to confuse the symmetry in the structure with the symmetry in the response. Indeed, the two cases here considered provide a symmetric response.

For the symmetric case, all the cavities are interconnected through cruciform irises, as it can be seen in Figure 2.21.

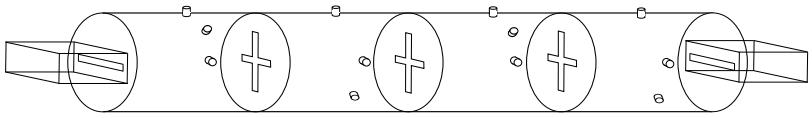

Figure 2.21 Physical structure of an eight-pole dual-mode filter with symmetric structure.

The corresponding distributed model is depicted in Figure 2.22. The formulas to calculate the inverter values are detailed below, where the symmetry can be appreciated, since $J_{12} = J_{78}$, $K_{23} = K_{67}$, etc.

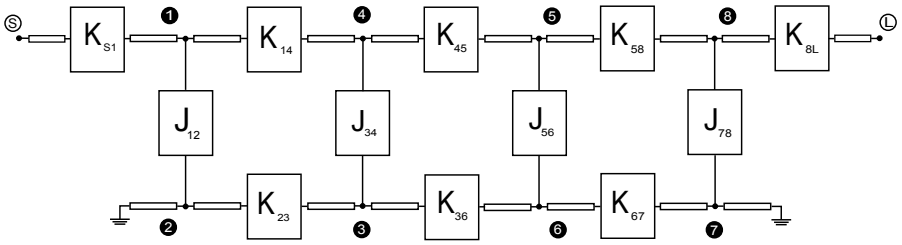

Figure 2.22 Distributed model of an eight-pole dual-mode filter with symmetric structure.

$$\bar{K}_{S1} = \bar{K}_{8L} = M_{S1}\sqrt{\frac{N\pi}{2}\mathcal{W}} \tag{2.26a}$$

$$\bar{J}_{12} = \bar{J}_{78} = M_{12}\frac{N\pi}{2}\mathcal{W} \tag{2.26b}$$

$$\bar{K}_{23} = \bar{K}_{67} = M_{23}\frac{N\pi}{2}\mathcal{W} \tag{2.26c}$$

$$\bar{J}_{34} = \bar{J}_{56} = M_{34}\frac{N\pi}{2}\mathcal{W} \tag{2.26d}$$

$$\bar{K}_{36} = M_{36}\frac{N\pi}{2}\mathcal{W} \tag{2.26e}$$

$$\bar{K}_{14} = \bar{K}_{58} = M_{14}\frac{N\pi}{2}\mathcal{W} \tag{2.26f}$$

$$\bar{K}_{45} = M_{45}\frac{N\pi}{2}\mathcal{W} \tag{2.26g}$$

The structure of the CM is detailed next:

$$M = \begin{pmatrix} 0 & M_{S1} & 0 & 0 & 0 & 0 & 0 & 0 & 0 & 0 \\ M_{S1} & 0 & M_{12} & 0 & M_{14} & 0 & 0 & 0 & 0 & 0 \\ 0 & M_{12} & 0 & M_{23} & 0 & 0 & 0 & 0 & 0 & 0 \\ 0 & 0 & M_{23} & 0 & M_{34} & 0 & M_{36} & 0 & 0 & 0 \\ 0 & M_{14} & 0 & M_{34} & 0 & M_{45} & 0 & 0 & 0 & 0 \\ 0 & 0 & 0 & 0 & M_{45} & 0 & M_{34} & 0 & M_{14} & 0 \\ 0 & 0 & 0 & M_{36} & 0 & M_{34} & 0 & M_{23} & 0 & 0 \\ 0 & 0 & 0 & 0 & 0 & 0 & M_{23} & 0 & M_{12} & 0 \\ 0 & 0 & 0 & 0 & 0 & M_{14} & 0 & M_{12} & 0 & M_{S1} \\ 0 & 0 & 0 & 0 & 0 & 0 & 0 & 0 & M_{S1} & 0 \end{pmatrix} \tag{2.27}$$

2.5.4 Eight-Pole Filters with Asymmetric Structure

As it happens with the symmetric case, asymmetric eight-pole dual-mode filters have 4 cavities. However, in this case one of the cruciform irises, more specifically the one between cavities 2 and 3, has been replaced by an horizontal iris (see Figure 2.23). That means that cavities 2 and 3 are solely coupled by the vertical mode, since the horizontal iris blocks the horizontal mode.

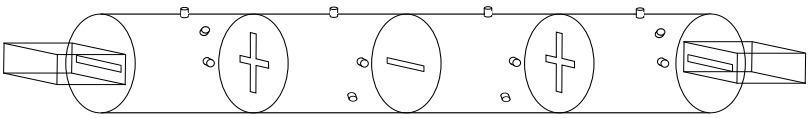

Figure 2.23 Physical structure of an eight-pole dual-mode filter with asymmetric structure.

The distributed model of the previous structure is shown in Figure 2.24, where it can be seen that it is composed of two cascaded quartets (each quartet constitutes a four-pole filter) connected through the K_{45} inverter.

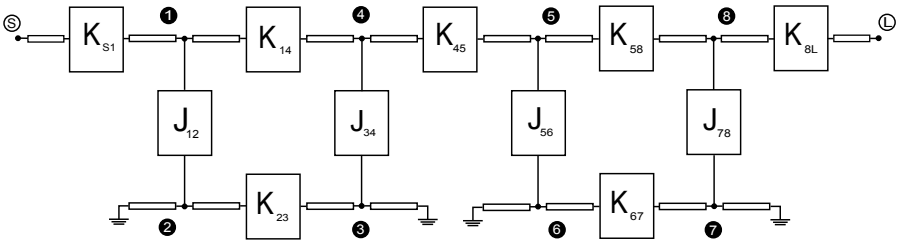

Figure 2.24 Distributed model of an eight-pole dual-mode filter with asymmetric structure.

The inverter values of the distributed model will be obtained as indicated in (2.28).

$$\bar{K}_{S1} = \bar{K}_{8L} = M_{S1}\sqrt{\frac{N\pi}{2}\mathcal{W}} \tag{2.28a}$$

$$\bar{J}_{12} = M_{12}\frac{N\pi}{2}\mathcal{W} \tag{2.28b}$$

$$\bar{K}_{23} = M_{23}\frac{N\pi}{2}\mathcal{W} \tag{2.28c}$$

$$\bar{J}_{34} = M_{34}\frac{N\pi}{2}\mathcal{W} \tag{2.28d}$$

$$\bar{K}_{14} = M_{14}\frac{N\pi}{2}\mathcal{W} \tag{2.28e}$$

$$\bar{K}_{45} = M_{45}\frac{N\pi}{2}\mathcal{W} \tag{2.28f}$$

$$\bar{J}_{56} = M_{56}\frac{N\pi}{2}\mathcal{W} \tag{2.28g}$$

$$\bar{K}_{67} = M_{67}\frac{N\pi}{2}\mathcal{W} \tag{2.28h}$$

$$\bar{J}_{78} = M_{78}\frac{N\pi}{2}\mathcal{W} \tag{2.28i}$$

$$\bar{K}_{58} = M_{58}\frac{N\pi}{2}\mathcal{W} \tag{2.28j}$$

where it can be appreciated that in this case there is no symmetry. The CM structure will be very similar to the symmetric case, but now the M_{36} element is equal to zero, due to the lack of horizontal-mode coupling between cavities 2 and 3. Note that the values of the rest of the elements will be completely different than those obtained for the symmetric case.

$$M = \begin{pmatrix} 0 & M_{S1} & 0 & 0 & 0 & 0 & 0 & 0 & 0 & 0 \\ M_{S1} & 0 & M_{12} & 0 & M_{14} & 0 & 0 & 0 & 0 & 0 \\ 0 & M_{12} & 0 & M_{23} & 0 & 0 & 0 & 0 & 0 & 0 \\ 0 & 0 & M_{23} & 0 & M_{34} & 0 & 0 & 0 & 0 & 0 \\ 0 & M_{14} & 0 & M_{34} & 0 & M_{45} & 0 & 0 & 0 & 0 \\ 0 & 0 & 0 & 0 & M_{45} & 0 & M_{56} & 0 & M_{58} & 0 \\ 0 & 0 & 0 & 0 & 0 & M_{56} & 0 & M_{67} & 0 & 0 \\ 0 & 0 & 0 & 0 & 0 & 0 & M_{67} & 0 & M_{78} & 0 \\ 0 & 0 & 0 & 0 & 0 & M_{58} & 0 & M_{78} & 0 & M_{S1} \\ 0 & 0 & 0 & 0 & 0 & 0 & 0 & 0 & M_{S1} & 0 \end{pmatrix} \tag{2.29}$$

2.5.5 Ten-Pole Filters

A ten-pole dual-mode filter is formed by 5 cavities and, as in the eight-pole case, can accommodate 4 transmission zeros. Its structure is shown in Figure 2.25.

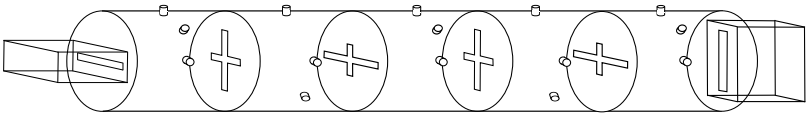

Figure 2.25 Physical structure of a ten-pole dual-mode filter.

The distributed model is depicted in Figure 2.26, while its inverter values can be calculated following (2.30).

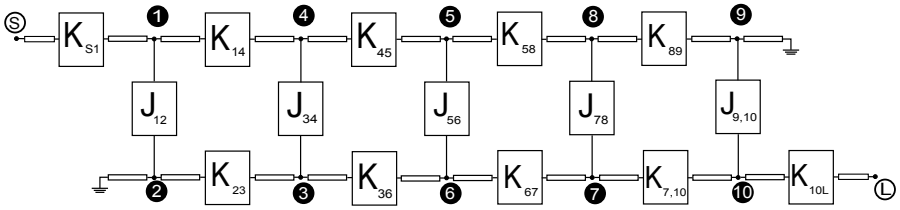

Figure 2.26 Distributed model of a ten-pole dual-mode filter.

$$\bar{K}_{S1} = \bar{K}_{10L} = M_{S1}\sqrt{\frac{N\pi}{2}\mathcal{W}} \tag{2.30a}$$

$$\bar{J}_{12} = \bar{J}_{9,10} = M_{12}\frac{N\pi}{2}\mathcal{W} \tag{2.30b}$$

$$\bar{K}_{23} = \bar{K}_{89} = M_{23}\frac{N\pi}{2}\mathcal{W} \tag{2.30c}$$

$$\bar{J}_{34} = \bar{J}_{78} = M_{34}\frac{N\pi}{2}\mathcal{W} \tag{2.30d}$$

$$\bar{K}_{14} = \bar{K}_{7,10} = M_{14}\frac{N\pi}{2}\mathcal{W} \tag{2.30e}$$

$$\bar{K}_{45} = \bar{K}_{67} = M_{45}\frac{N\pi}{2}\mathcal{W} \tag{2.30f}$$

$$\bar{K}_{36} = \bar{K}_{58} = M_{36}\frac{N\pi}{2}\mathcal{W} \tag{2.30g}$$

$$\bar{J}_{56} = M_{56}\frac{N\pi}{2}\mathcal{W} \tag{2.30h}$$

The matrix obtained from the folded CM after the appropriate transformations will have the structure shown in (2.31).

$$M = \begin{pmatrix}
0 & M_{S1} & 0 & 0 & 0 & 0 & 0 & 0 & 0 & 0 & 0 & 0 \\
M_{S1} & 0 & M_{12} & 0 & M_{14} & 0 & 0 & 0 & 0 & 0 & 0 & 0 \\
0 & M_{12} & 0 & M_{23} & 0 & 0 & 0 & 0 & 0 & 0 & 0 & 0 \\
0 & 0 & M_{23} & 0 & M_{34} & 0 & M_{36} & 0 & 0 & 0 & 0 & 0 \\
0 & M_{14} & 0 & M_{34} & 0 & M_{45} & 0 & 0 & 0 & 0 & 0 & 0 \\
0 & 0 & 0 & 0 & M_{45} & 0 & M_{56} & 0 & M_{36} & 0 & 0 & 0 \\
0 & 0 & 0 & M_{36} & 0 & M_{56} & 0 & M_{45} & 0 & 0 & 0 & 0 \\
0 & 0 & 0 & 0 & 0 & 0 & M_{45} & 0 & M_{34} & 0 & M_{14} & 0 \\
0 & 0 & 0 & 0 & 0 & M_{36} & 0 & M_{34} & 0 & M_{23} & 0 & 0 \\
0 & 0 & 0 & 0 & 0 & 0 & 0 & 0 & M_{23} & 0 & M_{12} & 0 \\
0 & 0 & 0 & 0 & 0 & 0 & 0 & M_{14} & 0 & M_{12} & 0 & M_{S1} \\
0 & 0 & 0 & 0 & 0 & 0 & 0 & 0 & 0 & 0 & M_{S1} & 0
\end{pmatrix} \tag{2.31}$$

2.5.6 Twelve-Pole Filters with Symmetric Structure

A twelve-pole dual-mode filter is composed of 6 cavities and can incorporate 6 transmission zeros. The concept of symmetric and asymmetric structure is the same one used for eight-pole dual-mode filters. The structure of the symmetric case has been depicted in Figure 2.27.

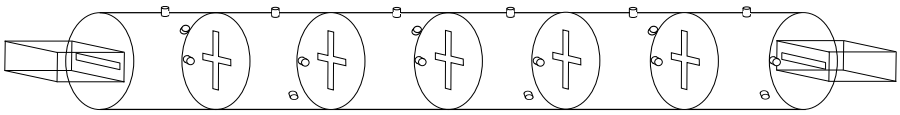

Figure 2.27 Physical structure of an twelve-pole dual-mode filter with symmetric structure.

The corresponding distributed model is depicted in Figure 2.28, and the formulas to calculate the inverter values are detailed below.

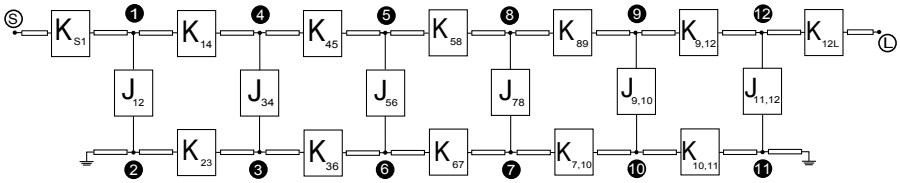

Figure 2.28 Distributed model of an twelve-pole dual-mode filter with symmetric structure.

$$\bar{K}_{S1} = \bar{K}_{12L} = M_{S1}\sqrt{\frac{N\pi}{2}\mathcal{W}} \tag{2.32a}$$

$$\bar{J}_{12} = \bar{J}_{11,12} = M_{12}\frac{N\pi}{2}\mathcal{W} \tag{2.32b}$$

$$\bar{K}_{23} = \bar{K}_{10,11} = M_{23}\frac{N\pi}{2}\mathcal{W} \tag{2.32c}$$

$$\bar{J}_{34} = \bar{J}_{9,10} = M_{34}\frac{N\pi}{2}\mathcal{W} \tag{2.32d}$$

$$\bar{K}_{14} = \bar{K}_{9,12} = M_{14}\frac{N\pi}{2}\mathcal{W} \tag{2.32e}$$

$$\bar{K}_{45} = \bar{K}_{89} = M_{45}\frac{N\pi}{2}\mathcal{W} \tag{2.32f}$$

$$\bar{K}_{36} = \bar{K}_{7,10} = M_{36}\frac{N\pi}{2}\mathcal{W} \tag{2.32g}$$

$$\bar{J}_{56} = \bar{J}_{78} = M_{56}\frac{N\pi}{2}\mathcal{W} \tag{2.32h}$$

$$\bar{K}_{67} = M_{67}\frac{N\pi}{2}\mathcal{W} \tag{2.32i}$$

$$\bar{K}_{58} = M_{58}\frac{N\pi}{2}\mathcal{W} \tag{2.32j}$$

The structure of the CM of a twelve-pole dual-mode filter is

$$M = \begin{pmatrix}
0 & M_{S1} & 0 & 0 & 0 & 0 & 0 & 0 & 0 & 0 & 0 & 0 & 0 & 0 \\
M_{S1} & 0 & M_{12} & 0 & M_{14} & 0 & 0 & 0 & 0 & 0 & 0 & 0 & 0 & 0 \\
0 & M_{12} & 0 & M_{23} & 0 & 0 & 0 & 0 & 0 & 0 & 0 & 0 & 0 & 0 \\
0 & 0 & M_{23} & 0 & M_{34} & 0 & M_{36} & 0 & 0 & 0 & 0 & 0 & 0 & 0 \\
0 & M_{14} & 0 & M_{34} & 0 & M_{45} & 0 & 0 & 0 & 0 & 0 & 0 & 0 & 0 \\
0 & 0 & 0 & 0 & M_{45} & 0 & M_{56} & 0 & M_{58} & 0 & 0 & 0 & 0 & 0 \\
0 & 0 & 0 & M_{36} & 0 & M_{56} & 0 & M_{67} & 0 & 0 & 0 & 0 & 0 & 0 \\
0 & 0 & 0 & 0 & 0 & 0 & M_{67} & 0 & M_{56} & 0 & M_{36} & 0 & 0 & 0 \\
0 & 0 & 0 & 0 & 0 & M_{58} & 0 & M_{56} & 0 & M_{45} & 0 & 0 & 0 & 0 \\
0 & 0 & 0 & 0 & 0 & 0 & 0 & 0 & M_{45} & 0 & M_{34} & 0 & M_{14} & 0 \\
0 & 0 & 0 & 0 & 0 & 0 & 0 & M_{36} & 0 & M_{34} & 0 & M_{23} & 0 & 0 \\
0 & 0 & 0 & 0 & 0 & 0 & 0 & 0 & 0 & 0 & M_{23} & 0 & M_{12} & 0 \\
0 & 0 & 0 & 0 & 0 & 0 & 0 & 0 & 0 & M_{14} & 0 & M_{12} & 0 & M_{S1} \\
0 & 0 & 0 & 0 & 0 & 0 & 0 & 0 & 0 & 0 & 0 & 0 & M_{S1} & 0
\end{pmatrix} \tag{2.33}$$

2.5.7 Twelve-Pole Filters with Asymmetric Structure

The physical structure of an asymmetric twelve-pole dual-mode filter is depicted in Figure 2.29. Note that, again, some of the cruciform irises have been replaced with horizontal irises.

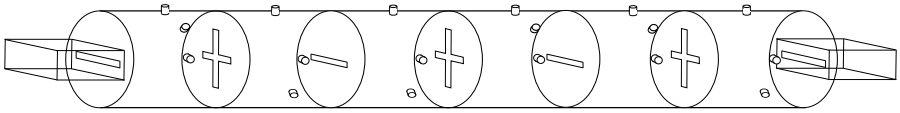

Figure 2.29 Physical structure of an twelve-pole dual-mode filter with asymmetric structure.

The corresponding distributed model can be seen in Figure 2.28, while the inverter values ca be calculated using (2.34).

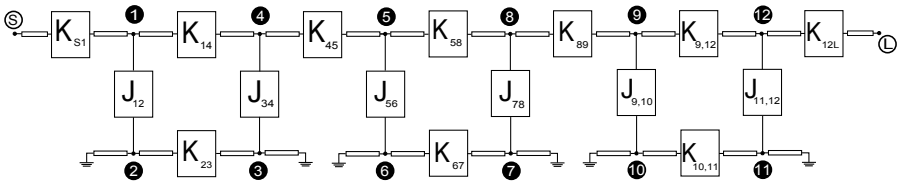

Figure 2.30 Distributed model of an twelve-pole dual-mode filter with asymmetric structure.

$$\bar{K}_{S1} = \bar{K}_{12L} = M_{S1}\sqrt{\frac{N\pi}{2}\mathcal{W}} \tag{2.34a}$$

$$\bar{J}_{12} = M_{12}\frac{N\pi}{2}\mathcal{W} \tag{2.34b}$$

$$\bar{K}_{23} = M_{23}\frac{N\pi}{2}\mathcal{W} \tag{2.34c}$$

$$\bar{J}_{34} = M_{34}\frac{N\pi}{2}\mathcal{W} \tag{2.34d}$$

$$\bar{K}_{14} = M_{14}\frac{N\pi}{2}\mathcal{W} \tag{2.34e}$$

$$\bar{K}_{45} = M_{45}\frac{N\pi}{2}\mathcal{W} \tag{2.34f}$$

$$\bar{J}_{56} = M_{56}\frac{N\pi}{2}\mathcal{W} \tag{2.34g}$$

$$\bar{K}_{67} = M_{67}\frac{N\pi}{2}\mathcal{W} \tag{2.34h}$$

$$\bar{J}_{78} = M_{78}\frac{N\pi}{2}\mathcal{W} \tag{2.34i}$$

$$\bar{K}_{58} = M_{58}\frac{N\pi}{2}\mathcal{W} \tag{2.34j}$$

$$\bar{K}_{89} = M_{89}\frac{N\pi}{2}\mathcal{W} \tag{2.34k}$$

$$\bar{J}_{9,10} = M_{9,10}\frac{N\pi}{2}\mathcal{W} \tag{2.34l}$$

$$\bar{K}_{10,11} = M_{10,11}\frac{N\pi}{2}\mathcal{W} \tag{2.34m}$$

$$\bar{J}_{11,12} = M_{11,12}\frac{N\pi}{2}\mathcal{W} \tag{2.34n}$$

$$\bar{K}_{9,12} = M_{9,12}\frac{N\pi}{2}\mathcal{W} \tag{2.34o}$$

The transformed CM will have the following structure:

$$M = \begin{pmatrix}
0 & M_{S1} & 0 & 0 & 0 & 0 & 0 & 0 & 0 & 0 & 0 & 0 & 0 & 0 \\
M_{S1} & 0 & M_{12} & 0 & M_{14} & 0 & 0 & 0 & 0 & 0 & 0 & 0 & 0 & 0 \\
0 & M_{12} & 0 & M_{23} & 0 & 0 & 0 & 0 & 0 & 0 & 0 & 0 & 0 & 0 \\
0 & 0 & M_{23} & 0 & M_{34} & 0 & 0 & 0 & 0 & 0 & 0 & 0 & 0 & 0 \\
0 & M_{14} & 0 & M_{34} & 0 & M_{45} & 0 & 0 & 0 & 0 & 0 & 0 & 0 & 0 \\
0 & 0 & 0 & 0 & M_{45} & 0 & M_{56} & 0 & M_{58} & 0 & 0 & 0 & 0 & 0 \\
0 & 0 & 0 & 0 & 0 & M_{56} & 0 & M_{67} & 0 & 0 & 0 & 0 & 0 & 0 \\
0 & 0 & 0 & 0 & 0 & 0 & M_{67} & 0 & M_{78} & 0 & 0 & 0 & 0 & 0 \\
0 & 0 & 0 & 0 & 0 & M_{58} & 0 & M_{78} & 0 & M_{89} & 0 & 0 & 0 & 0 \\
0 & 0 & 0 & 0 & 0 & 0 & 0 & 0 & M_{89} & 0 & M_{910} & 0 & M_{912} & 0 \\
0 & 0 & 0 & 0 & 0 & 0 & 0 & 0 & 0 & M_{910} & 0 & M_{1011} & 0 & 0 \\
0 & 0 & 0 & 0 & 0 & 0 & 0 & 0 & 0 & 0 & M_{1011} & 0 & M_{1112} & 0 \\
0 & 0 & 0 & 0 & 0 & 0 & 0 & 0 & 0 & M_{912} & 0 & M_{1112} & 0 & M_{S1} \\
0 & 0 & 0 & 0 & 0 & 0 & 0 & 0 & 0 & 0 & 0 & 0 & M_{S1} & 0
\end{pmatrix} \tag{2.35}$$

2.6 Reconfiguration of the Folded Coupling Matrix

In this section, the method to transform the folded CM in another matrix adapted to any particular dual-mode filter structure is going to be explained. All the filter orders and topologies considered in the previous section are going to be addressed. The theoretical concepts employed in this section have been extracted from [22].

As it was explained in sections 2.2 and 2.5, for four- and five-pole dual-mode filters no transformation is needed, since the folded CM has already a suitable structure (i.e. all the matrix elements representing non-physical couplings are equal to zero). Coupling matrices of higher filter orders, on the other hand, need to be reconfigured.

For all the cases, except for the asymmetric twelve-pole filter, the starting point will be the folded CM with order $N \times N$, where N is the filter order. The source and load couplings will not be considered at first, and they will be added at the end of the transformation process.

2.6.1 Folded Form of the Coupling Matrix

The folded CM of a filter can be obtained from the filter specifications, following the process described in [22], and also outlined in appendix B.

For filters with symmetric response, like the ones considered in this work, an $N + 2$ folded CM (which includes the source and load couplings) has the structure shown in (2.36). For the sake of explanation, an example of an eight-order filter has been represented. In this matrix, s and l are the source and load couplings,

respectively. The couplings identified by m are direct couplings, and x represents the cross couplings. The routing diagram of this matrix can be seen in Figure 2.31.

$$M = \begin{pmatrix} 0 & s & 0 & 0 & 0 & 0 & 0 & 0 & 0 & 0 \\ s & 0 & m & 0 & 0 & 0 & 0 & 0 & 0 & 0 \\ 0 & m & 0 & m & 0 & 0 & 0 & x & 0 & 0 \\ 0 & 0 & m & 0 & m & 0 & x & 0 & 0 & 0 \\ 0 & 0 & 0 & m & 0 & m & 0 & 0 & 0 & 0 \\ 0 & 0 & 0 & 0 & m & 0 & m & 0 & 0 & 0 \\ 0 & 0 & 0 & x & 0 & m & 0 & m & 0 & 0 \\ 0 & 0 & x & 0 & 0 & 0 & m & 0 & m & 0 \\ 0 & 0 & 0 & 0 & 0 & 0 & 0 & m & 0 & l \\ 0 & 0 & 0 & 0 & 0 & 0 & 0 & 0 & l & 0 \end{pmatrix} \tag{2.36}$$

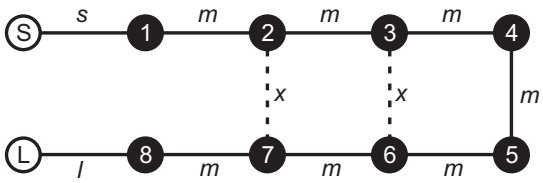

Figure 2.31 Routing diagram corresponding with an eight-order folded CM, including the source and load nodes.

2.6.2 Rotations of the Coupling Matrix

The CM reconfiguration is carried out by means of matrix rotations, also called similarity transformations. A rotation on an $N \times N$ coupling matrix M_0 is carried out by pre- and post-multiplying M_0 by an $N \times N$ rotation matrix R and its transpose R^t, thus obtaining the rotated matrix M_1 as follows

$$M_1 = R \cdot M_0 \cdot R^t \tag{2.37}$$

The rotation matrix R is given by a pivot [i,j] ($i \neq j$) and a rotation angle θ. For example, a six-order rotation matrix with pivot [3,5] would be

$$R = \begin{pmatrix} 1 & 0 & 0 & 0 & 0 & 0 \\ 0 & 1 & 0 & 0 & 0 & 0 \\ 0 & 0 & c & 0 & -s & 0 \\ 0 & 0 & 0 & 1 & 0 & 0 \\ 0 & 0 & s & 0 & c & 0 \\ 0 & 0 & 0 & 0 & 0 & 1 \end{pmatrix} \tag{2.38}$$

where $c \equiv \cos\theta$ and $s \equiv \sin\theta$. The pivot [i,j] indicates that $R_{ii} = R_{jj} = \cos\theta$ and $R_{ji} = -R_{ij} = \sin\theta$, ($i, j \neq 1$ or N). The other principal diagonal entries are equal to one, and all other off-diagonal entries are zero.

After the rotation, the eigenvalues of the matrix M_1 are the same as those of the original matrix M_0. Therefore, the CM obtained after a rotation (or a series of rotations) leads to a filter response equal to the one obtained with the original matrix.

2.6.3 The Even-Mode Coupling Matrices

An even-mode coupling matrix M_e is formed by reflecting the quadrants of the $N \times N$ folded coupling matrix M about the horizontal and vertical lines of symmetry, superimposed into the upper left quadrant. Equation (2.39) shows the extraction of the even-mode matrix from a six-degree CM.

$$M = \left[\begin{array}{ccc|ccc} 0 & M_{12} & 0 & 0 & 0 & 0 \\ M_{12} & 0 & M_{23} & 0 & M_{25} & 0 \\ 0 & M_{23} & 0 & M_{34} & 0 & 0 \\ \hline 0 & 0 & M_{34} & 0 & M_{23} & 0 \\ 0 & M_{25} & 0 & M_{23} & 0 & M_{12} \\ 0 & 0 & 0 & 0 & M_{12} & 0 \end{array}\right] \tag{2.39a}$$

$$M_e = \begin{bmatrix} 0 & M_{12} & 0 \\ M_{12} & M_{25} & M_{23} \\ 0 & M_{23} & M_{34} \end{bmatrix} = \begin{bmatrix} 0 & K_{12} & 0 \\ K_{12} & K_{22} & K_{23} \\ 0 & K_{23} & K_{33} \end{bmatrix} \tag{2.39b}$$

2.6.4 CM Reconfiguration for Six-Pole Filters

First of all, the even-mode matrix must be obtained from the 6 × 6 folded CM as explained in (2.39). After that, a rotation is made over the even-mode CM, with pivot [2,3] and angle θ_1 given by

$$\theta_1 = \tan^{-1} \frac{M_{23} - \sqrt{M_{23}^2 - M_{25}M_{34}}}{M_{34}} \tag{2.40}$$

After the rotation, a new matrix M'_e is obtained, which needs to be unfolded, as described in (2.41). As a result, the new coupling matrix M' will be finally obtained, which will be suitable for being implemented by a six-pole dual-mode filter.

$$M'_e = \begin{bmatrix} 0 & K'_{12} & K'_{13} \\ K'_{12} & 0 & K'_{23} \\ K'_{13} & K'_{23} & K'_{33} \end{bmatrix} \tag{2.41a}$$

$$M' = \left[\begin{array}{ccc|ccc} 0 & K'_{12} & 0 & K'_{13} & 0 & 0 \\ K'_{12} & 0 & K'_{23} & 0 & 0 & 0 \\ 0 & K'_{23} & 0 & K'_{33} & 0 & K'_{13} \\ \hline K'_{13} & 0 & K'_{33} & 0 & K'_{23} & 0 \\ 0 & 0 & 0 & K'_{23} & 0 & K'_{12} \\ 0 & 0 & K'_{13} & 0 & K'_{12} & 0 \end{array}\right] \tag{2.41b}$$

2.6.5 CM Reconfiguration for Symmetric Eight-Pole Filters

As for the six-pole filter, the process starts with the extraction of the even-mode matrix, following the same procedure. Then, two consecutive rotations are applied over the even-mode matrix, with pivots [3,4] and [2,4], respectively, and angles θ_1 and θ_2 given by

$$\theta_1 = \tan^{-1}\left[\frac{M_{27}M_{34} \pm \sqrt{M_{27}^2M_{34}^2 + M_{27}M_{45}(M_{23}^2 - M_{27}M_{36})}}{M_{23}^2 - M_{27}M_{36}}\right] \tag{2.42a}$$

$$\theta_2 = \tan^{-1}\left[\frac{M_{27}}{M_{23}\sin\theta_1}\right] \tag{2.42b}$$

After unfolding tho rotated matrix, the reconfigured CM for a symmetric eight-pole dual-mode filter is obtained.

2.6.6 CM Reconfiguration for Asymmetric Eight-Pole Filters

In order to transform the CM of an eight-pole dual-mode filter with cascaded quartets, even-mode matrices are not going to be employed. In this case, rotations are directly applied over the full CM. A total of four rotations are needed, with pivots [3,5], [4,6], [5,7] and [2,4], respectively. The first rotation angle will be obtained by solving the following second-degree equation:

$$\begin{aligned} t_1^2(M_{27}M_{34}M_{45} - M_{23}M_{56}M_{67} + M_{27}M_{36}M_{56}) \\ +t_1[M_{23}M_{36}M_{67} - M_{27}(M_{34}^2 - M_{45}^2 - M_{56}^2 + M_{36}^2)] \\ -M_{27}(M_{36}M_{56} + M_{34}M_{45}) = 0 \end{aligned}$$

where $t_1 = \tan\theta_1$. The rest of the rotation angles will be given by

$$\theta_2 = \tan^{-1}\left[\frac{-M_{36}}{M_{34}}\right] \tag{2.43a}$$

$$\theta_3 = \tan^{-1}\left[\frac{-M_{47}}{M_{45}}\right] \tag{2.43b}$$

$$\theta_4 = \tan^{-1}\left[\frac{M_{25}}{M_{45}}\right] \tag{2.43c}$$

2.6.7 CM Reconfiguration for Ten-Pole Filters

In the reconfiguration of the CM of a ten-pole dual-mode filter, the rotations are going to be carried out over its even-mode matrix. Three rotations are necessary in total, with pivots [4,5], [3,5] and [2,4], whose angles can be calculated as

$$\theta_1 = \tan^{-1}\left[\frac{M_{45} \pm \sqrt{M_{45}^2 - M_{47}M_{56}}}{M_{56}}\right] \tag{2.44a}$$

$$\theta_2 = \tan^{-1}\left[\frac{s_1 M_{34} \pm \sqrt{s_1^2 M_{34}^2 - M_{38}(M_{47} + M_{56})}}{M_{47} + M_{56}}\right] \tag{2.44b}$$

$$\theta_3 = \tan^{-1}\left[\frac{t_2 M_{23}}{M_{45} - t_1 M_{56} + c_1 t_2 M_{34}}\right] \tag{2.44c}$$

where $c_1 = \cos\theta_1$, $s_1 = \sin\theta_1$, $t_1 = \tan\theta_1$ and $t_2 = \tan\theta_2$. Once the three rotations have been applied, the resulting matrix must be unfolded.

2.6.8 CM Reconfiguration for Symmetric Twelve-Pole Filters

Just as for the rest of the symmetric cases, rotations are made over the even-mode matrix. In this case, five rotations will be needed, whose pivots are [4,5], [5,6], [4,6], [3,5] and [2,4]. In order to obtain the first rotation angle, the following quadratic equation must be solved:

$$t_1^4 + d_3 t_1^3 + d_2 t_1^2 + d_1 t_1 + d_0 = 0 \tag{2.45}$$

where $t_1 = \tan\theta_1$ and

$$
\begin{aligned}
d &= a_2c_3^2 + a_3c_2^2 \\
d_0 &= \frac{a_0 + a_3c_0^2 + a_4c_0}{d} \\
d_1 &= \frac{a_1 + 2a_0c_3 + 2a_3c_0c_1 + a_4(c_1 + c_0c_3)}{d} \\
d_2 &= \frac{a_2 + 2a_1c_3 + a_0c_3^2 + a_3(c_1^2 + 2c_0c_2) + a_4(c_2 + c_1c_3)}{d} \\
d_3 &= \frac{2a_2c_3 + a_1c_3^2 + 2a_3c_1c_2 + a_4c_2c_3}{d}
\end{aligned}
$$

The coefficients in the previous equations can be calculated as

$$
\begin{aligned}
a_0 &= M_{58} & b_0 &= M_{49}M_{67} & c &= a_3b_5 - a_4b_4 \\
a_1 &= 2M_{45} & b_1 &= -2M_{45}M_{67} & c_0 &= \frac{a_0b_4 - a_3b_0}{c} \\
a_2 &= M_{49} - \frac{M_{34}^2}{M_{3,10}} & b_2 &= M_{58}M_{67} - M_{56}^2 & c_1 &= \frac{a_1b_4 - a_3b_1}{c} \\
a_3 &= M_{67} & b_3 &= -2M_{56}M_{45} & c_2 &= \frac{a_2b_4 - a_3b_2}{c} \\
a_4 &= -2M_{56} & b_4 &= M_{49}M_{58} - M_{45}^2 & c_3 &= \frac{a_3b_3}{c} \\
& & b_5 &= 2M_{56}M_{49}
\end{aligned}
$$

The rest of the rotation angles can be obtained as

$$
\begin{aligned}
\theta_2 &= \tan^{-1}\left[\frac{c_0 + c_1t_1 + c_2t_1^2}{(1 + c_3t_1)\sqrt{1 + t_2^2}}\right] \\
\theta_3 &= \tan^{-1}\left(\frac{K_{46}}{K_{66}}\right) \\
\theta_4 &= \tan^{-1}\left(\frac{K_{35}}{K_{55}}\right) \\
\theta_5 &= \tan^{-1}\left(\frac{K_{25}}{K_{45}}\right)
\end{aligned}
$$

where K_{ij} are the elements in the matrix obtained in the preceding rotation.

2.6.9 CM Reconfiguration for Asymmetric Twelve-Pole Filters

The CM transformation of an asymmetric twelve-pole dual-mode filter is different from the rest of the cases. In this special case, the first step is to transform the folded

CM into another canonical matrix, called arrow matrix. In an arrow matrix, the only non-zero elements are placed in the main diagonal, in the upper and lower secondary diagonals, in the last row and in the last column. An example of a 7×7 arrow matrix is shown below, where the reason for its name can be appreciated.

$$M = \begin{pmatrix} 0 & x & 0 & 0 & 0 & 0 & x \\ x & x & x & 0 & 0 & 0 & x \\ 0 & x & x & x & 0 & 0 & x \\ 0 & 0 & x & x & x & 0 & x \\ 0 & 0 & 0 & x & x & x & x \\ 0 & 0 & 0 & 0 & x & x & x \\ x & x & x & x & x & x & 0 \end{pmatrix}$$

As it was expressed at the beginning of section 2.6, this is the only case in which the source and load couplings are considered within the reconfiguration process. Therefore, the arrow matrix will be calculated from the folded CM and the corresponding source and load couplings and, as a result, an $N + 2$ arrow matrix (where $N = 12$ is the filter order) will be obtained. The synthesis process to obtain the arrow CM can be found in section 10.3.2 of [22].

With the arrow matrix in hand, a series of rotations will be applied, which are going to be described next. The routing diagram of the arrow matrix of a twelve-pole filter has been depicted in Figure 2.32 (a), where it can be seen that the load node is connected with all nodes from 6 to 12. First of all, a trisection (connection between three nodes) must be created, by creating a coupling between nodes 10 and 12. This is done by applying a rotation with pivot [12,13] and angle θ_1 given by

$$\theta_1 = \tan^{-1} \frac{M_{12,13}}{TZ_1 + M_{13,13}} \tag{2.48}$$

where TZ_1 is one of the transmission zeros of the filter, which must be normalized with respect to the center frequency and the filter bandwidth. This transmission zero can be real, which means that it is visible in the modulus of the frequency response, or can also be imaginary, also known as equalization zero. The routing diagram obtained after creating the first trisection can be seen in Figure 2.32 (b).

The next step is to move this trisection along the main diagonal towards the source. This is done by carrying out a series of rotations, and with each rotation the trisection will move forward one position. At the end of the process, the coupling in question will be placed between nodes 1 and 3, and the cross coupling between nodes 6 and L will have disappeared (see Figure 2.32 (c)). In order to carry out this translation, a total of 9 rotations must be applied, whose rotation angles are given by the following expression:

$$\theta_r = \tan^{-1} \frac{M_{kl}}{M_{mn}} \tag{2.49}$$

Rotation r	Pivot $[i, j]$	k	l	m	n
2	[11,12]	11	13	12	13
3	[10,11]	10	12	11	12
4	[9,10]	9	11	10	11
5	[8,9]	8	10	9	10
6	[7,8]	7	9	8	9
7	[6,7]	6	8	7	8
8	[5,6]	5	7	6	7
9	[4,5]	4	6	5	6
10	[3,4]	3	5	4	5

Table 2.1 Rotations applied to move the first trisection.

The subscripts values in (2.49) and the corresponding rotation pivots are detailed in Table 2.1.

Then, another trisection must be created, again between nodes 10 and 12 (see Figure 2.32 (d)), by a rotation with pivot [12,13] and angle

$$\theta_{11} = \tan^{-1} \frac{M_{12,13}}{TZ_2 + M_{13,13}} \tag{2.50}$$

where TZ_2 is the transmission zero which is symmetric to the previous one[1].

After creating the second trisection, it must be moved toward the main diagonal, as it was done before, so the coupling is finally placed between nodes 3 and 5. Again, as it is shown in Figure 2.32 (e), another cross coupling is gone, now the one between nodes 7 and L. In this case, 7 rotations are required, whose angles are given by (2.49). The subscripts and pivots are detailed in Table 2.2.

After that, the previous two trisections must be joint to form a quartet, thus obtaining the routing diagram shown in Figure 2.32 (f). Two rotations must be applied, with pivots [4,5] and [3,4], respectively, and with angles

$$\theta_{19} = \tan^{-1} \left[\frac{M_{46}}{M_{56}} \right] \tag{2.51a}$$

$$\theta_{20} = \tan^{-1} \left[\frac{M_{35}}{M_{45}} \right] \tag{2.51b}$$

Then, the whole process must be repeated in order to create a second quartet. First, a trisection is created between nodes 10 and 12, by applying a rotation with pivot [12,13], and angle

[1]Only symmetric responses are permitted with this technique.

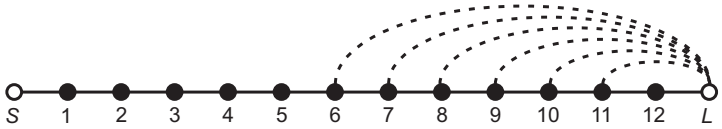

(a) Routing diagram of the arrow form.

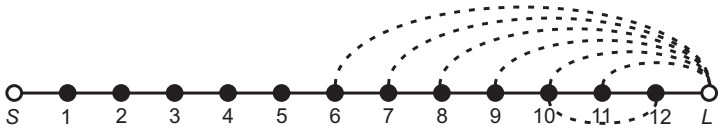

(b) Creation of the first trisection between nodes 10 and 12.

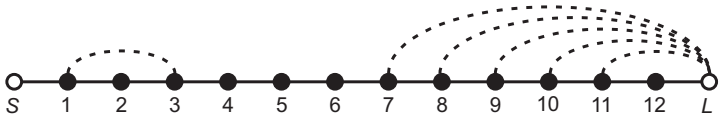

(c) Translation of the first trisection.

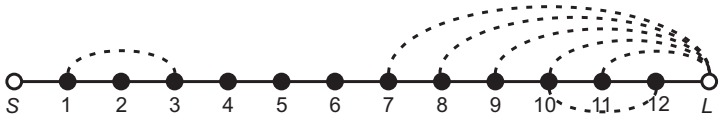

(d) Creation of the second trisection between nodes 10 and 12.

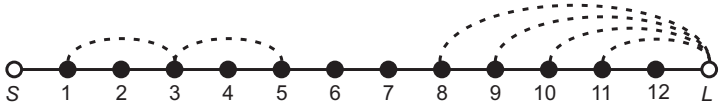

(e) Translation of the second trisection.

(f) Creation of the first quartet (nodes 1, 2, 3 and 4).

Figure 2.32 Routing diagrams showing the transformation process to create the first quartet in the asymmetric twelve-pole filter example.

Rotation r	Pivot $[i,j]$	k	l	m	n
12	[11,12]	11	13	12	13
13	[10,11]	10	12	11	12
14	[9,10]	9	11	10	11
15	[8,9]	8	10	9	10
16	[7,8]	7	9	8	9
17	[6,7]	6	8	7	8
18	[5,6]	5	7	6	7

Table 2.2 Rotations applied to move the second trisection.

Rotation r	Pivot $[i,j]$	k	l	m	n
22	[11,12]	11	13	12	13
23	[10,11]	10	12	11	12
24	[9,10]	9	11	10	11
25	[8,9]	8	10	9	10
26	[7,8]	7	9	8	9

Table 2.3 Rotations applied to move the third trisection.

$$\theta_{21} = \tan^{-1} \frac{M_{12,13}}{TZ_3 + M_{13,13}} \tag{2.52}$$

where TZ_3 is another transmission zero (there is a total of three pairs of transmission zeros).

The previous trisection is moved up, until it is situated between nodes 5 and 7, and thus eliminating the coupling between nodes 8 and L. To do that, five rotations are applied, whose angles are given by (2.49), whereas subscripts and pivots can be found in Table 2.3.

The next step is to create a fourth trisection with pivot [12,13] and angle

$$\theta_{27} = \tan^{-1} \frac{M_{12,13}}{TZ_4 + M_{13,13}} \tag{2.53}$$

where TZ_4 is the transmission zero which is symmetric to TZ_3. This trisection is then moved until the coupling is situated between nodes 7 and 9, by means of three rotations with angles θ_r given by (2.49), and the subscripts and pivots appearing in Table 2.4. In this case, the translation eliminates the cross coupling between nodes 9 and L.

Trisections three and four are joint together to form a second quartet, by applying two consecutive rotations with pivots [8,9] and [7,8] and angles

Rotation r	Pivot $[i, j]$	k	l	m	n
28	[11,12]	11	13	12	13
29	[10,11]	10	12	11	12
30	[9,10]	9	11	10	11

Table 2.4 Rotations applied to move the fourth trisection.

$$\theta_{31} = \tan^{-1}\left[\frac{M_{8,10}}{M_{9,10}}\right] \tag{2.54a}$$

$$\theta_{32} = \tan^{-1}\left[\frac{M_{79}}{M_{89}}\right] \tag{2.54b}$$

Finally, a third quartet needs to be built. To do that, a fifth trisection is created by a rotation with pivot [12,13] and angle

$$\theta_{33} = \tan^{-1}\frac{M_{12,13}}{TZ_5 + M_{13,13}} \tag{2.55}$$

where TZ_5 will be another transmission zero. In this case, a single rotation is applied in order to move up one position, with rotation pivot [11,12] and whose angle is

$$\theta_{34} = \tan^{-1}\frac{M_{11,13}}{M_{12,13}} \tag{2.56}$$

The previous translation eliminates the existing coupling between nodes 10 and L. The sixth required trisection is already there, since it coincides with the cross coupling between nodes 11 and L, which was already present in the arrow form. It just needs to be joint with the previous one, thus forming the third quartet, by applying the last two rotations with pivots [12,13] and [11,12], and angles

$$\theta_{35} = \tan^{-1}\left[\frac{M_{12,14}}{M_{13,14}}\right] \tag{2.57a}$$

$$\theta_{36} = \tan^{-1}\left[\frac{M_{11,13}}{M_{12,13}}\right] \tag{2.57b}$$

Once the previous process has been completed, the CM obtained is ready to be implemented by an asymmetric twelve-pole dual-mode filter with 3 cascaded quartets.

2.7 Design Examples

In this section, two design examples are going to be presented: a four-pole filter and a symmetric eight-pole filter. The corresponding numerical details and results will be shown next.

2.7.1 Four-Pole Filter

The filter specifications are the following ones:

- Order: $N = 4$
- Center frequency: $f_0 = 12$ GHz
- Bandwidth: $BW = 27$ MHz
- Return loss: $RL = 20$ dB
- Stopband rejection: > 40 dB
- Resonant mode inside the cavities: TE_{113}

In order to obtain the required rejection in the stopband, the two transmission zeros must be centered at frequencies 11.928 GHz and 12.032 GHz, respectively, which are symmetric with respect to the center frequency of the filter.

Starting from the filter specifications, the $N + 2$ folded CM is obtained, which does not need to be transformed:

$$M = \begin{pmatrix} 0 & 1.0270 & 0 & 0 & 0 & 0 \\ 1.0270 & 0 & 0.8851 & 0 & -0.1158 & 0 \\ 0 & 0.8851 & 0 & 0.7460 & 0 & 0 \\ 0 & 0 & 0.7460 & 0 & 0.8851 & 0 \\ 0 & -0.1158 & 0 & 0.8851 & 0 & 1.0270 \\ 0 & 0 & 0 & 0 & 1.0270 & 0 \end{pmatrix}$$

The inverter values in the lumped model (see Figure 2.3) are directly the corresponding elements in the CM, therefore

$$\begin{aligned} J_{S1}^{(lum)} &= M_{S1} = 1.0270 \\ J_{4L}^{(lum)} &= M_{4L} = 1.0270 \\ J_{12}^{(lum)} &= M_{12} = 0.8851 \\ J_{34}^{(lum)} &= M_{34} = 0.8851 \\ J_{14}^{(lum)} &= M_{14} = -0.1158 \\ J_{23}^{(lum)} &= M_{23} = 0.7460 \end{aligned}$$

The four LC resonators will have the same values and can be calculated following (2.2), thus obtaining $L = 0.02984$ pH and $C = 5.895$ nF.

To synthesize the distributed model (see Figure 2.4), the value of the cavity radius is needed, which has been chosen to be equal to 11.7 mm, since it allows a wide resonance-free frequency range around the center frequency of the filter. With this radius, the guide-wavelength fractional bandwidth is

$$\mathcal{W}_\lambda = 2\frac{\lambda_{g1} - \lambda_{g2}}{\lambda_{g1} + \lambda_{g2}} = 0.0037 \quad (0.37\%)$$

where λ_{g1} and λ_{g2} are the guide-wavelengths at the lower and upper band edge, respectively.

The inverter values in the distributed model can be obtained with (2.18), and are normalized with respect to the input/output impedance (i.e. $Z_{ref} = Z_0 = 1\,(\Omega)$).

$$\begin{aligned}
\bar{K}_{S1}^{(dis)} &= 0.1356 \\
\bar{K}_{4L}^{(dis)} &= 0.1356 \\
\bar{J}_{12}^{(dis)} &= 0.0154 \\
\bar{J}_{34}^{(dis)} &= 0.0154 \\
\bar{K}_{14}^{(dis)} &= -0.0020 \\
\bar{K}_{23}^{(dis)} &= 0.0130
\end{aligned}$$

The transmission lines of the distributed model must be able to take into account the waveguide dispersion. A possible way to include these lines in the circuit of the distributed element model is by means of a T-network equivalent circuit. Another possibility is to simulate the waveguide with a single EM mode. However it is done, the length of each transmission line section, equivalent to half a cavity, will be

$$l = \frac{1}{\beta}\phi = \lambda_g \frac{\phi}{2\pi} = 24.02 \text{ mm}$$

where $\phi = 3\pi/2$ since the TE_{113} mode is considered.

Following the procedure described in section 2.4, the physical dimensions of the filter can be obtained. For the input/output ports, the WR-75 standard waveguide ($a = 19.05$ mm and $b = 9.525$ mm) has been employed.

The dimensions of the input/output irises and cruciform inner iris are detailed in Table 2.5 (see Figure 2.12). The thickness t of all the irises has been set to 2 mm. Note that, in this case, the width W was fixed (2 mm for the input/output irises and 1 mm for the cruciform iris), while the length L was the only dimension to be adjusted in order to achieve the required coupling.

The length of the two cavities and the penetrations of the 6 screws can be found in Table 2.6. The screws have been simulated with a square section of 2×2 mm. As it can be appreciated, the two cavities in the filter are electromagnetically symmetric (i.e. the relative positions between the different screws and the irises are the same in

Dimensions (mm)	L (mm)	W (mm)
Input iris	9.160	2.000
Output iris	9.160	2.000
Cruciform iris: horizontal arm	3.809	1.000
Cruciform iris: vertical arm	6.489	1.000

Table 2.5 Dimensions of the irises in the four-pole dual-mode filter example.

Dimensions (mm)	Cavity 1	Cavity 2
Penetration of vertical screw	1.000	1.000
Penetration of horizontal screw	2.433	2.433
Penetration of oblique screw	1.570	1.570
Cavity length	47.487	47.487

Table 2.6 Dimensions of the screws and the cavities in the four-pole dual-mode filter example.

	Cavity 1	Cavity 2
Vertical screw	90°	90°
Horizontal screw	0°	180°
Oblique screw	45°	135°

Table 2.7 Position of the screws in the four-pole dual-mode filter example (see Figure A.4).

both cavities). Indeed, the positions of the screws have been chosen to achieve that symmetry, while maintaining the required 90°difference between the two oblique screws. The positions of the six screws have been detailed in Table 2.7, while the description of the position angles can be seen in Figure A.4.

Figure 2.33 shows the response of the EM model of the designed filter in comparison with the response of the distributed model. As it can be seen, both responses are very close, even though no optimization process has been applied.

The previously designed four-pole dual-mode filter, as well as the eight-pole filter example presented in the following section, have both been designed in a completely automatic way. A software tool which is able to automatically design CWDM filters has been developed, and it is currently included in the commercial EM software code FEST3D [23]. All the details and characteristics of this synthesis tool have been explained in appendix A.

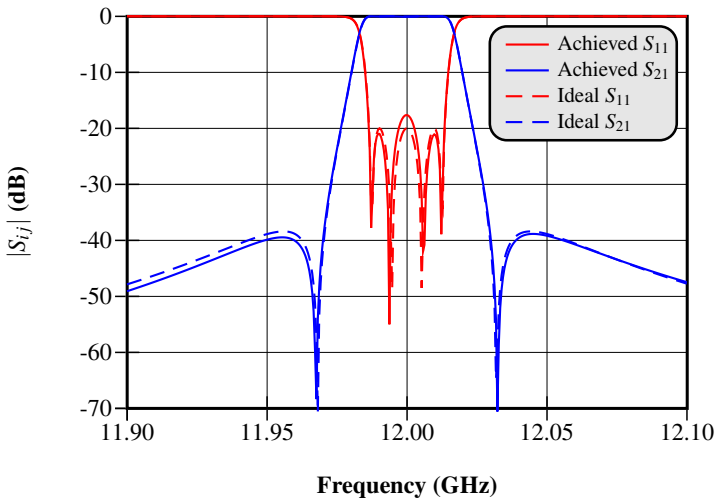

Figure 2.33 EM and distributed model responses of the four-pole dual-mode filter example.

2.7.2 Symmetric Eight-Pole Filter

The specifications for the eight-pole filter to be designed are detailed below:

- Order: $N = 8$
- Center frequency: $f_0 = 12$ GHz
- Bandwidth: $BW = 72$ MHz
- Return loss: $RL = 20$ dB
- Stopband rejection: > 60 dB
- Resonant mode inside the cavities: TE_{113}

In this case, the filter response presents two pairs of transmission zeros. The first pair will be placed at frequencies 11.95 GHz and 12.05 GHz, and the second pair at 11.93 GHz and 12.07 GHz.

The $N + 2$ folded CM is first obtained from the filter specifications:

$$M = \begin{pmatrix} 0 & 0.9867 & 0 & 0 & 0 & 0 & 0 & 0 & 0 & 0 \\ 0.9867 & 0 & 0.8153 & 0 & 0 & 0 & 0 & 0 & 0 & 0 \\ 0 & 0.8153 & 0 & 0.5855 & 0 & 0 & 0 & -0.0135 & 0 & 0 \\ 0 & 0 & 0.5855 & 0 & 0.5196 & 0 & 0.1816 & 0 & 0 & 0 \\ 0 & 0 & 0 & 0.5196 & 0 & -0.6995 & 0 & 0 & 0 & 0 \\ 0 & 0 & 0 & 0 & -0.6995 & 0 & 0.5196 & 0 & 0 & 0 \\ 0 & 0 & 0 & 0.1816 & 0 & 0.5196 & 0 & 0.5855 & 0 & 0 \\ 0 & 0 & -0.0135 & 0 & 0 & 0 & 0.5855 & 0 & 0.8153 & 0 \\ 0 & 0 & 0 & 0 & 0 & 0 & 0 & 0.5855 & 0 & 0.9867 \\ 0 & 0 & 0 & 0 & 0 & 0 & 0 & 0 & 0.9867 & 0 \end{pmatrix}$$

The previous matrix needs to be transformed following the procedure explained in section 2.6.5, thus obtaining

$$M = \begin{pmatrix} 0 & 0.9867 & 0 & 0 & 0 & 0 & 0 & 0 & 0 & 0 \\ 0.9867 & 0 & 0.8051 & 0 & -0.1281 & 0 & 0 & 0 & 0 & 0 \\ 0 & 0.8051 & 0 & 0.6702 & 0 & 0 & 0 & 0 & 0 & 0 \\ 0 & 0 & 0.6702 & 0 & 0.5252 & 0 & -0.0143 & 0 & 0 & 0 \\ 0 & -0.1281 & 0 & 0.5252 & 0 & 0.5458 & 0 & 0 & 0 & 0 \\ 0 & 0 & 0 & 0 & 0.5458 & 0 & 0.5252 & 0 & -0.1281 & 0 \\ 0 & 0 & 0 & -0.0143 & 0 & 0.5252 & 0 & 0.6702 & 0 & 0 \\ 0 & 0 & 0 & 0 & 0 & 0 & 0.6702 & 0 & 0.8051 & 0 \\ 0 & 0 & 0 & 0 & 0 & -0.1281 & 0 & 0.8051 & 0 & 0.9867 \\ 0 & 0 & 0 & 0 & 0 & 0 & 0 & 0 & 0.9867 & 0 \end{pmatrix}$$

Since the center frequency of the filter is the same as in the previous four-pole filter example, the cavity radius has been chosen to have the same value, so it will be equal to 11.7 mm. With this radius, the fractional bandwidth in terms of guide-wavelength will be

$$\mathcal{W}_\lambda = 2\frac{\lambda_{g1} - \lambda_{g2}}{\lambda_{g1} + \lambda_{g2}} = 0.0099 \quad (0.99\%)$$

The normalized inverter values in the distributed model (see Figure 2.22) are obtained from the CM using (2.26)

$$\begin{aligned} \bar{K}_{S1} &= \bar{K}_{8L} = 0.2127 \\ \bar{J}_{12} &= \bar{J}_{78} = 0.0374 \\ \bar{K}_{23} &= \bar{K}_{67} = 0.0311 \\ \bar{J}_{34} &= \bar{J}_{56} = 0.0244 \\ \bar{K}_{36} &= -0.0007 \\ \bar{K}_{14} &= \bar{K}_{58} = -0.0060 \\ \bar{K}_{45} &= 0.0254 \end{aligned}$$

Dimensions (mm)	L (mm)	W (mm)
Input iris	9.927	2.000
Output iris	9.927	2.000
Cruciform iris 1: horizontal arm	5.258	1.000
Cruciform iris 1: vertical arm	8.034	1.000
Cruciform iris 2: horizontal arm	7.691	1.000
Cruciform iris 2: vertical arm	2.758	1.000
Cruciform iris 3: horizontal arm	5.258	1.000
Cruciform iris 3: vertical arm	8.034	1.000

Table 2.8 Dimensions of the irises in the eight-pole dual-mode filter example.

Dimensions (mm)	Cavity 1	Cavity 2	Cavity 3	Cavity 4
Penetration of vertical screw	1.000	1.000	1.000	1.000
Penetration of horizontal screw	2.745	1.003	1.003	2.745
Penetration of oblique screw	2.353	1.849	1.849	2.353
Cavity length	47.110	47.753	47.753	47.110

Table 2.9 Dimensions of the screws and the cavities in the eight-pole dual-mode filter example.

Because the chosen radius, EM mode and center frequency of the filter are the same ones as in the previous example, the length of each transmission line section in the distributed model will be the same.

The WR-75 standard waveguide has also been selected for the input/output ports of this example, and the irises thickness has been set at 2 mm. The rest of the irises dimensions are detailed in Table 2.8, where cruciform iris 1 refers to the iris between cavities 1 and 2, cruciform iris 2 to the one between cavities 2 and 3, and cruciform iris 3 to the iris between cavities 3 and 4. As it can be seen, since the filter has a symmetric structure, dimensions of irises 1 and 3 are the same.

The dimensions of the four cavities and their screws can be found in Table 2.9, where the symmetry can also be appreciated. The positions of the screws are detailed in Table 2.10.

The responses of both EM model and distributed model are shown in Figure 2.34, where it can be seen that the results obtained for this second example are also very good. Again, no optimization process has been applied.

	Cavity 1	Cavity 2	Cavity 3	Cavity 4
Vertical screw	90°	90°	90°	90°
Horizontal screw	0°	180°	0°	180°
Oblique screw	45°	135°	45°	135°

Table 2.10 Position of the screws in the eight-pole dual-mode filter example (see Figure A.4).

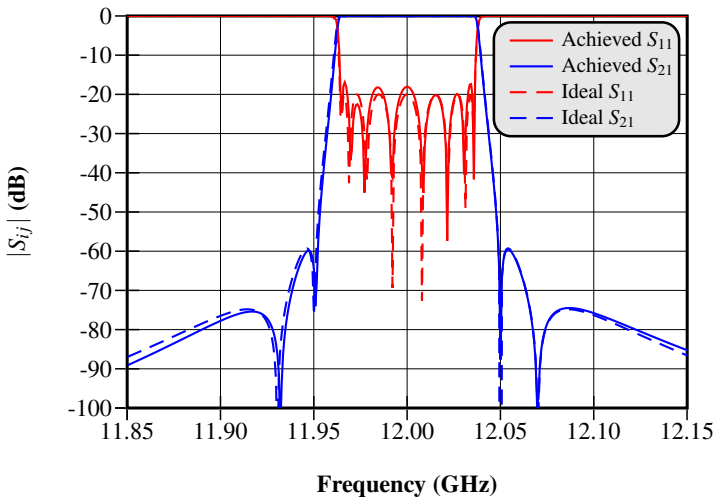

Figure 2.34 EM model and distributed model responses of the eight-pole dual-mode filter example.

REFERENCES

1. S. Cogollos, M. Brumos, V.E. Boria, C. Vicente, J. Gil, B. Gimeno, and M. Guglielmi. A systematic design procedure of classical dual-mode circular waveguide filters using an equivalent distributed model. In *Microwave Theory and Techniques, IEEE Transactions on*, volume 60, pages 1006–1017, April 2012.
2. S. Cogollos, M. Brumos, V.E. Boria, C. Vicente, B. Gimeno, and M. Guglielmi. New distributed model for synthesis of classical dual mode filters. In *Microwave Symposium Digest (MTT), 2010 IEEE MTT-S International*, pages 437–440, May 2010.
3. A E. Williams. A four-cavity elliptic waveguide filter. In *Microwave Symposium, G-MTT 1970 International*, pages 90–93, May 1970.
4. A.E. Atia and A.E. Williams. New types of waveguide bandpass filters for satellite transponders. In *Comsat Tech. Rev.*, volume 1, pages 21–43, Fall 1971.
5. A.E. Atia and A.E. Williams. Narrow-bandpass waveguide filters. In *Microwave Theory and Techniques, IEEE Transactions on*, volume 20, pages 258–265, Apr 1972.
6. C. Kudsia, R. Cameron, and Wai-Cheung Tang. Innovations in microwave filters and multiplexing networks for communications satellite systems. In *Microwave Theory and Techniques, IEEE Transactions on*, volume 40, pages 1133–1149, 1992.
7. A.E. Atia, A.E. Williams, and R.W. Newcomb. Narrow-band multiple-coupled cavity synthesis. In *Circuits and Systems, IEEE Transactions on*, volume 21, pages 649–655, Sep 1974.
8. D. Rosowsky. Design of manifold type multiplexers. In *Proc. ESA Workshop on Microwave Filters*, pages 145–156, Jun 1990.

9. J.R. Montejo-Garai and J. Zapata. Full-wave design and realization of multicoupled dual-mode circular waveguide filters. In *Microwave Theory and Techniques, IEEE Transactions on*, volume 43, pages 1290–1297, Jun 1995.
10. W. Hauth, D. Schmitt, and M. Guglielmi. Accurate modelling of narrow-band filters for satellite communications. In *Microwave Symposium Digest. 2000 IEEE MTT-S International*, volume 3, pages 1767–1770, June 2000.
11. H. Hu and K.L. Wu. An automated design technique for asynchronously-tuned circular waveguide dual-mode filters. In *Microwave Conference Proceedings (APMC), 2010 Asia-Pacific*, pages 1970–1973, Dec 2010.
12. H. Hu, K.L. Wu, and R.J. Cameron. A design technique for stepped circular waveguide dual-mode filters for broadband contiguous multiplexers. In *Microwave Symposium Digest (MTT), 2011 IEEE MTT-S International*, pages 1–4, June 2011.
13. M. Bekheit, S. Amari, and F. Seyfert. A new approach to canonical dual-mode cavity filter design. In *Microwave Theory and Techniques, IEEE Transactions on*, volume 57, pages 1196–1206, May 2009.
14. S. B. Cohn. Direct-coupled-resonator filters. In *Proceedings of the IRE*, volume 45, pages 187–196, Feb 1957.
15. G.L. Matthaei, L. Young, and E.M.T. Jones. *Microwave Filters, Impedance-Matching Networks, and Coupling Structures*. Artech House. McGraw-Hill, 1964.
16. L. Young. Direct-coupled cavity filters for wide and narrow bandwidths. In *Microwave Theory and Techniques, IEEE Transactions on*, volume 11, pages 162–178, May 1963.
17. J.D. Rhodes. The generalized direct-coupled cavity linear phase filter. In *Microwave Theory and Techniques, IEEE Transactions on*, volume 18, pages 308–313, Jun 1970.
18. J.D. Rhodes. *Theory of Electrical Filters.* Wiley, 1976.
19. R. Levy. Theory of direct-coupled-cavity filters. In *Microwave Theory and Techniques, IEEE Transactions on*, volume 15, pages 340–348, Jun 1967.
20. F.M. Vanin, D. Schmitt, and R. Levy. Dimensional synthesis for wide-band waveguide filters and diplexers. In *Microwave Theory and Techniques, IEEE Transactions on*, volume 52, pages 2488–2495, Nov 2004.
21. P. Soto, E. Tarín, V.E. Boria, C. Vicente, J. Gil, and B. Gimeno. Accurate synthesis and design of wideband and inhomogeneous inductive waveguide filters. In *Microwave Theory and Techniques, IEEE Transactions on*, volume 58, pages 2220–2230, Aug 2010.
22. R.J. Cameron, C.M. Kudsia, and R.R. Mansour. *Microwave Filters for Communication Systems: Fundamentals, Design and Applications*. Wiley, 2007.
23. FEST3D 6.8.4 Aurora Software and Testing, S.L. (on behalf of ESA/ESTEC), Valencia, Spain, 2013. Available: www.fest3d.com.
24. S. Amari, J. Bornemann, W. Menzel, and F. Alessandri. Diplexer design using pre-synthesized waveguide filters with strongly dispersive inverters. In *Microwave Symposium Digest, 2001 IEEE MTT-S International*, volume 3, pages 1627–1630, May 2001.
25. L.Q. Bui, D. Ball, and T. Itoh. Broad-band millimeter-wave E-plane bandpass filters (short papers). In *Microwave Theory and Techniques, IEEE Transactions on*, volume 32, pages 1655–1658, Dec 1984.

CHAPTER 3

CORRECTION OF MANUFACTURING DEVIATIONS IN CWDM FILTERS WITHOUT TUNING SCREWS

Tuning screws are commonly used in waveguide filters to compensate for small errors produced during the fabrication process. However, the use of tuning screws has some disadvantages, because the small gaps between the screws and the holes are prone to create PIM and RF breakdown effects, and are also the source of potential radiation losses [1–3]. Besides, it is known that, for space applications, fixed structures are generally preferred against others with mobile parts, because non-fixed parts can be moved due to vibration during the launching operation. For all these reasons, an alternative technique has been developed to correct manufacturing deviations, in which tuning screws are not necessary. In this case, the correction is made by means of substituting some pieces of the fabricated filter for new ones, which are able to correct those deviations. These pieces are quite cheap and easy to manufacture. In order to find the dimensions of the new pieces, an space mapping (SM) technique is applied [4]. This method has been particularized to correct the fabrication deviations in circular-waveguide dual-mode (CWDM) filters, although it could be easily extended to other filter topologies.

3.1 Background

Space mapping techniques were introduced to design microwave components in [5]. Since then, the idea has been successfully applied in different works with some specific variations [6–10]. The space mapping algorithms are usually employed to design microwave devices in a more efficient way, by combining the efficiency of circuit models with the accuracy of electromagnetic (EM) models [5, 6]. A fast low-accuracy model (usually a circuit model) is used as a "coarse model", while a high-precision model (usually obtained with an EM simulator) is employed as a "fine model". The final aim is to obtain an optimal design given by the fine model without performing direct optimization over the fine model. Instead, many simulations of the coarse model are combined with a few simulations of the fine model, thus establishing a relationship (mapping) between both models.

In this work, the space mapping technique has been applied in an alternative way. It has been used to correct typical manufacturing deviations appearing in circular-waveguide dual-mode filters, avoiding the need of including tuning screws in the filter structure.

Tuning screws are commonly used in waveguide filters to compensate for small errors produced during the fabrication process. However, the use of tuning screws has some disadvantages. First of all, they may cause problems dealing with high power signals, specially in space applications, since the small gaps along the threads between the screws and the holes, together with the contamination (metal shavings, dirt, etc) on the surface of the screws, are likely to create passive intermodulation (PIM) and multipaction effects [3]. These gaps may also create potential radiation losses in the structure. Besides, it is known that, for space applications, fixed structures are generally preferred against others with mobile parts, because non-fixed parts can be moved due to vibration effects (i.e. those generated during the launching operation). Furthermore, the tuning process of these screws is usually a time consuming task, and must be carried out by an expert operator. For all these reasons, many authors have tried to avoid the use of tuning screws in the design and manufacturing of dual-mode filters [1–3].

The method is going to be applied over a CWDM filter, in which the tuning and coupling screws have been replaced by fixed rectangular-shaped insertions. After designing the filter using an EM solver, it has been manufactured and then measured, obtaining a real response which is different to the simulated one, due to manufacturing tolerances. Since the filter structure has been divided into several pieces, those with rectangular-shaped insertions can be easily replaced with new ones. A series of pieces with new insertions will be designed using a space mapping technique, and then fabricated again, in order to progressively achieve the desired response.

3.2 Manufactured Prototype

Let us consider a four-pole CWDM filter with the structure shown in Figure 3.1. It can be seen that the tuning and coupling screws have been replaced by squared

insertions. The filter has a center frequency $f_0 = 10.5$ GHz and a bandwidth $BW = 27$ MHz. It has been designed using the technique explained in chapter 2, and the simulated EM response of the filter is shown in Figure 3.2 (solid line).

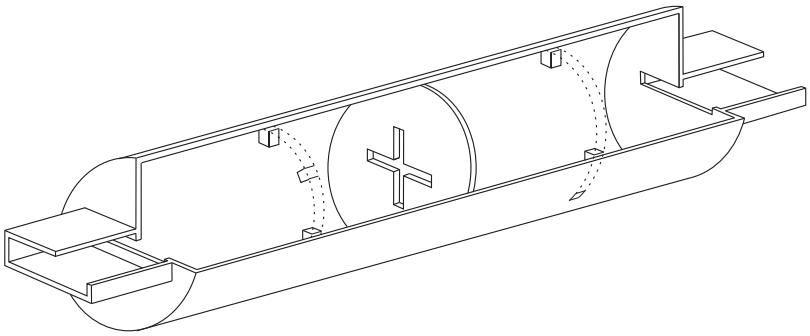

Figure 3.1 Physical structure of a four-pole CWDM filter with squared insertions.

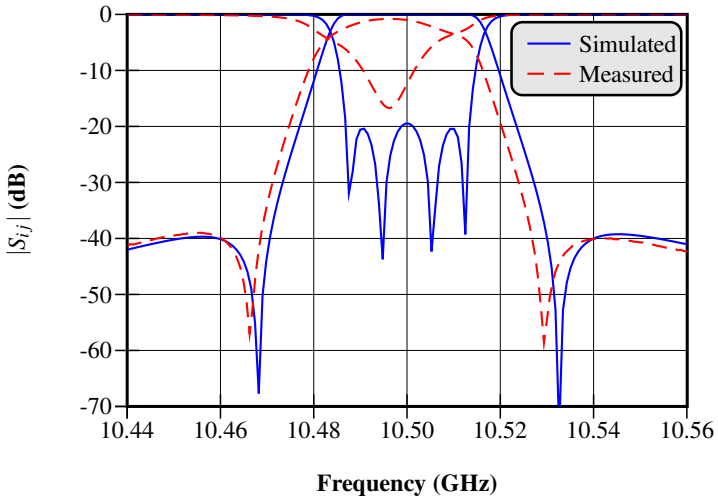

Figure 3.2 Ideal response obtained with a full-wave EM solver (FEST3D) compared with the measured response of the manufactured filter.

The filter was manufactured (see Figure 3.3) and then measured, thus obtaining the response shown in Fig. 3.2 (dashed line). It can be appreciated that the response of the fabricated filter is quite different from the simulated one. These differences are due to the manufacturing tolerances (about 10 microns in our case), which can lead to large variations in the response of very sensitive filters like this one (very narrow bandwidth at Ku-band).

As it can be seen in Figure 3.4, the whole filter structure has been divided into 5 separate pieces. The manufactured separate pieces are shown in Figure 3.5.

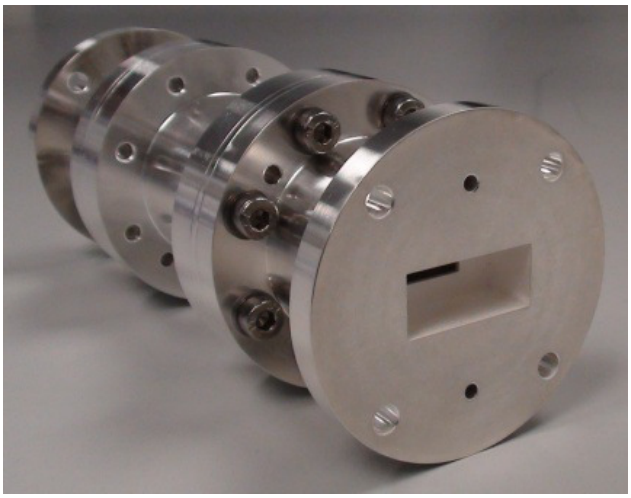

Figure 3.3 Manufactured filter with all its pieces assembled together.

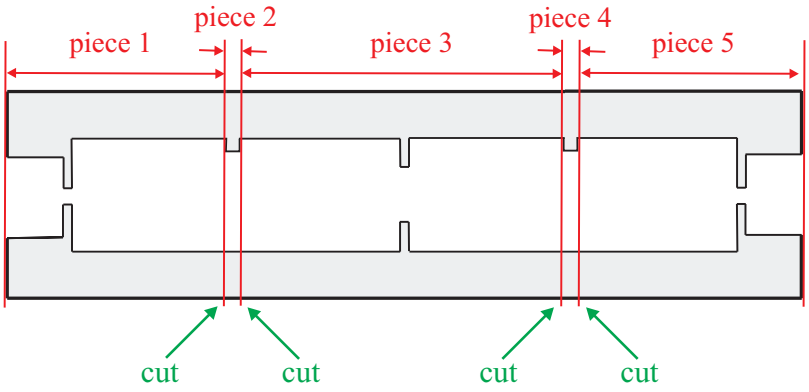

Figure 3.4 Side cut of the structure of the manufactured filter divided into 5 pieces.

3.3 Space Mapping Technique

An SM technique is going to be applied in order to calculate the penetrations of the insertion pieces in the two cavities. The procedure to obtain the new dimensions is going to be described along the following sections.

3.3.1 Fine and Coarse Models

In the proposed SM application, the coarse model is the commercial full-wave EM solver FEST3D [11], but any other software capable of coping with the full-wave EM analysis of the proposed complex structures, in reasonable CPU times, could be

Figure 3.5 Detailed view of the pieces composing the filter in Fig. 3.3.

used instead. The fine model responses are the measurements of the manufactured CWDM filter, which are obtained with a vector network analyzer (Agilent E8364B, 10 MHz to 50 GHz).

3.3.2 Space Mapping Parameters

The only parameters that are going to be modified during the SM process are the penetration depths (L variables in Fig. 3.6) of the 6 rectangular-shaped metal insertions.

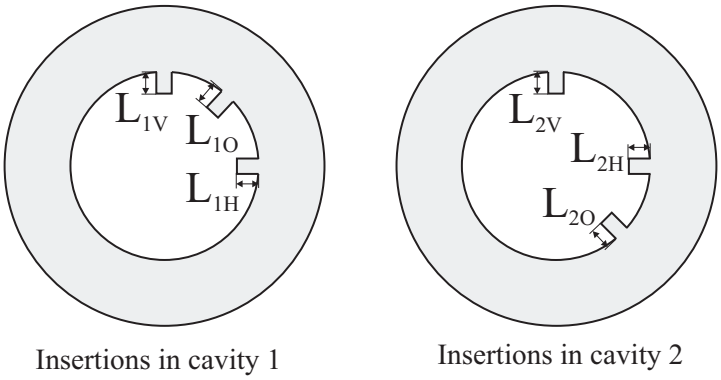

Figure 3.6 Pieces with insertions allocated in the middle of each cavity.

After each SM iteration, the length of the 6 insertions will be obtained, and the corresponding two pieces (i.e. pieces 2 and 4 in Fig. 3.4) will be fabricated again.

3.3.3 Formulation

In this case, the aggressive space mapping (ASM) technique has been employed [6]. The ASM is a version of the classical SM technique [5] where less simulations of the fine model are needed, thus resulting in a very efficient algorithm.

Following the method explained in [6], the length values to be fabricated in each iteration are calculated as follows

$$\mathbf{L}_f^{(j)} = \mathbf{L}_f^{(j-1)} + \mathbf{h}^{(j)} \tag{3.1}$$

where $\mathbf{L}_f^{(j)}$ are the lengths of the fine model in the j-th iteration, and $\mathbf{h}^j$ is the new increment for each new iteration that can be obtained as indicated next

$$\mathbf{h}^{(j)} = -(\mathbf{B}^{(j)})^{-1}\mathbf{f}^{(j)} \tag{3.2}$$

In the previous equation, $\mathbf{B}^{(j)}$ denotes the corresponding Jacobian matrix, also described in [6], that can be obtained by means of the classical Broyden update

$$\mathbf{B}^{(j)} = \mathbf{B}^{(j-1)} + \frac{\mathbf{f}^{(j)}\mathbf{h}^{(j-1)T}}{\mathbf{h}^{(j-1)T}\mathbf{h}^{(j-1)}} \tag{3.3}$$

and $\mathbf{f}^{(j)}$ can be calculated as

$$\mathbf{f}^{(j)} = \mathbf{L}_c^{(j)} - \mathbf{L}_c^{(0)} \tag{3.4}$$

where $\mathbf{L}_c^{(j)}$ and $\mathbf{L}_c^{(0)}$ are the dimensions in the coarse model for the j-th iteration and for the optimal solution (the insertion dimensions of the originally designed filter), respectively.

For the particular case of the first iteration, given that there is no information available to build the Jacobian matrix, the identity matrix is used instead.

3.4 Correction Process

Once the original filter has been designed and fabricated, its response is measured. When this response is significantly different from the desired one (see Figure 3.2), the correction process starts.

In order to perform the first iteration, the first step is to obtain six new dimensions in the coarse model ($\mathbf{L}_c^{(1)}$). This is done by obtaining, with the full-wave EM software code, a response that matches the previously measured response (dashed line in Figure 3.2). This can be done by optimizing the original design, only modifying the penetration lengths of the 6 metal insertions. Since the full-wave EM simulation tool employed to perform the optimization (FEST3D) is very efficient, and there are only

6 optimization parameters, the optimization process is quite fast (less than 1 hour with an AMD 3-core @ 2.6GHz, with 4GB RAM). Figure 3.7 shows the measured response compared with the optimized simulated response.

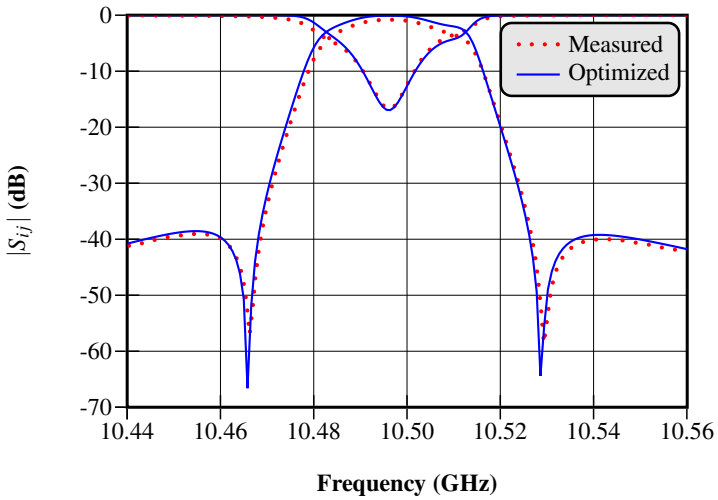

Figure 3.7 Optimization of the EM model to match the measured response in the first SM iteration.

The new penetrations of the coarse model $\mathbf{L}_c^{(1)}$ obtained after the optimization process are introduced in (3.1)-(3.4) to obtain the new 6 penetration values of the fine model $\mathbf{L}_f^{(1)}$, which correspond with the dimensions of the two new pieces that will be manufactured.

The next step is to measure the filter response after substituting the two original insertion pieces with the ones designed in the first SM iteration. If the new measured response is not close enough to the desired one, a second SM iteration can be performed. In this case, the response measured after the first SM iteration will be matched with the optimizer to obtain $\mathbf{L}_c^{(2)}$.

The whole process can be repeated until the desired response is achieved, or until there are not significant improvements between iterations (see section 3.6).

3.5 Results

For the sake of validation, three SM iterations have been performed over the CWDM filter considered, following the method explained in section 3.4. The insertion pieces manufactured along the correction process (the ones of the original prototype plus the three SM iterations) can be seen in Figure 3.8. Since there are two cavities, and each cavity has an insertion piece, a total of 8 insertion pieces have been manufactured. The pieces manufactured after the three SM iteration were fabricated without silver plating, in order to achieve a better accuracy (manufacturing tolerances of about 5

	Iteration 0		Iteration 1		Iteration 2		Iteration 3	
	$L_c^{(0)}$	$L_f^{(0)}$	$L_c^{(1)}$	$L_f^{(1)}$	$L_c^{(2)}$	$L_f^{(2)}$	$L_c^{(3)}$	$L_f^{(3)}$
L_{1V}	2.000	2.000	2.275	1.725	2.133	1.522	1.976	1.559
L_{1H}	3.145	3.145	3.226	3.063	3.172	3.022	3.123	3.042
L_{1O}	2.250	2.250	2.360	2.141	2.253	2.138	2.206	2.170
L_{2V}	2.000	2.000	1.971	2.029	2.077	1.911	1.907	1.989
L_{2H}	3.134	3.134	3.119	3.150	3.154	3.119	3.107	3.142
L_{2O}	1.707	1.707	1.642	1.772	1.739	1.724	1.757	1.692

Table 3.1 Penetration lengths obtained during the correction process.

microns, against a tolerance of about 10 microns if silver plating is applied). The penetration lengths obtained in the different iterations are detailed in Table 3.1.

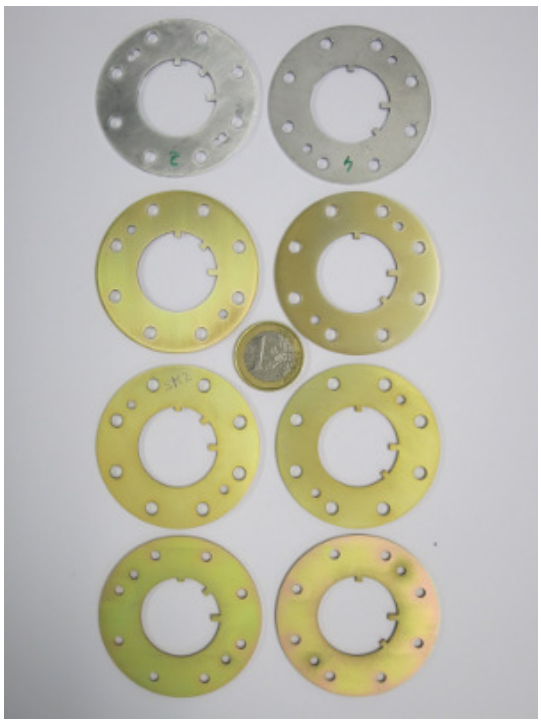

Figure 3.8 Insertion pieces of the original prototype and the three SM iterations (from top to bottom: original prototype, 1st SM iteration, 2nd SM iteration and 3rd SM iteration).

The measured responses of the filter with the pieces obtained after each iteration are shown in Figure 3.9. As it can be seen, the improvement of the response of the first iteration, with regard to the one of the original manufactured prototype, is

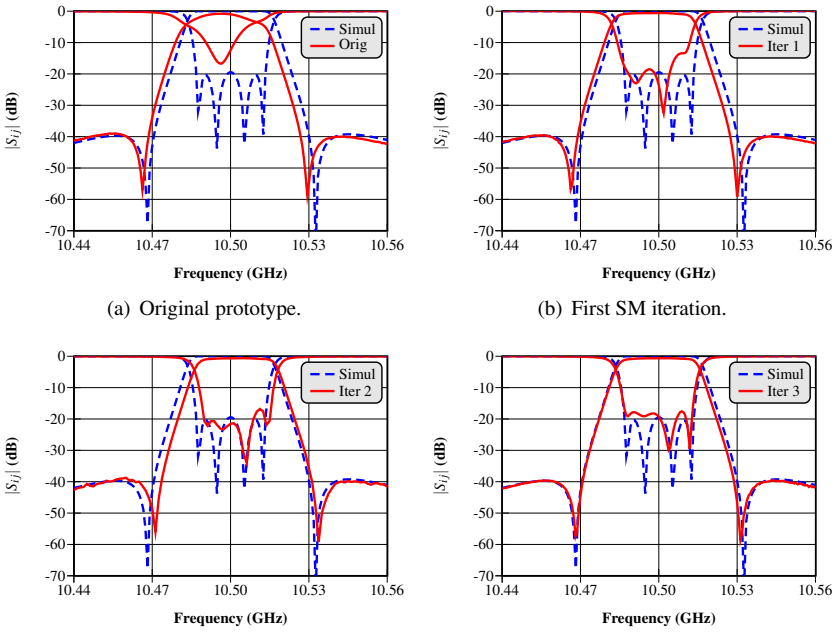

(a) Original prototype.

(b) First SM iteration.

(c) Second SM iteration.

(d) Third SM iteration.

Figure 3.9 Simulated response vs measured response of the original prototype and the 3 SM iterations.

already considerable. The differences between iterations one and two are also quite important, achieving a better return loss value after the second iteration. Finally, the last iteration has been able to correct almost perfectly the existing frequency shift, thus achieving a response that is very close (almost identical) to the ideal one. For the sake of a better comparison, all the responses have been put together in Figure 3.10.

In order to better verify the effectiveness of the method, the final response has been represented together with the ideal EM simulated response and the measurements of the original prototype (see Figure 3.11). The improvement between the response of the original manufactured prototype and the response of the last SM iteration is clearly observed.

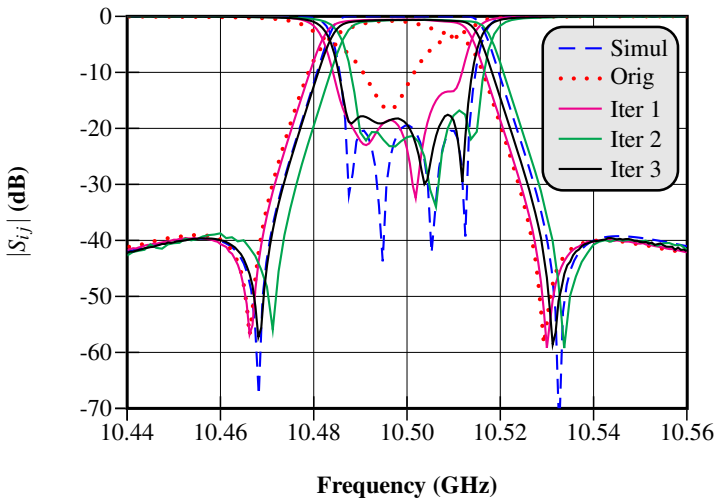

Figure 3.10 Measured responses after each iteration compared with the simulated response and the original fabrication.

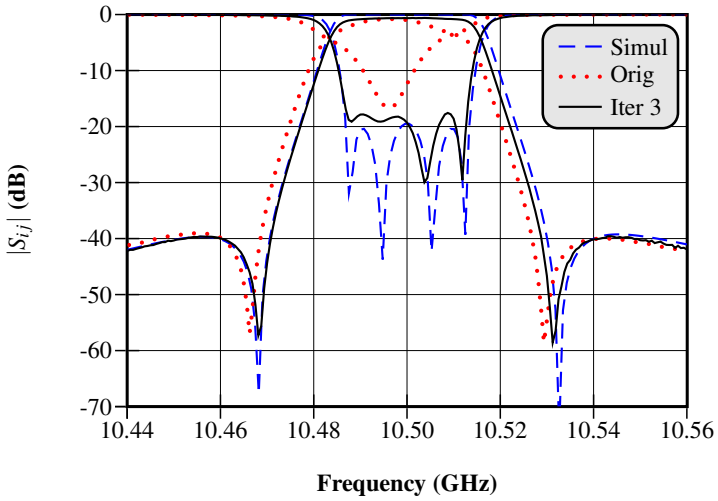

Figure 3.11 Comparison between the responses of the original prototype and the last SM iteration, together with the desired ideal response.

3.6 Practical Considerations

3.6.1 Minimum Penetrations in the Insertion Pieces

In the same way that it happens with filters with tunning screws, the insertion penetrations must be long enough to allow the correction of the fabricated filter, according

to the expected manufacturing tolerances. It means that, if very short insertions are chosen for the initial fabricated filter, it can occur that if, for example, there is a very high frequency displacement towards lower frequencies in the initial manufactured prototype, the tuning margin may not be enough to move the response to the desired center frequency (the penetration that can be achieved by any screw cannot be lower than zero). Therefore, it is advisable to perform a tolerance analysis, in order to find out the proper minimum penetrations of the insertions in the initial filter design.

3.6.2 Alignment Pins

It has been observed that small variations in the position of the different pieces when they are assembled together can lead to significant changes in the measured response. Because of that, it is very important to fix the position of the pieces by means of alignment pins. These pins must be included in every place where various pieces are joint together. Figure 3.12 shows the two pins employed to join each insertion piece with the adjacent waveguides.

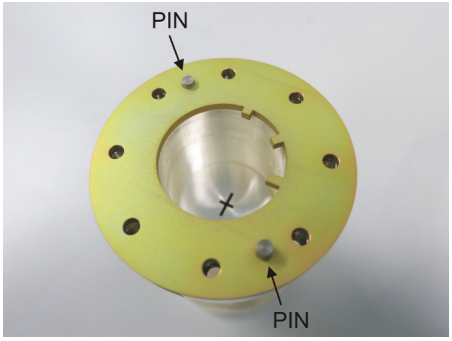

Figure 3.12 Alignment pins to assure that the position of the pieces is always the same.

3.6.3 Manufacturing Tolerances in the SM Pieces

The proposed method is meant for the correction of the filter response, which has been deteriorated due to the manufacturing deviations in the whole structure. However, the insertion pieces fabricated in each iteration are not perfectly fabricated either. Because of that, a totally perfect response is never going to be achieved (except for a matter of chance). Nevertheless, due to mechanical reasons, the accuracy that can be obtained in the fabrication of the pieces with insertions is significantly higher than the accuracy that can be achieved in the rest of the structure, so the final result, if not perfect, can be very close to the ideal one.

3.6.4 Correction Capability of the Insertion Pieces

This technique will only be able to correct those manufacturing problems that can be compensated with the circuit parts considered in the process (in this case the rectangular insertions). For the CWDM filter considered here, the best achievable result would be similar to the one obtained in the tuning process of a CWDM filter, where real tuning and coupling screws are used instead of the rectangular-shaped insertions. This means that if, for example, there are important errors in the fabrication of the irises, which could lead to a significant variation of the filter bandwidth, it may not be possible to correct the response deviations perfectly. Nevertheless, given that case, the technique would be able to significantly improve the initial response of the original manufactured filter.

REFERENCES

1. M. Guglielmi, R. C. Molina, and A. Alvarez. Dual-mode circular waveguide filters without tuning screws. In *Microwave and Guided Wave Letters, IEEE*, volume 2, pages 457–458, Nov 1992.
2. L. Accatino, G. Bertin, and M. Mongiardo. A four-pole dual mode elliptic filter realized in circular cavity without screws. In *Microwave Theory and Techniques, IEEE Transactions on*, volume 44, pages 2680–2687, Dec 1996.
3. K.L. Wu. An optimal circular-waveguide dual-mode filter without tuning screws. In *Microwave Theory and Techniques, IEEE Transactions on*, volume 47, pages 271–276, Mar 1999.
4. M. Brumos, V.E. Boria, M. Guglielmi, and S. Cogollos. Correction of manufacturing deviations in circular-waveguide dual-mode filters using aggressive space mapping. In *Microwave Conference, 2014. 44th European*, Oct 2014.
5. J.W. Bandler, R. Biernacki, Shao Hua Chen, P.A. Grobelny, and R.H. Hemmers. Space mapping technique for electromagnetic optimization. In *Microwave Theory and Techniques, IEEE Transactions on*, volume 42, pages 2536–2544, Dec 1994.
6. J.W. Bandler, R. Biernacki, Shao Hua Chen, R.H. Hemmers, and K. Madsen. Electromagnetic optimization exploiting aggressive space mapping. In *Microwave Theory and Techniques, IEEE Transactions on*, volume 43, pages 2874–2882, 1995.
7. J.W. Bandler, Q.S. Cheng, S.A. Dakroury, A.S. Mohamed, M.H. Bakr, K. Madsen, and J. Sondergaard. Space mapping: the state of the art. In *Microwave Theory and Techniques, IEEE Transactions on*, volume 52, pages 337–361, Jan 2004.

8. M.B. Steer, J.W. Bandler, and Christopher M. Snowden. Computer-aided design of RF and microwave circuits and systems. In *Microwave Theory and Techniques, IEEE Transactions on*, volume 50, pages 996–1005, Mar 2002.

9. K.L. Wu, Y.J. Zhao, J. Wang, and M.K.K. Cheng. An effective dynamic coarse model for optimization design of LTCC RF circuits with aggressive space mapping. In *Microwave Theory and Techniques, IEEE Transactions on*, volume 52, pages 393–402, Jan 2004.

10. S. Amari, C. LeDrew, and W. Menzel. Space-mapping optimization of planar coupled-resonator microwave filters. In *Microwave Theory and Techniques, IEEE Transactions on*, volume 54, pages 2153–2159, May 2006.

11. FEST3D 6.8.4 Aurora Software and Testing, S.L. (on behalf of ESA/ESTEC), Valencia, Spain, 2013. Available: www.fest3d.com.

CHAPTER 4

DESIGN OF MANIFOLD MULTIPLEXERS WITH CWDM FILTERS USING DISTRIBUTED MODELS

This chapter is devoted to explain a novel technique to design manifold-coupled multiplexers in waveguide technology, whose channel filters are circular-waveguide dual-mode (CWDM) filters [1]. These classical multiplexers are very popular in satellite communication payloads. The proposed technique can be applied to multiplexers with a large number of both contiguous and non-contiguous channels. As it happens with the design procedure for individual CWDM filters explained in chapter 2, it makes use of distributed models for the synthesis of the channel filters, but the design method of such filters must be properly adapted to take into account the effect of the rest of the multiplexer structure. The process starts with the synthesis of a lumped model of the whole multiplexer, designing first its individual filters, and then performing a quick optimization over the multiplexer model to achieve the desired response. With the lumped model in hand, the distributed model can be obtained straightforwardly. This distributed model will be employed to extract the physical dimensions of the multiplexer.

4.1 Background

Multiplexers are passive devices employed to divide a wideband signal into several channels or, on the contrary, to combine the signal coming from multiple channels to form a wideband signal [2, 3]. They are typically composed of a certain number of filters connected together to form a complex structure. Microwave multiplexers find wide application in communication systems, such as satellite links or wireless base stations [2, 4, 5].

Between the different possibilities to implement microwave multiplexers (some of them making use of hybrids or circulators to connect the channel filters), manifold type multiplexers are the ones preferred in terms of losses, compactness and amplitude and group delay response [6–8], since they use a simple waveguide to connect the filters. However, due to this direct connection, there is a high interaction between the channel filters [6, 7, 9], which makes the design process much more complicated.

The classical techniques to design waveguide manifold multiplexers usually employ lumped-element models [7, 10]. Nevertheless, since they do not consider some effects of the real structures, such as their frequency dependence behavior, they commonly lead to an electromagnetic (EM) model whose response significantly differs from the desired one. Because of that, they require time-consuming optimizations of the full-wave EM model. In order to achieve a better starting point, hybrid procedures have been introduced, where some parts of the structure are replaced with full-wave EM models [11–13]. As an alternative, space mapping techniques linking analytical models with full-wave EM simulations were employed [6, 14–16], in order to reduce computational times while maintaining a high accuracy level.

The design technique proposed in this work uses distributed models of both the channel filters and the manifold, which are able to better represent the real behavior of the considered structures, while allowing faster simulations. Because of that, a very good starting point of the EM model is obtained in a low execution time, which only needs a slight optimization to achieve the desired final response.

4.2 Synthesis of the Lumped Model

4.2.1 Lumped Model of the Individual Filters

The first step in the procedure is to synthesize the lumped model of each individual filter in the multiplexer to fulfill the frequency specifications of the corresponding channel. In this work, the method has been particularized for CWDM filters, but it could be easily extended to other filter structures.

4.2.1.1 Filters in Non-Contiguous Channel Multiplexers The procedure to synthesize the lumped model of the individual filters is slightly different depending on the frequency separation between the multiplexer channels. A multiplexer is considered non-contiguous when the separation between channels (from the end of the band of one channel to the beginning of the band of the following channel) is greater

than the 25% of the separation between the center frequencies of two adjacent channels. Otherwise it is said to be contiguous. In non-contiguous channel multiplexers, the interactions between different channels are quite low, since the passband of each channel is clearly rejected by the rest of the channel filters. In this case, the channel filters may be designed, at this initial stage, as if they were independent and isolated. In other words, the channel filters are initially designed as doubly terminated networks. The procedure to obtain the coupling matrix of a doubly terminated network has been outlined in appendix B, while the synthesis of the lumped model of a CWDM filter is described in section 2.2.

4.2.1.2 Filters in Contiguous Channel Multiplexers

As the guard bands between the channel filters decrease, they begin to interact strongly along the manifold. Although it is possible to optimize doubly terminated filters to operate in a contiguous channel environment, a starting point much closer to the final optimal result is obtained if singly terminated filter prototypes are used. The method to design the lumped model of singly terminated filters is essentially the same as for doubly terminated filters, but the folded coupling matrix must be designed as singly terminated. The procedure to synthesize the coupling matrix for a singly terminated network has also been described in appendix B. In this case, the coupling matrix obtained will always be non-symmetric.

The singly terminated filter network is useful for the design of contiguous channel manifold multiplexers, because the contiguous singly terminated channel filters along the manifold tend to interact in a mutually beneficial manner, providing a conjugate match for each other. This natural multiplexing effect may be explained by studying the special characteristics of the input admittance of the singly terminated circuit, looking in at the port connected to the manifold (see Figure 4.1). As it can be seen, the real part of the input admittance is close to one over the filter passband, dropping to near zero in the out-of-band regions. If the contiguous-band singly terminated filters are connected to the manifold with the zero impedance termination closest to the manifold junction, then the negative in-band slope of the imaginary part will tend to cancel with the positive slopes of the two contiguous neighbors.

4.2.2 Multiplexer with the Lumped Model of the Filters

Once the lumped model of each isolated filter is obtained, all of them must be connected to the manifold. Figure 4.2 shows a simplified diagram of the multiplexer structure with the lumped model of each filter, which in this case are four-pole CWDM filters. The manifold waveguides, as well as the waveguides connecting the filters with the manifold, have been modeled with an equivalent π-network. The T-junctions are simulated electromagnetically (only one full-wave simulation is required) and their S-parameters are introduced in the circuit.

As explained in [6], the initial spacings between E or H-plane junctions must be set at $m\lambda_g/2$, where m is usually as low as possible in order to achieve a compact design and to minimize potential spurious. The spacing between the last junction and the short circuit must be $m\lambda_g/2$ for multiplexers with filters connected along

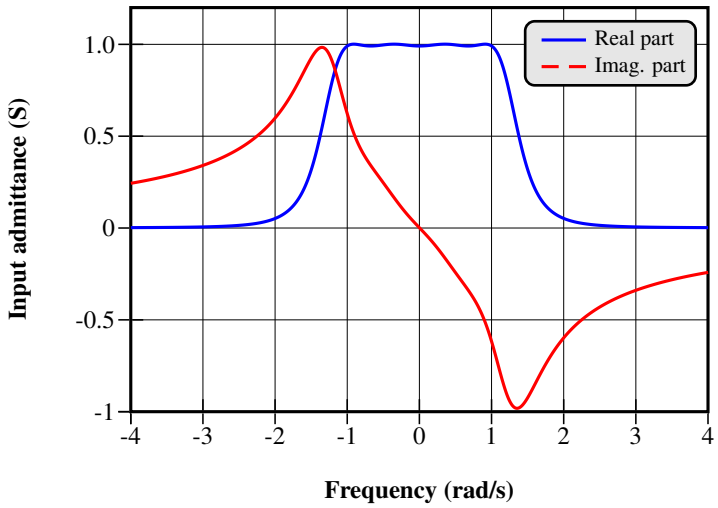

Figure 4.1 Response of the input impedance of the singly terminated network.

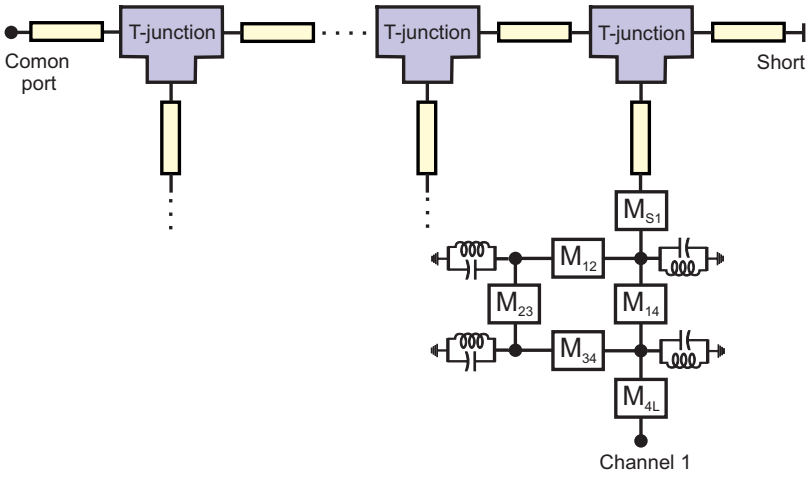

Figure 4.2 Multiplexer structure with the lumped model of the filters.

the manifold through E-plane junctions, and $m\lambda_g/4$ for multiplexers with H-plane junctions. Junction-filter stub lengths are also initialized at $m\lambda_g/2$.

Even though the filters have an ideal response when they are isolated, once they are put together with the manifold to form the multiplexer, the channel responses are not ideal any more. This is due to the interactions between the different filters and the manifold that occurs in both contiguous and non-contiguous cases. To achieve the required response of the multiplexer, an optimization of the model needs to be performed. The optimization masks must be specified according to the design spec-

ifications of the multiplexer, and may include restrictions to the common port return loss (CPRL) and the transmission characteristics of the different channels. As an example, the typical specifications of a C-band output multiplexer of a real satellite system can be found in section 1.8.4 of [2]. The steps to carry out an efficient optimization are detailed below:

1. Optimize the lengths of the transmission lines placed between the T-junctions, and between the short-circuit and the last T-junction.

2. Optimize the length of the transmission lines between the T-junctions and the filters.

3. Optimize all the transmission lines together (between T-junctions, and between T-junctions and filters).

4. Optimize the first 3 or 4 parameters of each filter (the ones which are closer to the manifold). An option would be to include the input coupling, the coupling between the two orthogonal modes inside the first cavity, and the resonant frequency of the two modes in the first cavity. In this step, the stub length connecting the filter to the manifold is also included. This is done with each filter separately, starting always with the filter placed next to the short-circuit, except if there is another filter whose response is clearly worse than the others, in which case this filter is optimized first.

Repeat the previous steps until the multiplexer response is almost perfect. This time, when optimizing the filters, more parameters may be included, specially when dealing with contiguous multiplexers. After the second round, the length of the lines (manifold and stubs) change very little, so the corresponding steps can be avoided. Normally, no more than three optimization rounds are needed. Besides, the optimization process will be very fast, since it is being applied over the circuit model. If the number of channels is not very large, in order to refine the response, a final optimization with all the parameters can be carried out.

Once the optimization is finished, the response of the multiplexer circuit with the lumped model of the filters will meet the specifications, but the response of the individual filters will not be ideal any more, because each filter has been modified to compensate its interaction with the rest of the structure. Additionally, the optimized filters, whatever they have been initially designed as contiguous or non-contiguous, will now be asymmetric and asynchronous, which means that the resonant frequency will be different in all the cavities within each filter.

4.3 Synthesis of the Distributed Model

The next step is to replace the previously optimized lumped model of the filters with their distributed counterparts. As it was explained in section 2.3, this is done by replacing the LC resonators with equivalent transmission lines resonating at the corresponding frequency, and calculating the values of the new inverters following (2.18).

The structure of the multiplexer with the distributed model of the filters is shown in Figure 4.3.

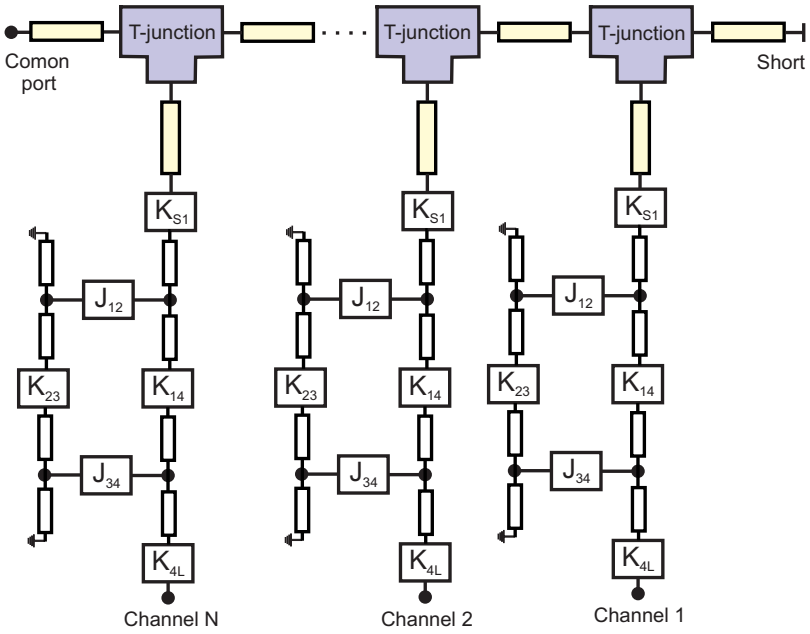

Figure 4.3 Structure of the multiplexer with the distributed model for each filter.

In section 2.3, in the last step of the circuit simplification, it was said that when designing individual filters, the two unity coupling K-inverters (see Figure 2.11) could be removed, since they only affect the phase of the filter, and not its modulus. However, when a multiplexer design is being carried out, the phase of each part of the circuit matters, and when substituting the lumped model of each filter by its distributed model, both circuits must be completely equivalent, not only in modulus, but also in phase. Therefore, the unity coupling inverters can not be ignored and must be taken into account.

One possibility could be to include the unity inverters in both sides of each filter in the distributed model. The problem here is that these inverters should be later converted to a physical part of the multiplexer, and this is not trivial. Since the only condition is that the lumped and the distributed models must be equivalent, an easier option would be to include these unity inverters in the lumped model, prior to the optimization process. That way, when substituting the lumped model of each filter (with the unity inverters), by the the corresponding distributed model (without unity inverters), both circuits are equivalent in modulus and in phase.

When designing E-plane contiguous channel multiplexers, since the equivalent network of the T-junction acts as a series connector, the multiplexer is obtained as an addition of the input impedances of the channel filters. In this case, the unity inverters will transform admittances into impedances, so the impedance of the lumped model

Case	Filter networks	Lumped model	Distributed model
Non-contiguous E-plane	Doubly term.	Inverters $K = 1$	-
Non-contiguous H-plane	Doubly term.	Inverters $K = 1$	-
Contiguous E-plane	Singly term.	Inverters $K = 1$	-
Contiguous H-plane	Singly term.	-	Stub $\lambda_g/4$

Table 4.1 The four possible cases in the design of multiplexers, depending if it is or not contiguous, and if it is E-plane or H-plane.

plus the two inverters will have the desired shape shown in Figure 4.1. However, if an H-plane contiguous multiplexer is considered, the equivalent networks of the T-junctions will act as parallel connections, carrying out an addition of the input admittances. Since the admittance of lumped model of the filters already has the proper shape (see Figure 4.1), no inverters should be included, in order to achieve a better starting point in the optimization. Instead, a transmission line of $\lambda_g/4$ is added to the input port of the filters in the distributed model, which in fact acts as an inverter (at the center frequency of the filter).

In non-contiguous multiplexers, thanks to the big separation between channels, the fact of adding admittances or impedances is not so important, and the previous consideration can be neglected, thus opting for the easier option in both E-plane and H-plane multiplexers. For the sake of clarity, the different cases have been summarized in Table 4.1.

The length of the transmission lines modeling the cavities can be calculated following (2.4). In this case, it must be taken into account that each transmission line will have a different length, since all the resonant frequencies are different.

The value of the cavity radius is needed in order to calculate the elements of the distributed model, so it must be decided at this point. A proper choice of the radius value is crucial, not only to achieve a good design of the individual channel filters, but also to avoid undesired resonances inside the bandwidth of the whole multiplexer. The radius may or may not be the same for all the channel filters of the multiplexer. When choosing the radius of each filter, it must be guaranteed that the only resonance in the whole multiplexer bandwidth is the desired resonant mode.

After substituting the lumped model of the filters by their distributed models, if the channel fractional bandwidths are small (e.g. less than 1 %), the response of the new distributed model of the multiplexer will be practically the same as the response of the lumped model, so no further optimization will be required. If wider bandwidths are considered, a soft general optimization may be necessary.

4.4 Extraction of the Physical Dimensions

As it was done for the design of CWDM filters, the distributed model of the whole multiplexer is going to be employed to calculate its physical dimensions. First of all,

the dimensions of all the channel filters are going to be obtained. Then, the initial lengths of the waveguide sections in the manifold, and between the manifold and the filters, will be calculated. Finally, a step by step optimization will be carried out to refine the final response of the multiplexer.

4.4.1 Individual Filters

The first step is to calculate the dimensions of all the channel filters within the multiplexer. This is done filter by filter, and the values of the distributed model obtained in section 4.3 are going to be used. The design procedure for each filter is very similar to the one explained in section 2.4, with some modifications.

First, the sizes of all the irises are calculated to achieve the corresponding inverter values given by the distributed model, using the iterative method detailed in 2.4.1.

Next, the length of the cavities and the penetrations of the three screws inside each cavity must be obtained. As it was explained in section 2.4.2, the design is accomplished by matching the response of the EM model of each cavity with the response of the equivalent distributed model. However, in this case the technique presented in section 2.4.2 needs to be modified, so it can be applied to filters whose response is not ideal. A typical response of one stage of a channel CWDM filter is shown in Figure 4.4. Note that, unlike for ideal CWDM filters, this response is not totally symmetric. In this case, the dimensions of the cavities and the screws will be adjusted to match the asymmetric response of each filter stage of the distributed model. Once all the individual filters have been designed, they will not have an ideal response, since their dimensions have been adjusted to compensate the influence of the rest of the structure.

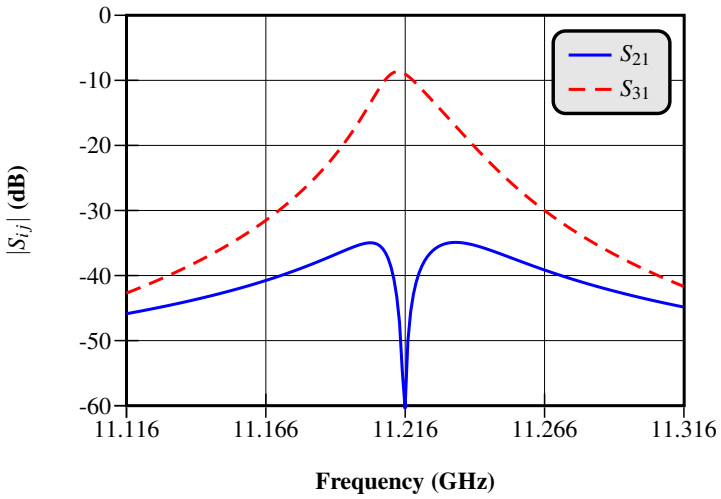

Figure 4.4 Response of one stage of the distributed model of a channel filter with asymmetric lobes.

4.4.2 Manifold Waveguide Sections and Stubs

The spacings between T-junctions, and between the last T-junction and the short circuit, are the same as the ones obtained with the distributed model. The spacings between junctions and filters, on the other hand, must be changed to take into account the influence of the input iris of each filter. The loading effect introduced by the iris in the input-waveguide side, must be compensated by adding its corresponding phase shift to the length of the stub obtained in the distributed model:

$$l^{(EM)} = l^{(dis)} + \frac{\phi_{iris}}{2\beta} \tag{4.1}$$

where ϕ_{iris} can be obtained using (2.19). Since the value of ϕ_{iris} is always negative, the resulting lines in the EM model will be shorter than the corresponding ones in the distributed model.

4.4.3 Complete Multiplexer

Once all the dimensions of the filters and the waveguide sections have been computed, they can be assembled together to build an initial EM model of the multiplexer, which will already give a response very close to the desired one. Nevertheless, a slight final optimization may be carried out, in order to refine the response. This optimization is also made step by step, following the procedure explained in section 4.2.2.

4.5 Design Examples

4.5.1 Non-Contiguous Channel Multiplexer

In this section, a non-contiguous 10-channel multiplexer with CWDM filters is going to be designed. In this case, an E-plane configuration has been chosen. The frequency plan of the multiplexer, belonging to the Ku frequency band, is detailed in Table 4.2, while the rest of the specifications are the following ones:

- Order of the channel filters: $N = 4$
- Return loss: $RL = 22$ dB
- Stopband rejection: > 40 dB
- Resonant mode inside the cavities: TE_{113}

4.5.1.1 Lumped Model of the Individual Filters The first step is to design the lumped model of the channel filters as if they were not connected to the multiplexer. Since the coupling matrix does not depend on the center frequency, it will be the same for all the filters:

Channel	Center frequency (GHz)	Bandwidth (MHz)
1	11.000	36
2	11.054	36
3	11.108	36
4	11.162	36
5	11.216	36
6	11.270	36
7	11.324	36
8	11.378	36
9	11.432	36
10	11.486	36

Table 4.2 Frequency plan of the non-contiguous 10-channel multiplexer.

$$M = \begin{pmatrix} 0 & 1.0741 & 0 & 0 & 0 & 0 \\ 1.0741 & 0 & 0.9356 & 0 & -0.1079 & 0 \\ 0 & 0.9356 & 0 & 0.7670 & 0 & 0 \\ 0 & 0 & 0.7670 & 0 & 0.9356 & 0 \\ 0 & -0.1079 & 0 & 0.9356 & 0 & 1.0741 \\ 0 & 0 & 0 & 0 & 1.0741 & 0 \end{pmatrix}$$

The initial response of the lumped model of all the individual filters has been depicted in Figure 4.5.

4.5.1.2 Multiplexer with the Lumped Model of the Filters An initial circuit is created by connecting the previous lumped model of all the filters to the manifold. The manifold waveguides, and the stubs connecting the filters with the manifold, are modeled with equivalent π-networks. The length of the stubs between the manifold and the filters are initialized at $\lambda_g/2$ to achieve a compact design. The waveguide sections connecting the T-junctions, on the other hand, are in this case initialized to λ_g, in order to leave the required separation between adjacent channel filters. At this point, the multiplexer provides the response shown in Figure 4.6.

As it can be seen, even though the response of the individual filters was perfect (see Figure 4.5), when they are connected to the manifold, the multiplexer response is seriously deteriorated. This is because the lumped model of the filters does not take into account the effect of the rest of the structure. Furthermore, the initial length values of the transmission lines in the manifold is just a starting point, but they also need to be adjusted.

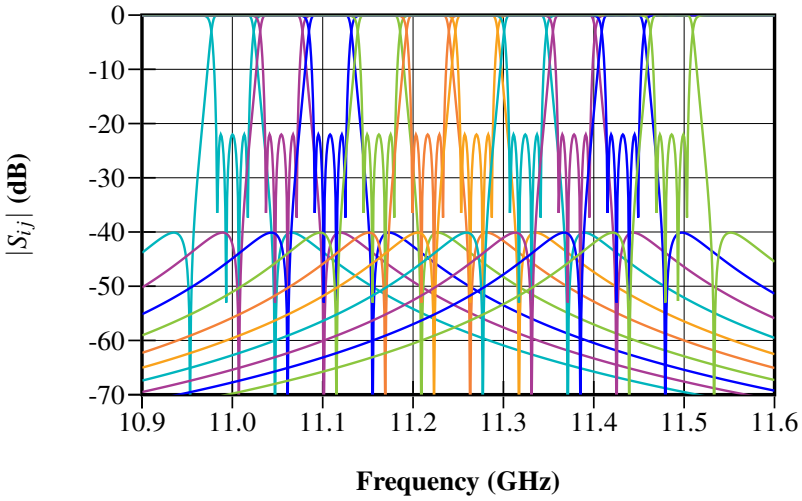

Figure 4.5 Initial response of the lumped model of the individual filters of the non-contiguous 10-channel multiplexer.

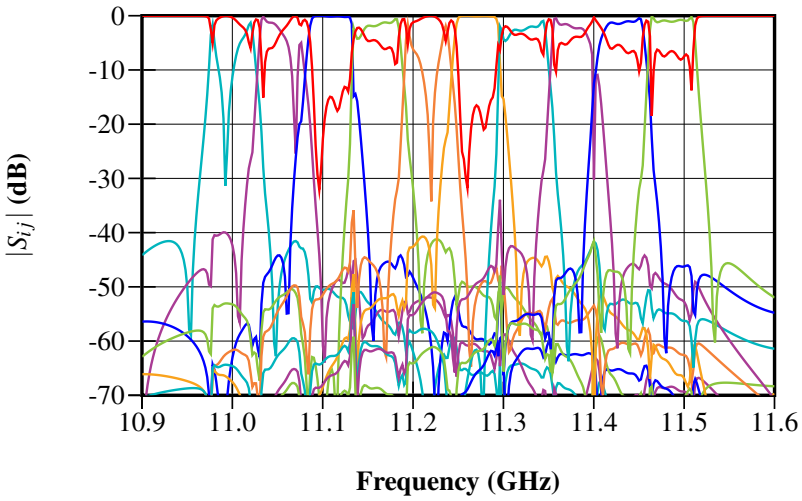

Figure 4.6 Initial response of the non-contiguous 10-channel multiplexer with the lumped model of the filters.

Therefore, a step-by-step optimization is performed following the procedure explained in section 4.2.2. The response of the multiplexer after the optimization is shown in Figure 4.7, where it can be appreciated that it meets the design specifications.

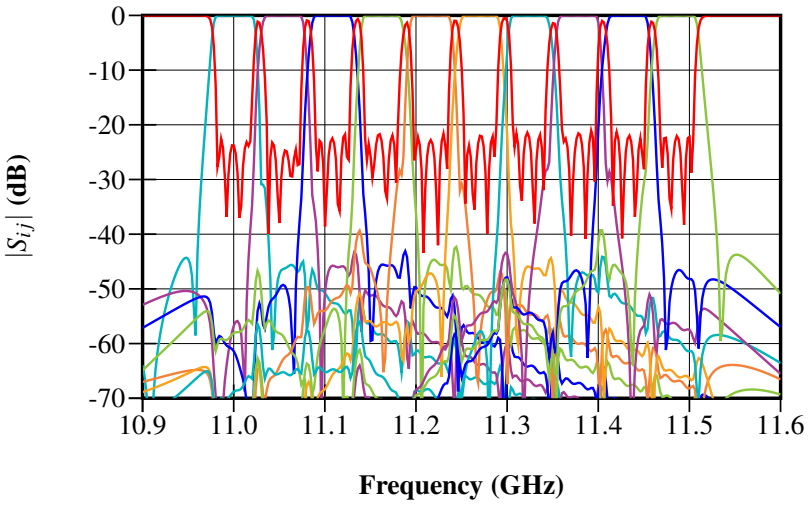

Figure 4.7 Response of the non-contiguous 10-channel multiplexer with the lumped model of the filters after the optimization process.

4.5.1.3 Multiplexer with the Distributed Model of the Filters Starting from the lumped model of each filter of the previously optimized multiplexer, the corresponding distributed models can be obtained as it was explained in section 4.3. The response of the multiplexer with the distributed model of the filters is shown in Figure 4.8, compared with the response of the multiplexer with the lumped models. In order to make the comparison clearer, only one parameter has been represented, which corresponds to the CPRL.

As it can be seen in Figure 4.8, both responses are almost identical, so no further optimization is needed. Nevertheless, the distributed model constitutes a more accurate representation of the physical structure of the multiplexer than the lumped model, so it will be more useful in order to extract the physical dimensions of the multiplexer.

4.5.1.4 Physical Dimensions of the Channel Filters First of all, the physical dimensions of each channel filter are calculated individually, following the procedure explained in section 4.4. Each filter is designed using the distributed model of the corresponding filter obtained in section 4.5.1.3. Remember that these filters are not ideal (the response is neither perfect nor symmetrical), but they are the required filters to achieve the desired multiplexer. The responses of the distributed model of the 10 individual filters are shown in Figure 4.9.

After applying the design technique of section 4.4 to design each filter, the response of the EM model of the individual filters will be very similar to the responses shown in Figure 4.9.

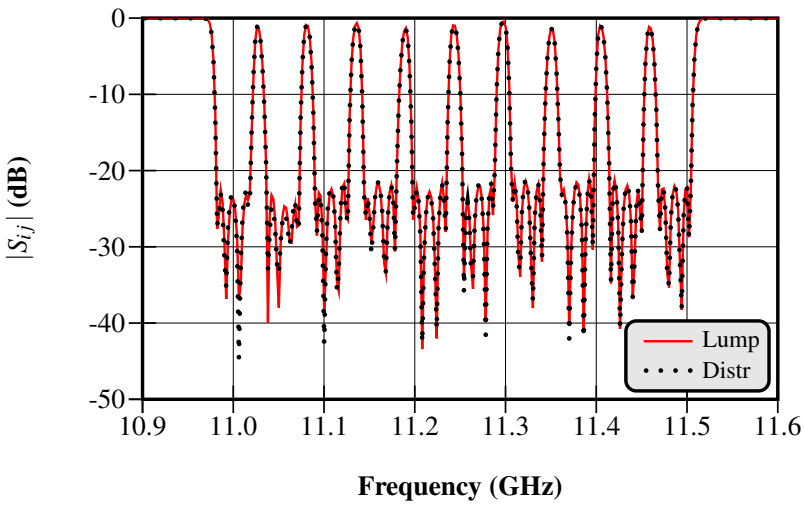

Figure 4.8 Comparison between the CPRL of both lumped and distributed models of the non-contiguous 10-channel multiplexer.

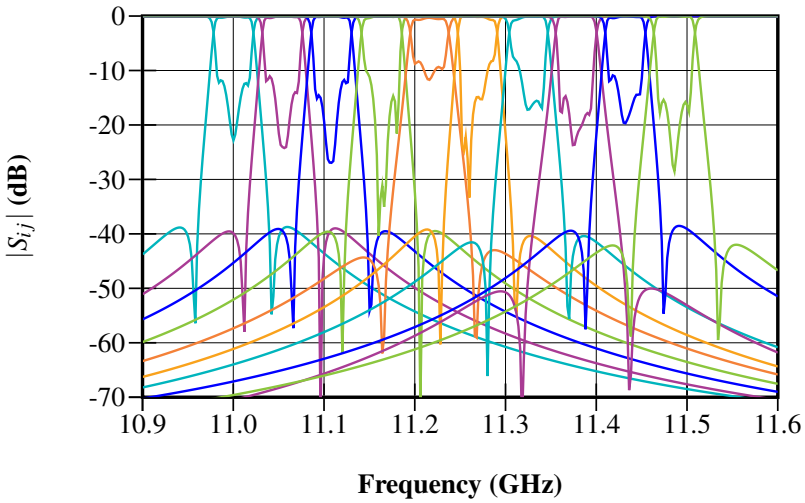

Figure 4.9 Responses of the individual filters in the distributed model of the non-contiguous 10-channel multiplexer.

4.5.1.5 Physical Dimensions of the Multiplexer The previously designed channel filters are connected to the manifold through the waveguide stubs to form the initial EM model of the multiplexer. The length of the manifold waveguides and the stubs are calculated as it was explained in section 4.4.2. The response of the EM model of the multiplexer after assembling all the pieces together is shown in Fig-

ure 4.10. The physical structure of the multiplexer is shown in Figure 4.11, where the structure of a CWDM channel filter has also been depicted.

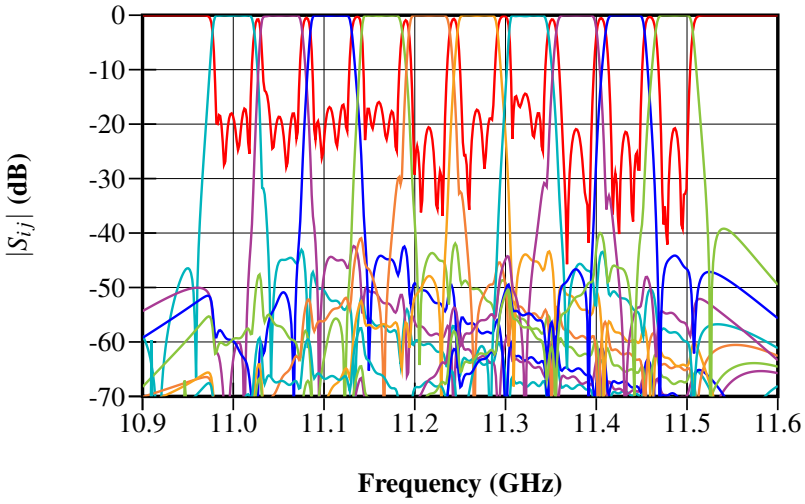

Figure 4.10 Initial response of the EM model of the non-contiguous 10-channel multiplexer.

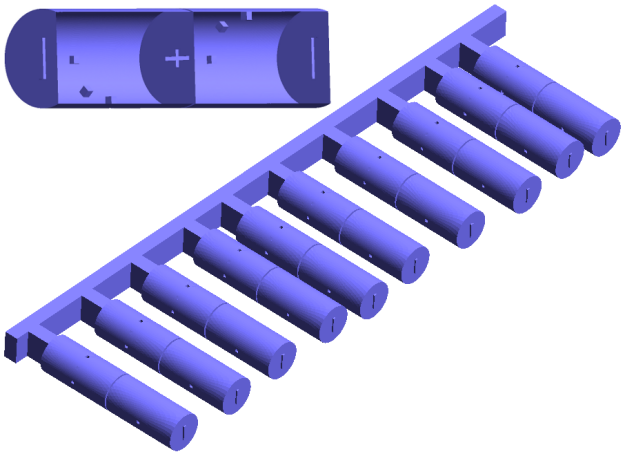

Figure 4.11 Physical structure of the non-contiguous 10-channel multiplexer with CWDM filters.

As it can be seen in Figure 4.10, the initial response of the EM model of the multiplexer is quite close to the desired one. Nevertheless, an optimization can be carried out in order to refine the previous response. The optimization process will be faster if it is made step by step, following a procedure like the one performed to optimize the lumped model (see section 4.2.2). Although the optimization is made

over an EM model, it should not take a long time, since the starting point is already very good.

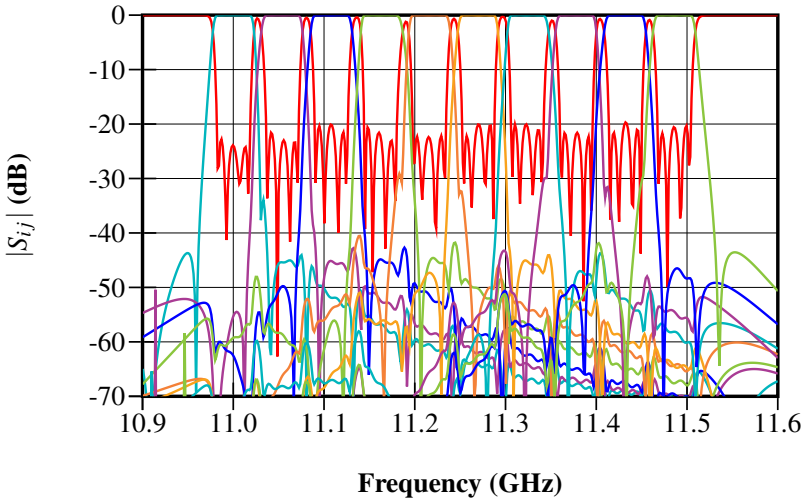

Figure 4.12 Optimized response of the EM model of the non-contiguous 10-channel multiplexer.

The final physical dimensions of the optimized multiplexer are detailed in Tables 4.3 and 4.4. Table 4.3 contains the dimensions of the manifold sections (between T-junctions, and between the last T-junction and the short circuit) and the stubs connecting the channel filters with the manifold, where N refers to the channel filter closest to the common port (see Figure 4.13). The WR-75 standard waveguide (a = 19.05 mm, b = 9.525 mm) has been employed for the manifold and the stubs (with a rotation of 90^{o} to allow an E-plane connection).

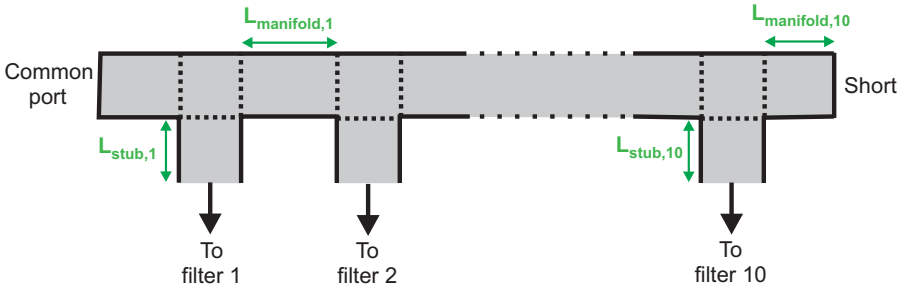

Figure 4.13 Physical dimensions of the manifold sections and the stubs for the non-contiguous 10-channel multiplexer.

On the other hand, Table 4.4 includes all the inner dimensions of the 10 channel filters. The thickness of all the irises is 1 mm. The width (smallest dimension in the

N	L_{stub}	$L_{manifold}$
1	16.622	38.169
2	16.927	34.664
3	14.793	37.533
4	14.257	24.340
5	17.867	32.666
6	13.391	38.941
7	15.634	38.935
8	18.376	32.979
9	14.869	21.548
10	17.235	32.007

Table 4.3 Final dimensions (mm) of the manifold sections and the stubs in the non-contiguous 10-channel multiplexer.

cross section) of the input and output irises is 2 mm, while in the cross iris is 1 mm. All the iris dimensions in the table refer to the biggest dimension in the cross section ($Cross_H$ and $Cross_V$ are the horizontal and vertical arms of the cross iris). The cavity metal insertions have a square cross section of 2 mm side length, and T_V, T_H and T_O, are the penetrations of the vertical, horizontal and oblique screws, respectively. Note that, in this case, different cavity radius values have been chosen for the different channel filters, in order to achieve a greater spurious-free margin.

	Cavity	Cavity 1				Cavity 2				Irises			
	radius	L	T_V	T_H	T_O	L	T_V	T_H	T_O	Input	Output	$Cross_H$	$Cross_V$
Filter 1	12.550	52.212	1.530	2.925	2.018	52.169	1.505	2.953	2.223	10.336	10.405	4.526	7.857
Filter 2	12.550	51.834	1.500	2.845	1.996	51.750	1.500	2.937	2.206	10.107	10.347	4.491	7.823
Filter 3	12.600	51.297	1.500	2.799	2.004	51.201	1.500	2.918	2.219	10.077	10.287	4.479	7.782
Filter 4	12.650	50.874	1.378	2.771	2.006	50.794	1.470	2.889	2.202	10.028	10.231	4.426	7.746
Filter 5	12.650	50.121	1.453	3.067	2.145	50.284	1.468	2.867	2.207	10.534	10.171	3.968	7.636
Filter 6	12.700	50.077	1.517	2.603	1.933	49.887	1.537	2.864	2.213	9.655	10.116	4.403	7.582
Filter 7	12.750	49.404	1.461	2.814	2.043	49.398	1.492	2.814	2.205	10.000	10.058	4.167	7.590
Filter 8	12.750	48.922	1.484	2.790	2.124	48.914	1.513	2.783	2.235	9.988	10.002	3.594	7.500
Filter 9	12.750	48.572	1.411	2.731	2.064	48.544	1.519	2.747	2.249	9.948	9.949	4.243	7.588
Filter 10	12.800	48.058	1.078	2.713	2.096	48.080	1.494	2.671	2.263	10.173	9.893	3.965	7.628

Table 4.4 Final dimensions (mm) of the channel filters for the non-contiguous 10-channel multiplexer.

4.5.2 Contiguous Channel Multiplexer

Unlike a non-contiguous channel multiplexer, in a contiguous channel multiplexer the separation between channels is quite small. This entails a big interaction between each channel with its neighbors. In this section, a contiguous 8-channel multiplexer in E-plane configuration will be designed. It will operate in Ku-band, and its frequency plan is detailed in Table 4.5. The distance between the end of the band of one channel until the beginning of the band of the next channel (called guard band) is only 4 MHz, which represents a 10% of the separation between the center frequencies of two adjacent channels (40 MHz). Therefore, the multiplexer channels are clearly contiguous.

Channel	Center frequency (GHz)	Bandwidth (MHz)
1	11.000	36
2	11.040	36
3	11.080	36
4	11.120	36
5	11.160	36
6	11.200	36
7	11.240	36
8	11.280	36

Table 4.5 Frequency plan of the 8-channel contiguous multiplexer.

The rest of the specifications are the following:

- Order of the channel filters: $N = 4$
- Return loss: $RL = 22$ dB
- Stopband rejection: > 40 dB
- Resonant mode inside the cavities: TE_{113}

4.5.2.1 Lumped Model of the Individual Filters First of all, the lumped model of the 8 filters must be synthesized. Since a contiguous multiplexer is being designed, the coupling matrix of the channel filters will be synthesized as singly terminated:

$$M = \begin{pmatrix} 0 & 0.9167 & 0 & 0 & 0 & 0 \\ 0.9167 & 0 & 0.7697 & 0 & -0.1773 & 0 \\ 0 & 0.7697 & 0 & 0.9333 & 0 & 0 \\ 0 & 0 & 0.9333 & 0 & 1.4789 & 0 \\ 0 & -0.1773 & 0 & 1.4789 & 0 & 1.5191 \\ 0 & 0 & 0 & 0 & 1.5191 & 0 \end{pmatrix}$$

It can be appreciated that the coupling matrix is clearly asymmetric (with respect to its anti-diagonal), and also the couplings near the output are much bigger than those near the input. This is indeed a typical characteristic of the singly terminated coupling matrices.

The initial response of the lumped model of all the individual filters is shown in Figure 4.14. The contiguity between channel filters can clearly be appreciated.

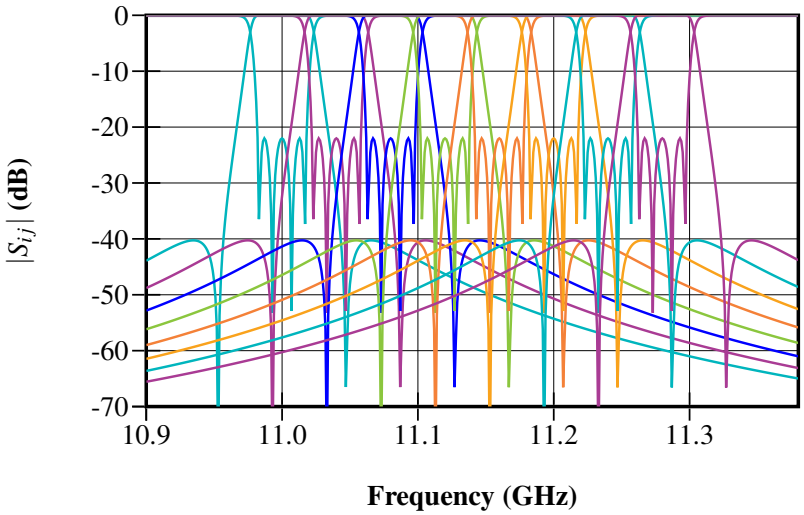

Figure 4.14 Initial response of the lumped model of all the individual filters of the contiguous 8-channel multiplexer.

4.5.2.2 Multiplexer with the Lumped Model of the Filters The previously synthesized lumped models of the 8 channel filters are connected to the manifold. In this case, an herringbone configuration has been chosen, with the channel filters placed in both sides of the manifold. This configuration allows to make the multiplexer shorter, since the minimum length of the manifold sections necessary to avoid the physical overlapping between filters can be smaller. On the other hand, the width of the multiplexer is doubled. Note that, as long as the length of the manifold sections do not change, the response (in modulus) of the multiplexer is the same regardless of

whether the filters are placed in one or both sides of the manifold. Nevertheless, the configuration must be decided prior to the optimization of the lumped model of the multiplexer, since suitable constraints must be specified according to the minimum separation between filters.

Therefore, as it was done in the previous example, the length of the stubs connecting the channel filters with the manifold are initialized at $\lambda_g/2$. However, in this case, the waveguide sections between the T-junctions can also be initialized at $\lambda_g/2$, since this value already provides enough separation between the filters. The response of the resulting initial multiplexer can be seen in Figure 4.15.

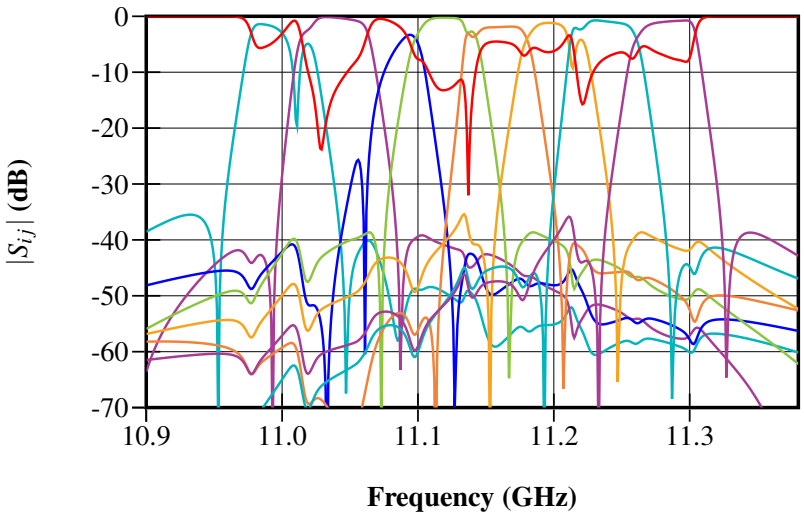

Figure 4.15 Initial response of the contiguous 8-channel multiplexer with the lumped model of the filters.

Next, an optimization must be carried out over the previous multiplexer model to achieve the desired response. The optimization procedure is the same as for non-contiguous multiplexers, and it was explained in section 4.2.2. The response obtained after the optimization is shown in Figure 4.16.

4.5.2.3 Multiplexer with the Distributed Model of the Filters The lumped model of each filter of the optimized circuit is replaced by the corresponding distributed model, following the process explained in section 4.3. The response of the resulting circuit, in comparison with the lumped model, can be seen in Figure 4.17, where it can be appreciated that both responses are practically identical.

4.5.2.4 Physical Dimensions of the Channel Filters The first step is to calculate the initial dimension of each channel filter employing the distributed model. The responses of the distributed model of the 8 individual channel filters are shown in Figure 4.18. The physical dimensions of the channel filters will be calculated as explained in section 4.4, in order to match the filter responses in Figure 4.18.

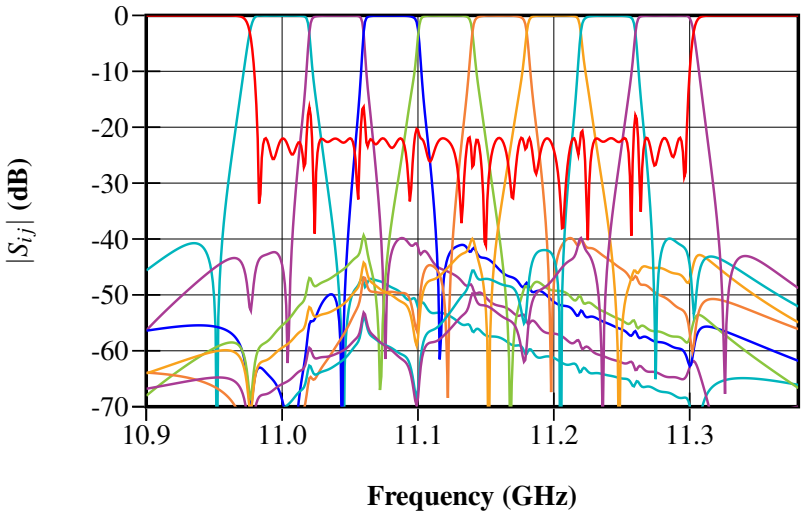

Figure 4.16 Response of the contiguous 8-channel multiplexer with the lumped model of the filters, after the optimization process.

4.5.2.5 Physical Dimensions of the Multiplexer The initial multiplexer is obtained by connecting the previously designed channel filters to a manifold with the waveguide lengths calculated as explained in section 4.4.2. The multiplexer structure is shown in Figure 4.19, while its initial response can be seen in Figure 4.20.

The initial response of the multiplexer must be improved in order to meet the design specifications. As it was done for the contiguous case, a step-by-step optimization must be carried out, which will not take long since the initial response is not far from the desired one. The response obtained after the optimization is shown in Figure 4.21.

The final dimensions of the manifold waveguide sections and the stubs between the manifold and the channel filters are detailed in Table 4.6. The waveguide employed is the same as for the non-contiguous example (the standard waveguide WR-75).

The physical dimensions of the 8 channel filters can be found in Table 4.7. The rest of the dimensions of the irises and the screws that are not specified in such table have the same values as those for the non-contiguous example.

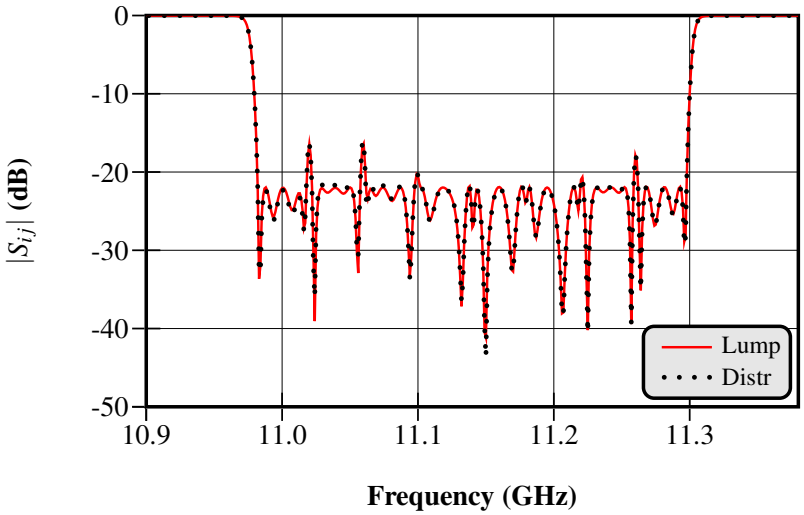

Figure 4.17 Comparison between the CPRL of both lumped and distributed models of the contiguous 8-channel multiplexer.

N	L_{stub}	$L_{manifold}$
1	17.358	14.653
2	15.276	18.623
3	18.673	23.913
4	17.166	16.897
5	16.810	23.693
6	17.480	15.390
7	15.601	20.622
8	19.710	14.872

Table 4.6 Final dimensions (mm) of the manifold sections and the stubs for the contiguous 8-channel multiplexer (N=1 corresponds to the filter channel closest to the common port, as in Figure 4.13).

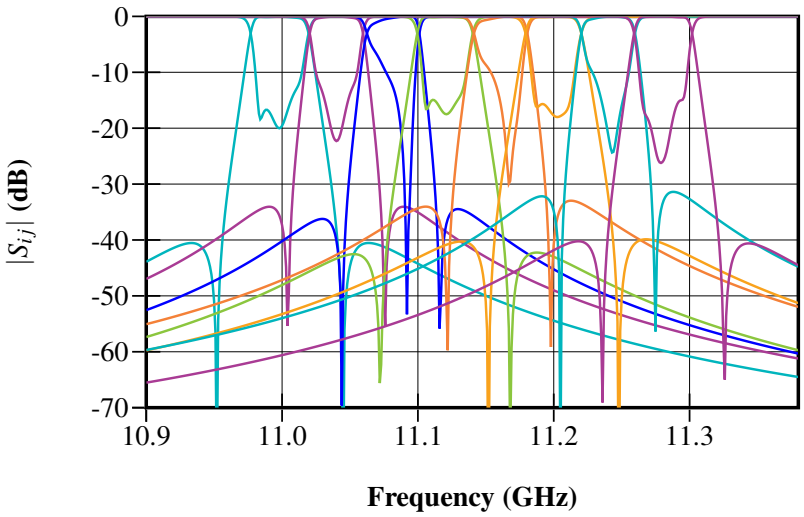

Figure 4.18 Responses of the individual filters in the distributed model of the contiguous 8-channel multiplexer.

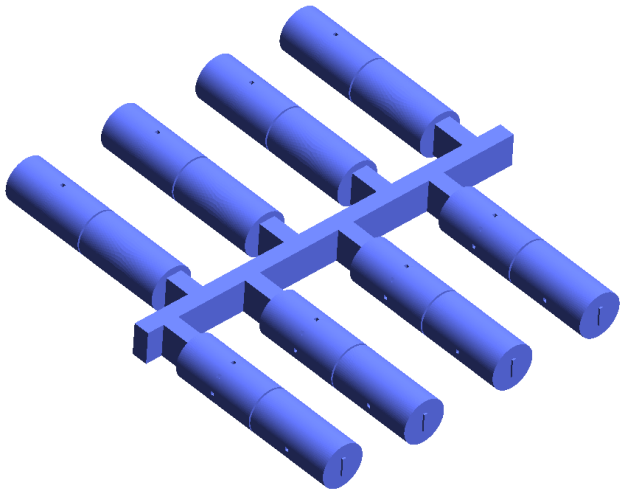

Figure 4.19 Physical structure of the contiguous 8-channel multiplexer with herringbone configuration.

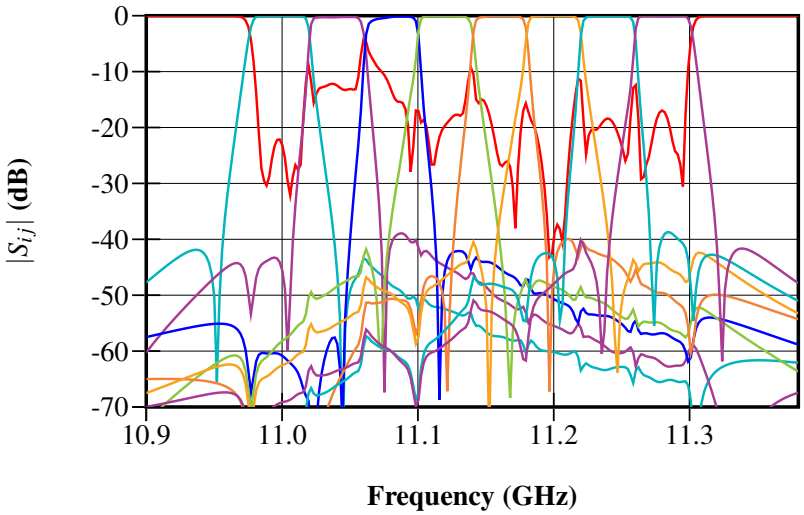

Figure 4.20 Initial response of the EM model of the contiguous 8-channel multiplexer.

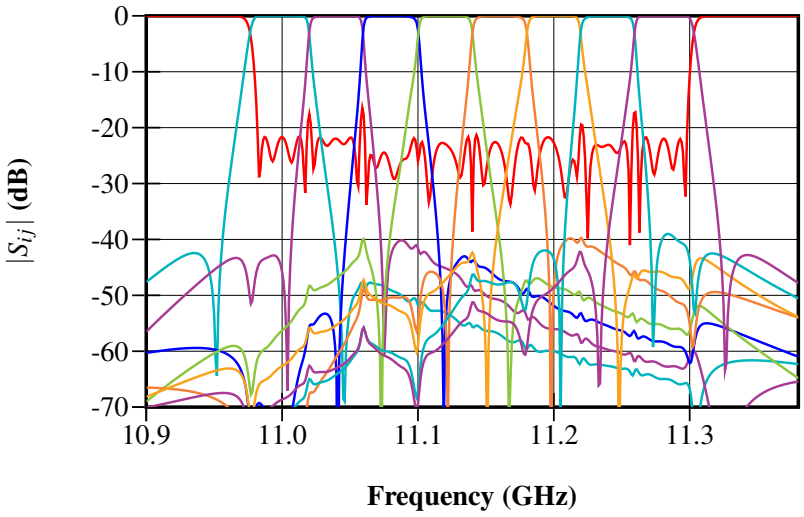

Figure 4.21 Optimized response of the EM model of the contiguous 8-channel multiplexer.

	Cavity	Cavity 1				Cavity 2				Irises			
	radius	L	T_V	T_H	T_O	L	T_V	T_H	T_O	Input	Output	$Cross_H$	$Cross_V$
Filter 1	12.700	51.793	1.488	2.955	2.098	51.709	1.507	3.030	2.334	10.431	10.560	4.289	7.801
Filter 2	12.700	51.666	1.498	2.651	1.848	51.320	1.510	3.095	2.423	9.713	10.667	4.921	7.814
Filter 3	12.750	51.185	1.514	2.719	1.898	50.947	1.494	3.020	2.359	9.682	10.531	4.579	7.749
Filter 4	12.750	50.794	1.393	2.845	2.011	50.612	1.501	3.042	2.374	10.236	10.558	4.172	7.668
Filter 5	12.800	50.471	1.465	2.680	1.876	50.075	1.399	3.121	2.555	9.682	10.768	4.971	7.837
Filter 6	12.800	50.082	1.480	2.827	2.034	49.810	1.515	3.084	2.537	10.109	10.677	4.232	7.673
Filter 7	12.850	49.771	1.484	2.682	1.897	49.494	1.529	2.982	2.434	9.706	10.451	4.985	7.696
Filter 8	12.850	49.425	1.387	2.732	2.081	49.301	1.500	2.870	2.330	9.983	10.238	4.215	7.621

Table 4.7 Final dimensions (mm) of the channel filters for the contiguous 8-channel multiplexer.

REFERENCES

1. M. Brumos, S. Cogollos, M. Martinez, P. Soto, V.E. Boria, and M. Guglielmi. Design of waveguide manifold multiplexers with dual-mode filters using distributed models. In *Microwave Symposium (IMS), 2014 IEEE MTT-S International*, pages 1–4, June 2014.
2. R.J. Cameron, C.M. Kudsia, and R.R. Mansour. *Microwave Filters for Communication Systems: Fundamentals, Design and Applications*. Wiley, 2007.
3. C. Kudsia, R. Cameron, and Wai-Cheung Tang. Innovations in microwave filters and multiplexing networks for communications satellite systems. In *Microwave Theory and Techniques, IEEE Transactions on*, volume 40, pages 1133–1149, 1992.
4. G. Macchiarella. Synthesis of star-junction multiplexers. In *Microwave Magazine, IEEE*, volume 12, pages 101–109, Oct 2011.
5. C.M. Kudsia, J. Dorey, J. Heierli, K. R. Ainsworth, and G. J P Lo. A new type of low loss l4 GHz high power combining network for satellite earth terminals. In *Microwave Conference, 1979. 9th European*, pages 386–391, Sept 1979.
6. R.J. Cameron and M. Yu. Design of manifold-coupled multiplexers. In *Microwave Magazine, IEEE*, volume 8, pages 46–59, 2007.
7. A.E. Atia. Computer-aided design of waveguide multiplexer (short papers). In *Microwave Theory and Techniques, IEEE Transactions on*, volume 22, pages 332–336, 1974.
8. C. Kudsia, K. Ainsworth, and M. O'Donovan. Microwave filters and multiplexing networks for communication satellites in the 1980s. In *Proc. AIAA 8th Communications Satellite Systems Conf.*, Apr 1980.

9. J.D. Rhodes and R. Levy. Design of general manifold multiplexers. In *Microwave Theory and Techniques, IEEE Transactions on*, volume 27, pages 111–123, Feb 1979.

10. A.E. Atia and A.E. Williams. Narrow-bandpass waveguide filters. In *Microwave Theory and Techniques, IEEE Transactions on*, volume 20, pages 258–265, Apr 1972.

11. L. Accatino and M. Mongiardo. Hybrid circuit-full-wave computer-aided design of a manifold multiplexers without tuning elements. In *Microwave Theory and Techniques, IEEE Transactions on*, volume 50, pages 2044–2047, 2002.

12. Y. Wang, S. Li, and M. Yu. Hybrid models for effective design and optimization of large-scale multiplexing networks. In *Microwave Theory and Techniques, IEEE Transactions on*, volume 61, pages 1839–1849, 2013.

13. D. Bariant, S. Bila, D. Baillargeat, S. Verdeyme, P. Guillon, D. Pacaud, and J.-J. Herren. Method of spurious mode compensation applied to manifold multiplexer design. In *Microwave Symposium Digest, 2002 IEEE MTT-S International*, volume 3, pages 1461–1464 vol.3, June 2002.

14. M.A. Ismail, D. Smith, A. Panariello, Y. Wang, and M. Yu. EM-based design of large-scale dielectric-resonator filters and multiplexers by space mapping. In *Microwave Theory and Techniques, IEEE Transactions on*, volume 52, pages 386–392, 2004.

15. M. Yu and Y. Wang. Synthesis and beyond. In *Microwave Magazine, IEEE*, volume 12, pages 62–76, Oct 2011.

16. M.A. Ismail, Y. Wang, and M. Yu. Advanced design and optimization of large scale microwave devices. In *Microwave Symposium Digest (MTT), 2012 IEEE MTT-S International*, pages 1–3, June 2012.

CHAPTER 5

DESIGN OF A WIDEBAND MANIFOLD MULTIPLEXER WITH RECTANGULAR WAVEGUIDE FILTERS

This chapter addresses the design of a wideband manifold multiplexer with six channel filters. The design of wideband multiplexers is specially complicated, since a lot of spurious may appear inside the multiplexer bandwidth. The way to minimize these spurious is to maintain the manifold lengths as short as possible. In the following sections, the complete design procedure of a wideband multiplexer with a new type of rectangular-waveguide filter is going to be thoroughly explained. The multiplexer was designed as part of a test bed to measure passive intermodulation (PIM) effects at K-band, for being employed in the European High Power RF Space Laboratory [1]. Some preliminary tests were performed, prior to fabrication, in order to guarantee its proper functioning. The manufactured prototype was measured and tested, and the excellent obtained results fully validate the design procedure.

Design of microwave filters and multiplexers in waveguide technology using distributed models.
By María Brumos Vicente, Universidad Politécnica de Valencia.

5.1 Background

The design of narrowband multiplexers, which are the most commonly used in satellite communications, has been traditionally carried out by means of equivalent circuits with lumped elements [2, 3]. In the last years, more advanced design techniques have also been proposed in order to design these complex devices in a more efficient way [4–10].

More recently, some works related with the design of multiplexers with moderate bandwidths have been developed, in which complex models for the channel filters were employed, together with simple models for the manifold [11]. Nevertheless, the wideband case has only been considered for filters, but not for entire multiplexers, where an increase in the bandwidth entails a much more complex design, mainly due to spurious caused by the manifold. In [12], a modified structure for the channel filters has been proposed, which is able to compensate spurious occurring in the manifold, but it also entails an increase of the filter size.

In the previous chapter, a new design procedure employing a distributed model of the whole multiplexer was presented. Now, the same concept is going to be applied to design a wideband multiplexer. In order to minimize the spurious modes, very short waveguide sections are going to be considered for the manifold, and the procedure is going to be suitably modified to take into account the high-order EM modes of the structure.

5.2 General Description

In the following sections, the design of an E-plane non-contiguous 6-channel multiplexer in K-band is going to be considered. The multiplexer is intended to be part of a test bed to measure PIM effects. The block diagram of the complete test bed is depicted in Figure 5.1. As it can be seen in the figure, the first five channels are employed to collect five different high power signals to be combined and directed to the device under test (DUT), while the sixth channel will filter the PIM generated by the DUT. The low-pass filters connected to channels 1 to 5 are employed to clean the output of the amplifier used to generate the high power signals, before being introduced to the multiplexer, in order to increase the spurious rejection of the whole device. The high-pass filter connected to the PIM collector channel removes the undesired low frequency signals that the multiplexer can not totally eliminate.

5.3 Design Specifications

5.3.1 Frequency Specifications

The center frequencies and bandwidths of the multiplexer are detailed in Table 5.1, where f_1 refers to the lower frequency of the band, f_2 is the upper frequency, f_0 is the center frequency of the channel, and BW refers to the frequency bandwidth. The

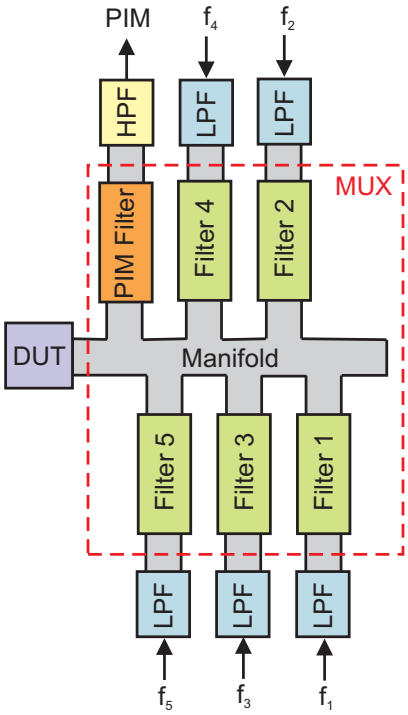

Figure 5.1 Block diagram of the test bed to measure PIM including a 6-channel multiplexer.

Channel	f_1 (GHz)	f_2 (GHz)	f_0 (GHz)	BW (MHz)
1	17.89	18.31	18.10	420
2	18.48	18.90	18.69	420
3	19.07	19.49	19.28	420
4	19.66	20.08	19.87	420
5	20.25	20.67	20.46	420
6	22.70	24.10	23.40	1400

Table 5.1 Frequency plan of the wideband 6-channel multiplexer.

first five channels have a bandwidth of 420 MHz, and the distance between center frequencies is 590 MHz (guard bands equal to 170 MHz). The sixth channel has a wider bandwidth of 1.4 GHz, and it is placed at 2.94 GHz of the fifth channel.

5.3.2 Power and Attenuation Specifications

The designed multiplexer must comply with the following specifications related with the power handling:

- It must admit 200 W carriers at the input channels, allowing at least 2 full-power carriers (200 W each) operating simultaneously in different input channels.
- The maximum allowed attenuation between any input port and the DUT port is 2.04 dB.
- The PIM generated by the test bed should be lower than -198 dBc (or equivalently, -145 dBm).
- The attenuation between any input port and the PIM output port, in the PIM reception band, must be greater than 155 dB (for avoiding the transmission of spurious signals of the tube amplifiers to the output PIM port, considering undesired signals in the PIM reception band are lower tan -43 dBc).
- The attenuation between any input port and the PIM output port must be greater than 133 dB, in the whole transmission band (in order to produce signals in the PIM output port at transmission band lower than -80 dBm, that guarantee PIM products in the output coaxial connector below -145 dBm at PIM reception band).

5.4 Configuration of the Multiplexer and the Channel Filters

The configuration of the multiplexer to be designed is shown in Figure 5.2. As it can be seen, filters are placed in both sides of the manifold, which corresponds with the so called herringbone configuration. The common port will be the one in which the DUT will be connected.

During this work, different multiplexer configurations were tested. Due to the very stringent requirements in terms of manufacturing tolerances, the final choice (shown in Figure 5.2) was the most robust one in such terms. Note that this particular solution locates the PIM reception filter close to the DUT (common) port, thus favoring the reception of the weak PIM reflected signal.

For channels 1 to 5, a new filter configuration with rectangular waveguides has been employed [13]. These filters are called hybrid folded rectangular-waveguide (HFRW) filters, and are composed of a series of cascaded trisections, where each trisection is formed by three rectangular waveguides. Figure 5.3 shows a trisection in which only the adjacent waveguides are connected (no cross-couplings).

These structures provide responses with transmission zeros (TZ) in arbitrary positions. Each trisection is responsible of a single TZ, which is accomplished by the second resonator, thanks to the stub placed next to one of its coupling irises. Inside this resonator, the signal has two possible paths (see Figure 5.4), and the interference

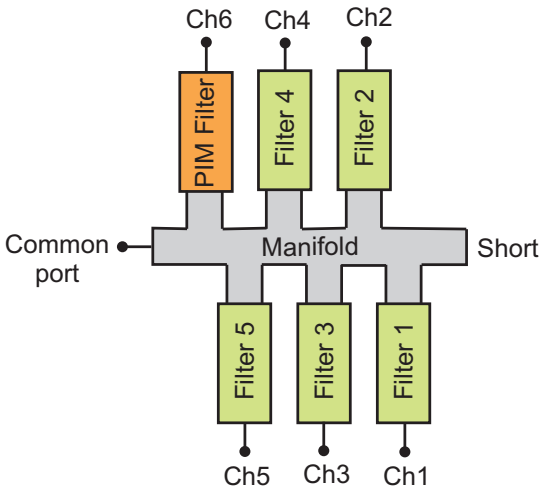

Figure 5.2 Configuration of the 6-channel manifold-coupled multiplexer.

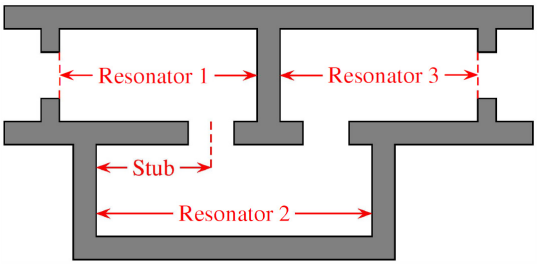

Figure 5.3 Structure of a single trisection of the HFRW filters.

between these paths creates a TZ at the frequency at which the stub is 90^o long (i.e. the frequency shift between the two paths is 180^o).

In this case, for channel filters 1 to 5, 4-cavity HFRW filters with TE_{102} resonators have been used, which are composed of two cascaded trisections. Their structure can be seen in Figure 5.5, and their frequency response has 4 poles and can accommodate 2 asymmetric transmission zeros.

For the sixth channel, a different filter configuration has been used. In this case, a classic in-line rectangular-waveguide filter with 5 cavities (5 poles) and capacitive irises has been employed, whose structure is shown in Figure 5.6.

5.5 Design Procedure

The design method employed for the multiplexer here considered is slightly different than the one proposed in chapter 4. The technique explained in the previous

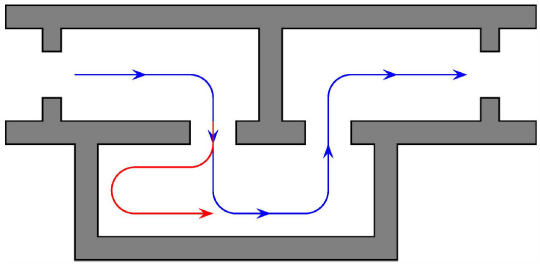

Figure 5.4 Signal paths withing the trisection of Figure 5.3. The blue line shows the main path, while the red line shows the secondary path producing the TZ at the frequency at which the stub is 90° long.

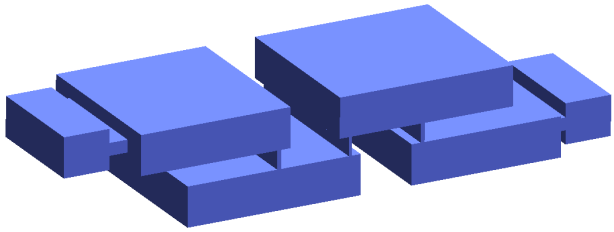

Figure 5.5 Structure of the HFRW filters employed for channels 1 to 5.

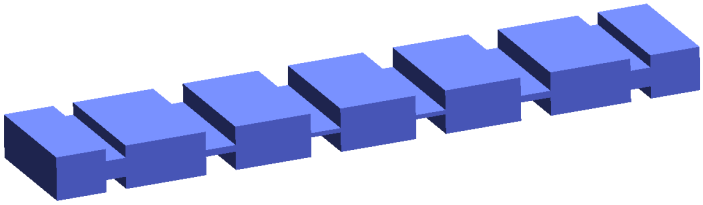

Figure 5.6 Structure of the in-line rectangular-waveguide filter with capacitive irises employed for the PIM channel.

chapter is valid for multiplexers with moderate bandwidths, in which the waveguide sections connected to the T-junctions are long, and a distributed model considering only propagating modes is normally accurate enough.

However, as the multiplexer bandwidth increases, the problems associated with the manifold spurious gain importance [14]. The way to minimize these problems is to maintain the manifold lengths, and also the stub lengths for connecting the filters to the manifold, as short as possible. Nevertheless, if the lengths of the transmission lines connected to the T-junctions are very small, a new problem arises. The high-order EM modes generated in each step (T-junctions and input irises of the channel filters) are not totally attenuated, and they reach the next step. This means that if the

distributed model only considers the propagating modes, some important information gets lost, which would lead to a deficient starting point when the EM model is obtained from the distributed model.

A classic distributed model, as the one employed in chapter 4, is essentially equivalent to what is provided by a modal-based analysis tool considering only the propagating modes of the waveguide sections as accessible modes. For a broadband multiplexer this is not good enough. However, we can extend this model by simply increasing the number of included accessible modes. Normally, considering just very few modes, we will be able to build a low-order EM model, which gathers up all the needed first-order information while maintaining low CPU computational efforts.

Therefore, the design procedure for this particular multiplexer starts with the synthesis of a low-order EM model of the whole structure. Once the previous model complies with the specifications, the number of EM modes is significantly increased in order to obtain a more accurate approach. The whole procedure is going to be thoroughly explained along the present section.

5.5.1 Design of the Low-Order EM Model

The first step is to obtain an initial EM model of the multiplexer with a low number of EM modes. This model will be employed to perform an initial optimization in which a large number of simulations are going to be required. One of the advantages of low-order EM models is the flexibility of choosing a suitable trade-off between model accuracy and simulation time for a particular structure. In our case, we found that a low-order EM model with up to 5 accessible modes provides a fair level of accuracy and is also very fast.

5.5.1.1 Design of the Individual Channel Filters First of all, the six individual channel filters are designed to have an ideal response. At this point, the filters are considered isolated (i.e. as if they were not connected to the manifold). The channel filters 1 to 5 are designed employing an equivalent distributed model, whose structure is shown in Figure 5.7. The procedure to obtain the inverter values and the lengths of the transmission lines of the distributed model can be found in [13]. The physical dimensions of the filters are calculated by means of the distributed model, following a design procedure similar to the one described in section 2.4.

Once the initial dimensions of the individual filters have been obtained, their EM models provide the responses shown in Figure 5.8. The channel filters 1 to 5 have been designed to have their two transmission zeros placed inside the PIM band, in order to achieve a better isolation between the transmission channels and the PIM band. The transmission responses of all the individual channels have been represented separately in Figure 5.9, where the transmission zeros of channels 1 to 5 can be appreciated.

5.5.1.2 Initialization of the Manifold Transmission Lines As it is said in [8, 15], and as it was also explained in chapter 4, for E-plane multiplexers, the initial length of all the transmission lines in the manifold (between T-junctions and between the last

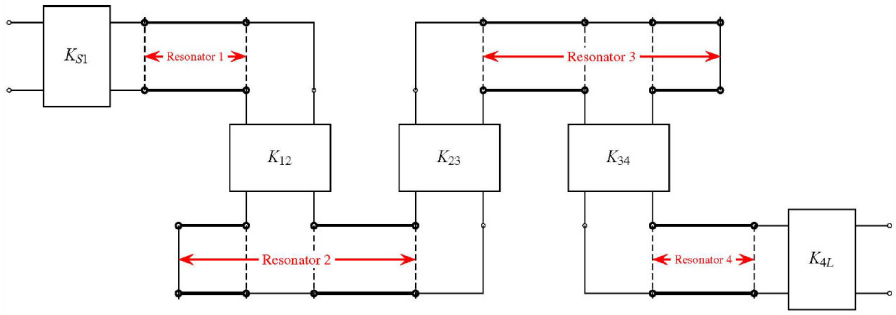

Figure 5.7 Structure of the equivalent distributed model of the HFRW filters employed for channels 1 to 5.

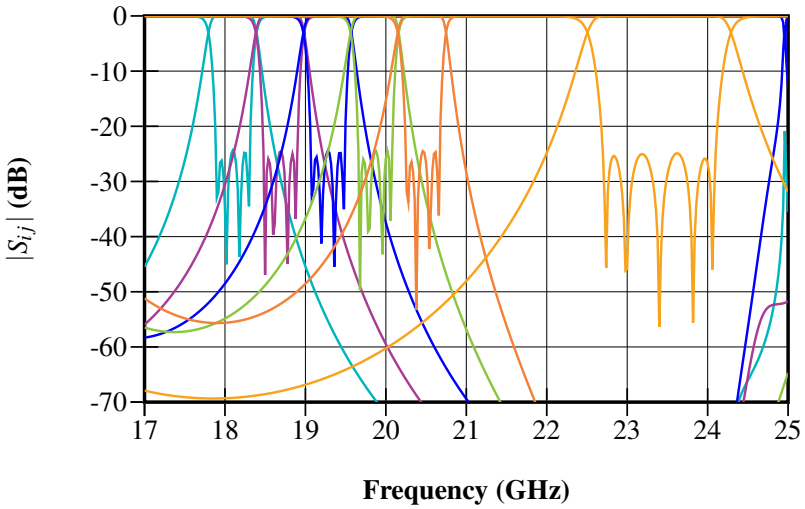

Figure 5.8 Response of the individual channel filters in the multiplexer before being connected to the manifold.

T-junction and the short circuit), as well as the stubs connecting the manifold with the filters, should be set at $m\lambda_g/2$. The value of m is normally set to 1 to achieve a more compact design. However, in multiplexers with very wide bandwidth, like it is the case here considered, a length of $\lambda_g/2$ is too much, since it usually generates a large number of spurious modes inside the multiplexer bandwidth, which are then very difficult (or even impossible) to remove during the optimization process.

In order to minimize the spurious modes, one possible solution could be to take a value of $m = 0$, thus obtaining the most compact design achievable. However, this option entails two other problems. First of all, if there is not enough separation between adjacent filters, they can touch each other and the design could be unfeasible. Furthermore, choosing an initial length of the transmission lines equal to zero makes

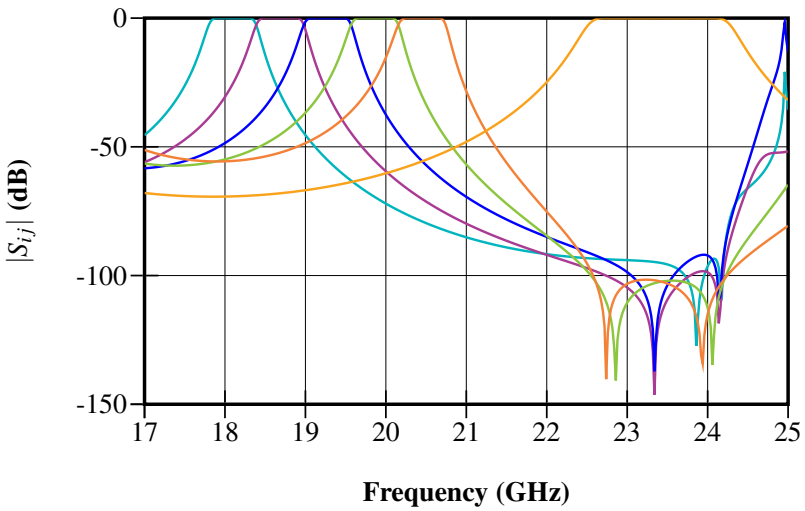

Figure 5.9 Response of the individual channel filters in the multiplexer with the transmission zeros placed inside the PIM band.

the optimization process more difficult (or even impossible), since such variable will not be able to take lower values. Therefore, the optimum solution is to choose the values of the initial lengths of the waveguide sections to be close to the suggested values of $m\lambda_g/2$ (with $m = 0$), but slightly bigger than zero, in order to allow an efficient optimization. In this case, a length of 2 mm (approximately $\lambda_g/10$) has been chosen for both the manifold sections and the stubs.

With the individually designed channel filters, and all the manifold waveguides initialized at 2 mm, the initial response of the low-order EM model of the multiplexer is the one shown in Figure 5.10. As it can be seen, the initial response is quite far away from the desired one.

5.5.1.3 Optimization of the Low-Order EM Model The next step is to perform an optimization of the EM model with a reduced number of accessible modes. It is made step by step, following the algorithm explained in section 4.2.2 (first the transmission lines and then the first parameters of each filter). In the end, a response like the one shown in Figure 5.11 is obtained.

A tolerance analysis was carried out, and the lobes of the filters which resulted to be more sensitive to manufacturing tolerances were designed with lower return loss levels, in order to ensure a proper manufactured multiplexer. This is the reason why, as it can be appreciated in Figure 5.11, the channel filters are not exactly equi-ripple. The design goal was attaining a return loss better than 20 dB in the manufactured component.

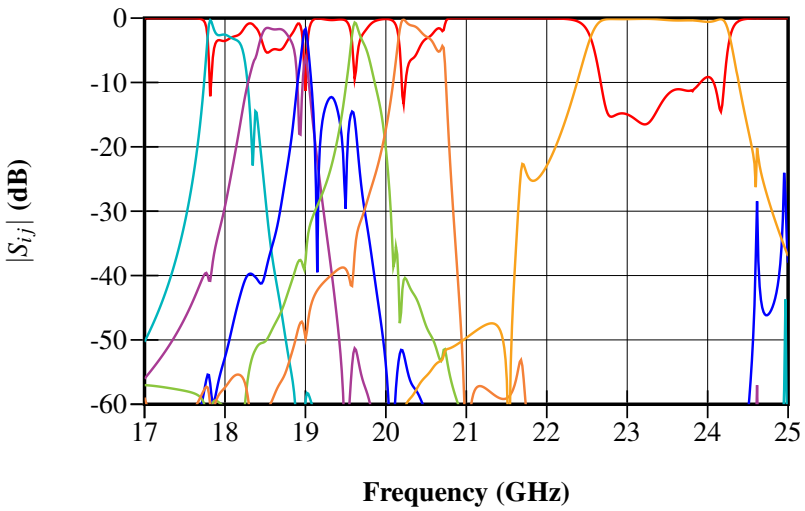

Figure 5.10 Response of the initial low-order EM model of the multiplexer before the optimization.

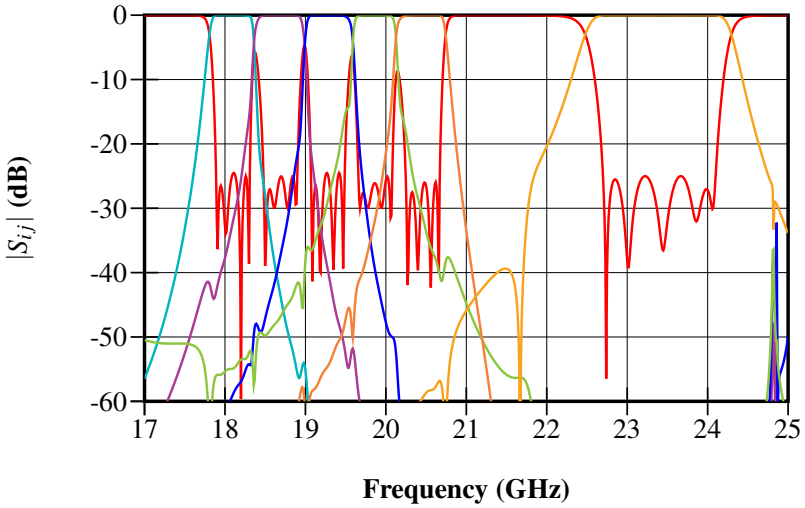

Figure 5.11 Response of the low-order EM model of the multiplexer after the optimization process.

5.5.2 Obtaining the Full-Wave EM Model

Once the low-order EM model provides an adequate response, the number of EM modes in the structure is significantly increased in order to guarantee an accurate

full-wave simulation of the real multiplexer. The response of the initial full-wave EM model is shown in Figure 5.12.

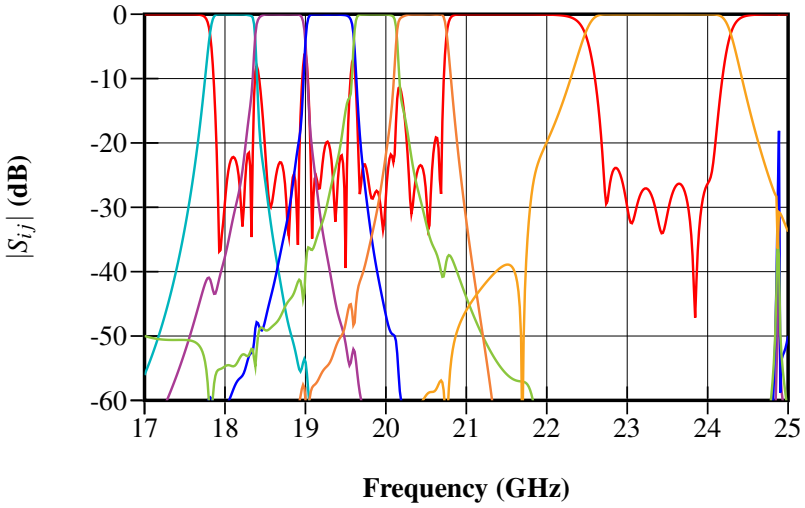

Figure 5.12 Response of the initial full-wave EM model of the multiplexer.

It can be seen that the deterioration of the response shown in Figure 5.12 is not very important. However, the simulation time of the full-wave EM model was more than 100 times higher than the low-order EM model. This proves that, with a proper choice of the number of modes in the low-order distributed model, all the relevant information can be included without paying the cost of very expensive model simulations.

The final step is to perform a last optimization of the full-wave EM model, following the procedure explained in section 4.2.2. In this case, the multiplexer is simulated with the high-pass filter (consisting on a simple bent rectangular waveguide section with reduced width) connected to the sixth channel filter, in order to take its effect into account. Even though the optimization is done with a full-wave EM model, it is indeed quite fast, since the starting point is very close to the desired response, and the number of EM iterations was therefore very low. The final full-wave EM response of the optimized structure can be seen in Figure 5.13.

As it can be seen in Figure 5.14, the response shows a perfect isolation between all the input ports and the PIM output port in the whole transmission band, which exceeds 210 dB (the minimum specified value was 133 dB). There is also a very good isolation between the input channels and the DUT port, in the PIM reception band (see figure 5.15). This attenuation should be better than 155 dB, and only the multiplexer filters provide at least 105 dB of rejection. The remaining rejection will be provided by the low-pass filters connected between the amplifiers and the multiplexer input ports.

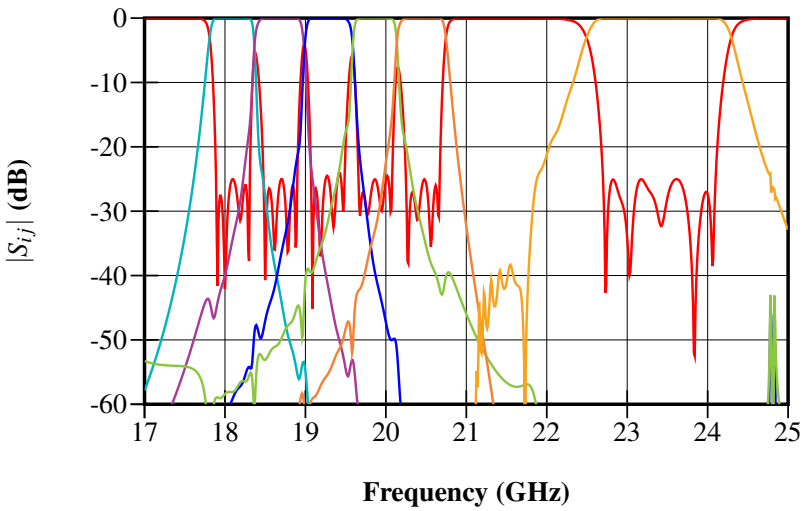

Figure 5.13 Optimized response of the full-wave EM model of the multiplexer with a high-pass filter connected to the output of the sixth channel filter.

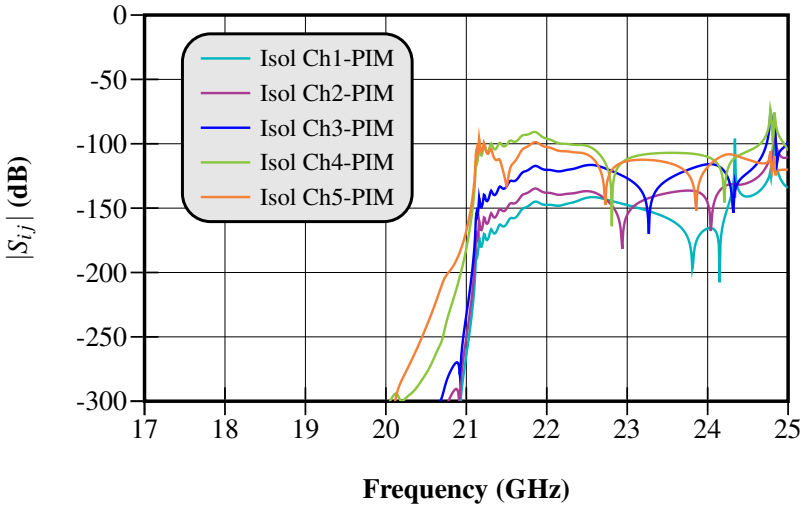

Figure 5.14 Isolation between the input ports and the PIM output port of the full-wave EM model of the multiplexer with a high-pass filter.

The finally designed structure is shown in Figure 5.16. It can be observed that some of the channel filters have been bent to reduce the overall size and the layout of the component, and simultaneously allow a proper arrangement of the channel filters, providing enough separation for thermal performance.

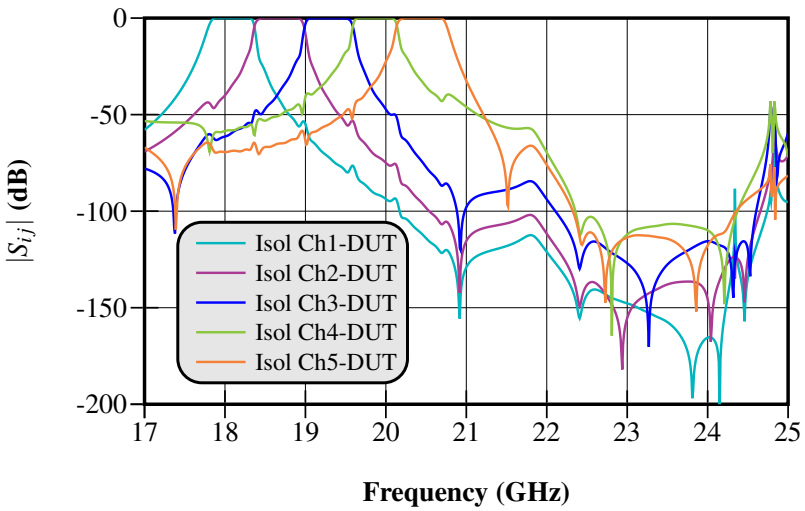

Figure 5.15 Isolation between the input ports and the DUT port of the full-wave EM model of the multiplexer with a high-pass filter.

5.6 Pre-Manufacturing Tests

In order to guarantee a proper fabricated prototype, a series of tests have been performed, including the fabrication of a simple prototype (an individual channel filter) with different materials, tolerance analyses, simulation of the insertion losses, simulations with a different EM solver, and computation of the expected values of EM fields inside the structure. The results obtained are detailed below.

5.6.1 Material Choice

Two possible materials were considered for manufacturing the K-band PIM test bed, bare aluminum and aluminum with silver coating. For the two options, the 6082 aluminum alloy was chosen since it provides the best grade against corrosion, good machining performance and an excellent conductivity for an aluminum alloy ($\sigma = 2.6 \times 10^7$ S/m at DC). This aluminum can be coated with a silver plating to improve conductivity (silver is the metal with the highest conductivity at DC, $\sigma = 6.3 \times 10^7$ S/m), although the manufacturing accuracy is decreased since the imperfections of the plating process should be added to the aluminum manufacturing tolerances.

In order to be able to determine the best material for the multiplexer, a test component, corresponding with the fifth channel filter, was manufactured in both bare aluminum and aluminum with silver plating. The measured responses of the two fabricated filters are shown in Figure 5.17. As it can be seen, the performance of the silver plating in terms of manufacturing tolerances is clearly worse. Although the return loss is reduced to 21 dB (an acceptable and expected value), there are severe

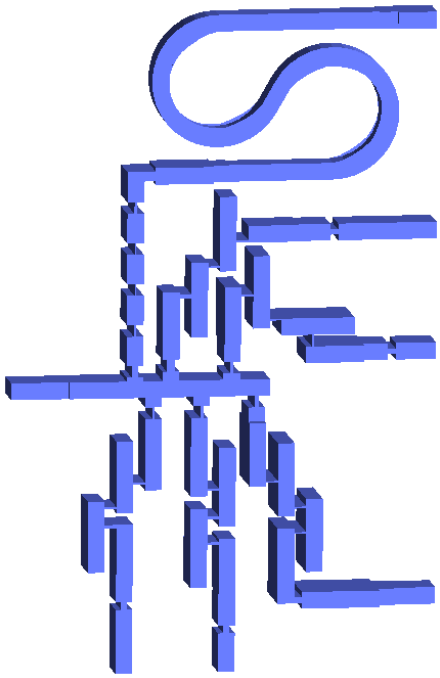

Figure 5.16 Structure of the designed wideband 6-channel manifold multiplexer with a high-pass filter connected to the sixth channel filter.

changes in the frequency response (frequency shift of 30 MHz with an increase in the passband width of about 24 MHz). On the other hand, the filter manufactured in bare aluminum has a clearly better performance, since the central frequency is only shifted 14 MHz with a bandwidth increment of about 7 MHz.

A simulated test was carried out to calculate the approximate manufacturing tolerances with the two materials. An optimization of the ideal designed filter prototype was performed, in order to match each measured response, and the resulting variations in the filter dimensions were attributed to the manufacturing deviations. However, since not all the physical dimensions were included in the optimization process (only one per resonator or coupling), the obtained values can be higher than the real tolerances (deviations occur in all the existing dimensions). Nevertheless, these calculated values can serve us to estimate the order of the real manufacturing tolerances.

In the case of the bare aluminum, the average value of the variation in the dimensions, after the optimization, was of ± 14.7 μm, while for the aluminum with silver plating, a variation of ± 21.3 μm was obtained. The previous average variations correspond to a manufacturing tolerance of about ± 7 μm for bare aluminum, and ± 10 μm for coated aluminum.

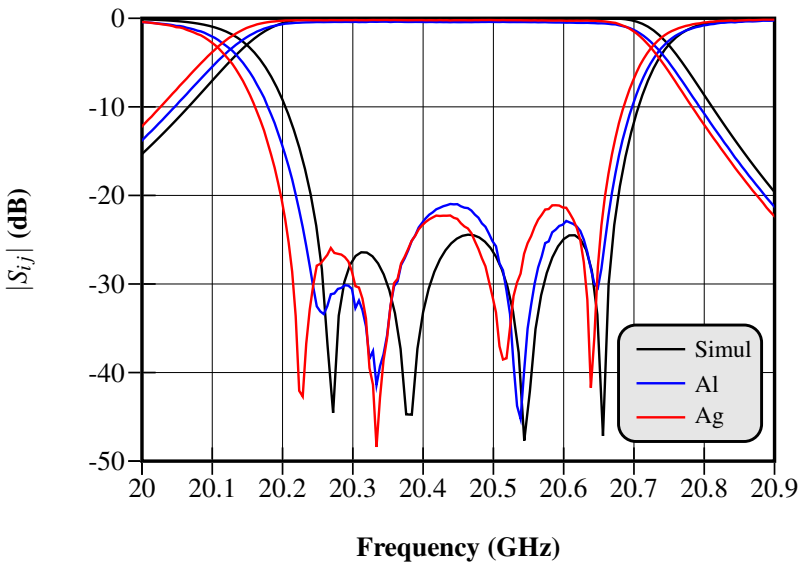

Figure 5.17 Measured responses of the two manufactured components in bare aluminum and aluminum with silver plating.

Taking into account that manufacturing tolerances increase with the distance to the central point of the manufactured structure, and that the multiplexer will be a component much larger than an isolated filter, silver plating is not a suitable option for this multiplexer (which in addition will be more sensitive than an isolated filter). On the other hand, and although the measured conductivity of aluminum is one third of the conductivity of the silver plating, the specification regarding the total losses between any input port and the DUT port is not compromised. Therefore, the final choice was the use of bare aluminum 6082.

5.6.2 Tolerance Analysis

A tolerance analysis was also performed over the whole multiplexer in order to guarantee that the manufacturing tolerances were not going to lead to a fabricated device with a deficient response. A Monte Carlo analysis was carried out using a Gaussian distribution with 4 μm standard deviation in all the design variables. This choice represents an approximate maximum tolerance of ± 8 μm after discarding very bad simulations corresponding to an unrealistic variation of a particular design variable (a Gaussian distribution is unbounded). The results obtained are shown in Figure 5.18. As it can be seen, the maximum values of the return loss level of all the channel filters are approximately homogeneous and they are below 20 dB. In addition, the frequency shift of the channels is not very important (around 10-20 MHz), and all the response lobes are clearly distinguishable. This analysis shows the robustness

Channel	IL_{min} (dB)	$BW_{IL<0.7dB}$ (MHz)
1	0.46	390
2	0.48	420
3	0.51	410
4	0.45	400
5	0.46	410
6	0.51	1400

Table 5.2 Simulated insertion losses in the designed multiplexer.

against manufacturing tolerances of the designed multiplexer. An unsatisfactory frequency response of the manufactured component is rather unlikely.

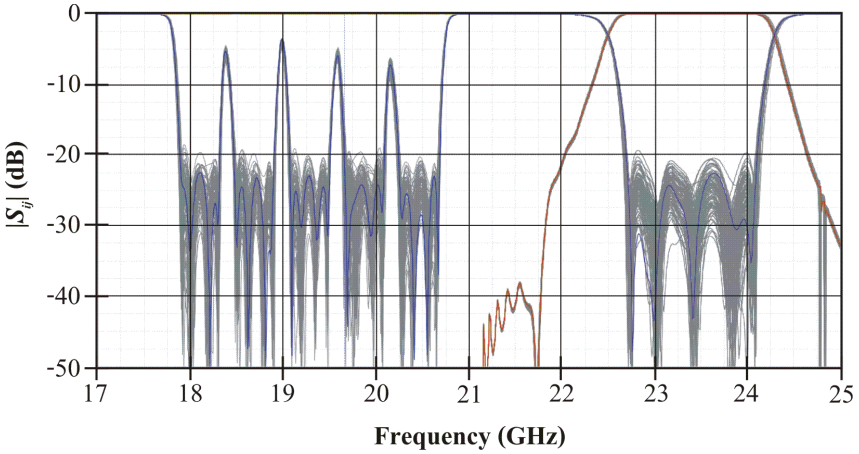

Figure 5.18 Results of the tolerance analysis performed over the final multiplexer, considering a typical deviation of 4 μm.

5.6.3 Insertion Losses

The multiplexer was fabricated in bare aluminum (alloy 6082), avoiding any coating, in order to minimize the manufacturing tolerances. Exploiting the knowledge of the aluminum real conductivity, it was possible to accurately simulate the expected losses of the multiplexer. The results are shown in Figure 5.19, and a summary is presented in tabulated form in Table 5.2.

The attenuation of all the input channels is lower than 0.7 dB in a "useful" passband region wider than 390 MHz. This attenuation represents a dissipation lower than 26.2 W per full-power carrier. In the PIM reception band, the attenuation does

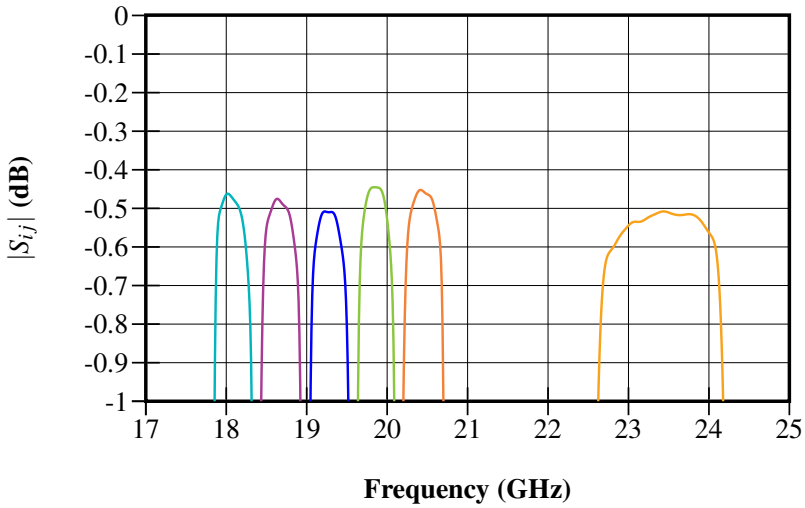

Figure 5.19 Simulated insertion losses in the 6 channels of the designed multiplexer.

not exceed 0.65 dB. These are indeed excellent figures that guarantee a total attenuation of the test bed well below the 2.04 dB specified.

5.6.4 Comparison with Other EM Solver

To ensure the accuracy of the performed EM simulations, the results obtained with FEST3D have been compared with the response provided by another reputed simulator based on a different analysis technique. Unfortunately, a simulator not based on modal methods is unable to simulate the whole structure. Therefore, the structure was decomposed in parts, and it was simulated with both FEST3D and HFSS [16]. Figures 5.20 and 5.21 show the results obtained in the part of the structure with the highest deviation, which corresponds with the fourth channel filter, and whose structure is like the one shown in Figure 5.5. As it can be seen, even in this case, there is an excellent agreement between both responses. It has also been observed that HFSS tends to converge to the FEST3D response using a finer mesh. Therefore, it is safe to affirm that the response of the designed multiplexer is accurate.

5.6.5 Power-Handling Capability

The last test was focused on the power-handling capability of the multiplexer. Since the multiplexer will not operate in a vacuum condition, the power-handling capability is limited by the dielectric breakdown EM field value of 22.8 kV/cm. The EM field of the multiplexer for a 1 W input at the common (DUT) port was computed by FEST3D at the edges and central frequency of each channel passband, and then

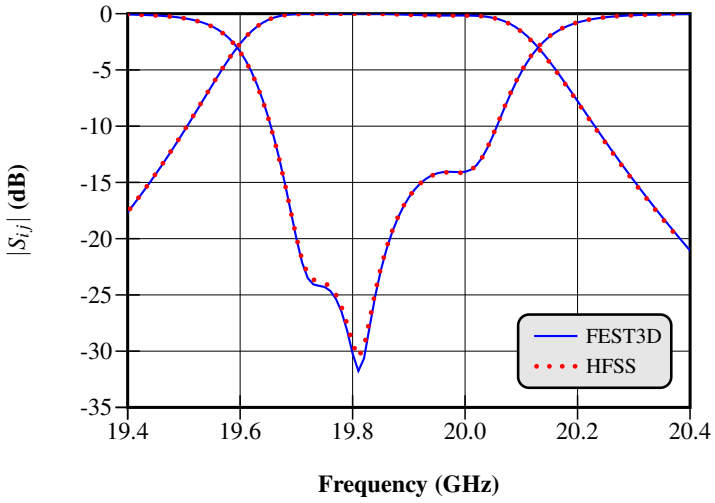

Figure 5.20 Comparison of the passband responses obtained with FEST3D and HFSS in a part of the multiplexer.

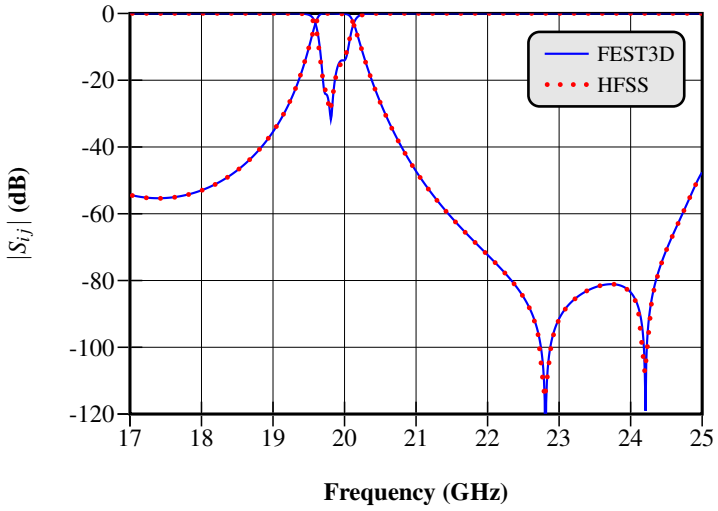

Figure 5.21 Comparison of the wideband responses obtained with FEST3D and HFSS in a part of the multiplexer.

extrapolated to a 200 W full-power carrier. Figure 5.22 plots the case where higher fields were detected.

The edges of the channel passband were always the ones providing higher EM fields (due to the peak of the group delay). On the other hand, the most dangerous zones in the structure are:

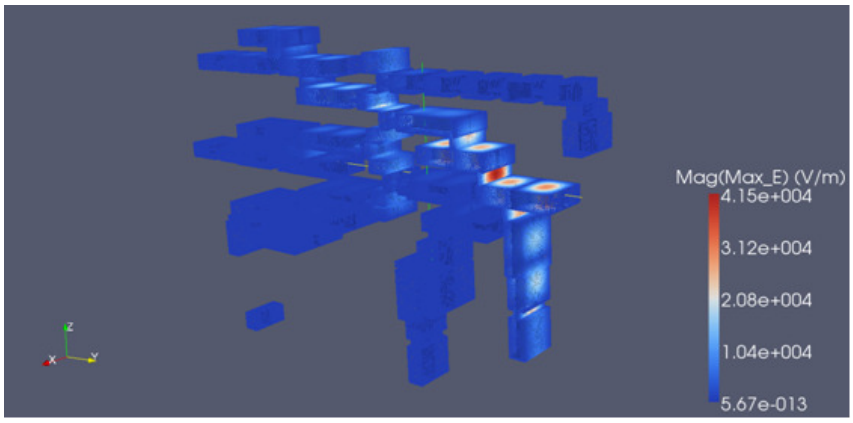

Figure 5.22 Simulated EM fields obtained in the designed multiplexer for a 1 W input power at the common port (input frequency 20.08 GHz).

- The central couplings in the channel filters 1 to 5, due to the narrow apertures required by this particular type of filters.
- The manifold transmission lines and the stubs connecting the manifold with the channel filters, since in these regions there will be an important amount of field of all the input carriers.
- The input irises of the channel filters, due to the signal of all the input carriers that has not been filtered yet.

In the case of the central couplings of the filters, the values obtained in the worst case were lower than 6 kV/cm. Taking into account that in the inner part of the filters there is only one carrier with high power (the remaining ones are attenuated at least by 10 dB), these regions of the structure are able to work with 5 carriers at full power with a good security margin.

For the input couplings and the stubs, the fields computed for a particular input carrier (at band edges, a conservative worst case) were about:

- Own channel: 5 kV/cm for carrier at ch.1, below 4 kV/cm for carrier at other channel.
- Adjacent channel: lower than 2.5 kV/cm.
- Other channel: lower than 2 kV/cm.

Therefore, for 5 input carriers operating at full-power, the maximum EM field in these particular regions will be lower than 13.5 kV/cm in any case. This figure represents a margin of about 5 dB over the maximum allowable threshold. For the specified operation with 2 full-power carriers simultaneously, the EM field will be lower than 8 kV/cm and the security margin increases to about 9 dB.

5.7 Fabrication and Measurements

5.7.1 Manufactured Device

The manufactured device (composed of the designed multiplexer plus a high-pass filter connected to the sixth channel filter) can be seen in Figure 5.23. It consist of an extremely compact solid piece, with an overall dimension of about 10×20 cm. It was designed to have all its walls of at least 3 mm, in order to prevent deformations due to heating and cooling. Finally, it has been attached to a base plate for proper fixation and to favor heat dissipation. The multiplexer was fabricated in two identical halves (clam-shell technique) to minimize the PIM generated by the component (Figure 5.23 shows one of the two halves).

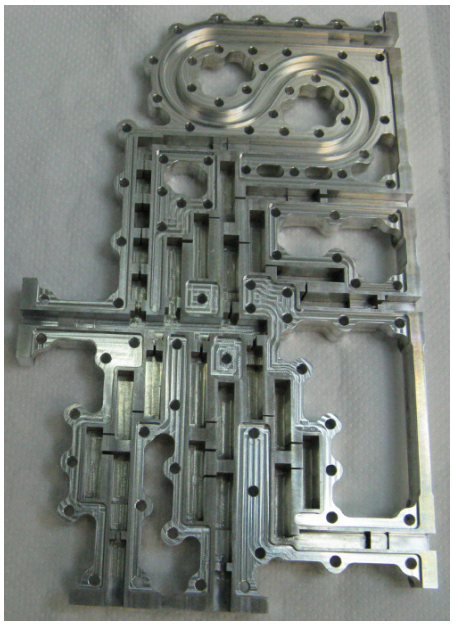

Figure 5.23 Manufactured PIM test bed with the wideband 6-channel manifold multiplexer.

5.7.2 Measurements with a Virtual Network Analyzer

The multiplexer was measured employing a virtual network analyzer (VNA), obtaining the response shown in Figure 5.24 (compare with Figure 5.13). As it can be appreciated, the final measured response is very close to the simulated one. Figure 5.25 shows the measured insertion losses of the multiplexer with more detail, where it can be appreciated that they are very similar to the ones obtained in the simulations (see Figure 5.19). Table 5.3 shows the measured values for the frequency

and bandwidth deviations of the 6 channels, their minimum return losses and also their insertion losses.

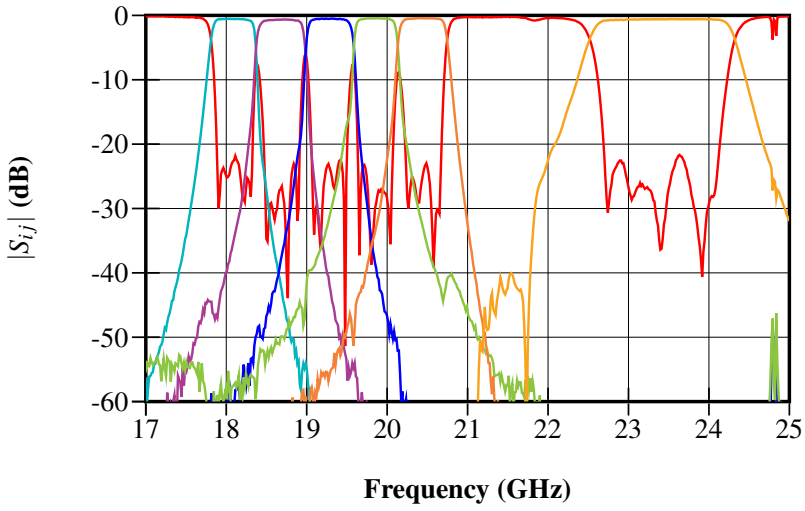

Figure 5.24 Measured response of the wideband multiplexer with a high-pass waveguide filter connected to the sixth channel filter.

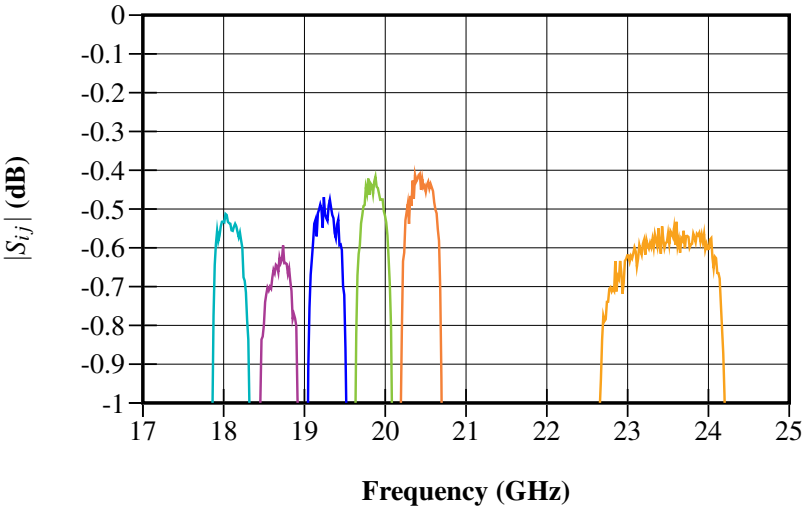

Figure 5.25 Measured insertion losses of the wideband multiplexer with a high-pass waveguide filter connected to the sixth channel filter.

Ch	Frequency deviation (MHz)	Bandwidth deviation (MHz)	RL_{min} (dB)	IL_{min} (dB)	$BW_{IL<0.8dB}$ (MHz)
1	+6	+6	22.5	0.52	430
2	+2	+10	23.0	0.62	400
3	-3	+9	22.3	0.49	440
4	-17	+3	21.6	0.44	430
5	-8	+6	23.7	0.42	480
6	+10	+16	22.4	0.57	1500

Table 5.3 Measured performance in the designed multiplexer.

Input port	Rejection MUX (dB)	Rejection MUX+LPF (dB)
1	> 135	> 220
2	> 135	> 220
3	> 115	> 200
4	> 105	> 190
5	> 110	> 195

Table 5.4 Measured rejection levels between each input port and the PIM output port, with and without including a low-pass filter connected to each input port.

5.7.3 Measurements with a Spectrum Analyzer

The attenuation between the 5 input ports and the PIM output port in the PIM reception band was measured employing an spectrum analyzer. The measurement was performed first only over the multiplexer (with the high-pass filter), and then connecting a low-pass filter to each input port. Due to the leakages in the measurement set-up, it was not possible to measure rejections greater than 135 dB. The obtained results are summarized in Table 5.4. As it can be seen, the attenuation is, at least, 35 dB (and probably more than 45 dB) greater than the specified conservative value of 155 dB.

On the other hand, the measured attenuation between all the input ports and the PIM output port is greater than 135 dB in the whole transmission band. Taking into account that the measured performance agrees with the simulation, the attenuation will probably be above 200 dB, providing a very wide margin over the specified 133 dB.

5.7.4 Power-Handling Capability

The multiplexer was used as a power combiner, by connecting 3 amplifiers to 3 of the 5 available input ports, and using the common port of the multiplexer as output port (see Figure 5.26). The total power introduced to the multiplexer was about 350 W, and the device scarcely heated up (without using any kind of cooling system). This experiment demonstrates an excellent temperature stability, thanks to an appropriate heat dissipation, which will enable the component to resist the required power levels.

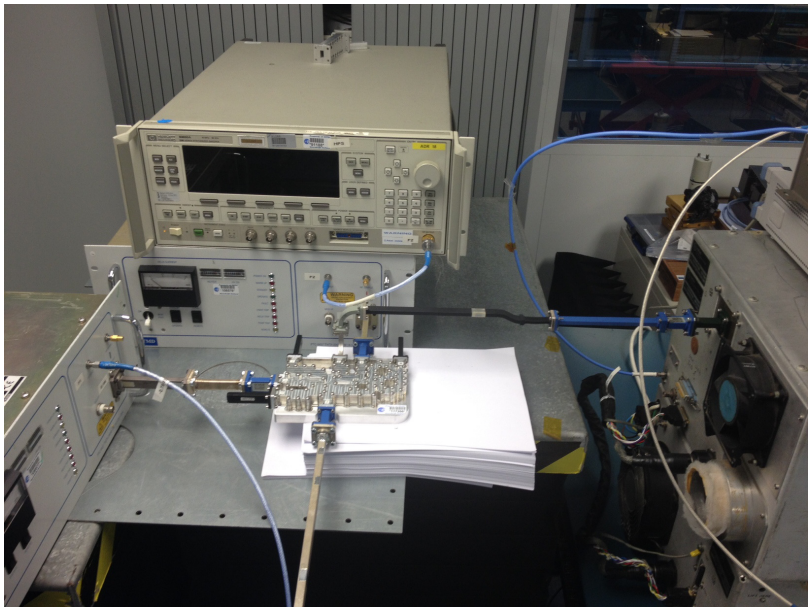

Figure 5.26 Utilization of the multiplexer as a power combiner. The observed temperature stability proved its power handling capability.

5.7.5 Final Purpose: PIM Measurements

The designed and manufactured multiplexer was conceived to measure the PIM signals generated by microwave devices. Figure 5.27 shows the multiplexer included in a test setup to analyze a horn antenna, which has been directly connected to the common port of the multiplexer. Two power amplifiers have also been connected to input ports 1 and 5 through two low-pass filters. The output port of the sixth channel must be connected to a spectrum analyzer, where it will be possible to visualize the PIM signals generated by the DUT.

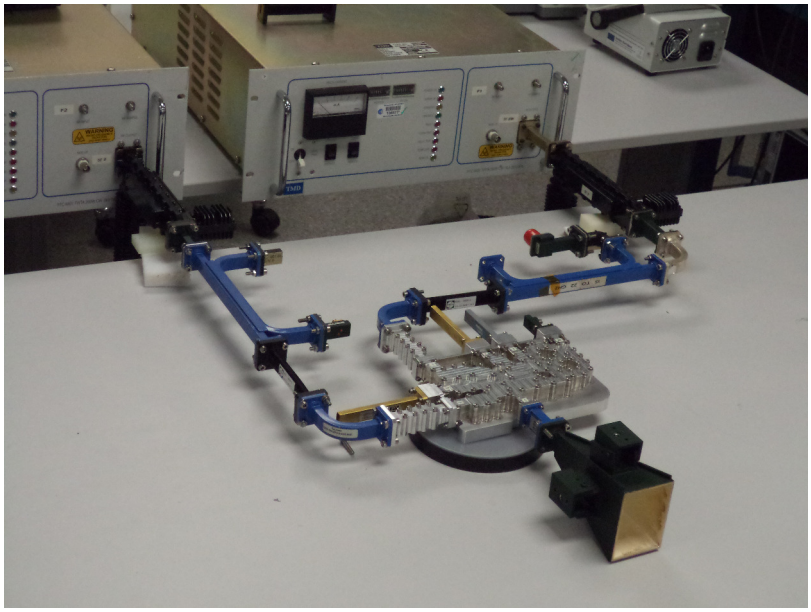

Figure 5.27 Test setup to measure PIM of a horn antenna, with two amplifiers connected to ports 1 and 5, and the DUT connected to the common port.

REFERENCES

1. European Space Agency (ESA) and Val Space Consortium (VSC) High Power RF Space Laboratory, http://www.val-space.com.
2. A.E. Atia and A.E. Williams. Narrow-bandpass waveguide filters. In *Microwave Theory and Techniques, IEEE Transactions on*, volume 20, pages 258–265, Apr 1972.
3. A.E. Atia. Computer-aided design of waveguide multiplexer (short papers). In *Microwave Theory and Techniques, IEEE Transactions on*, volume 22, pages 332–336, 1974.
4. L. Accatino and M. Mongiardo. Hybrid circuit-full-wave computer-aided design of a manifold multiplexers without tuning elements. In *Microwave Theory and Techniques, IEEE Transactions on*, volume 50, pages 2044–2047, 2002.
5. Y. Wang, S. Li, and M. Yu. Hybrid models for effective design and optimization of large-scale multiplexing networks. In *Microwave Theory and Techniques, IEEE Transactions on*, volume 61, pages 1839–1849, 2013.
6. D. Bariant, S. Bila, D. Baillargeat, S. Verdeyme, P. Guillon, D. Pacaud, and J.-J. Herren. Method of spurious mode compensation applied to manifold multiplexer design. In *Microwave Symposium Digest, 2002 IEEE MTT-S International*, volume 3, pages 1461–1464 vol.3, June 2002.
7. M.A. Ismail, D. Smith, A. Panariello, Y. Wang, and M. Yu. EM-based design of large-scale dielectric-resonator filters and multiplexers by space mapping. In *Microwave Theory and Techniques, IEEE Transactions on*, volume 52, pages 386–392, 2004.

8. R.J. Cameron and M. Yu. Design of manifold-coupled multiplexers. In *Microwave Magazine, IEEE*, volume 8, pages 46–59, 2007.

9. M. Yu and Y. Wang. Synthesis and beyond. In *Microwave Magazine, IEEE*, volume 12, pages 62–76, Oct 2011.

10. M.A. Ismail, Y. Wang, and M. Yu. Advanced design and optimization of large scale microwave devices. In *Microwave Symposium Digest (MTT), 2012 IEEE MTT-S International*, pages 1–3, June 2012.

11. H. Hu and K.L. Wu. A deterministic EM design technique for general waveguide dual-mode bandpass filters. In *Microwave Theory and Techniques, IEEE Transactions on*, volume 61, pages 800–807, Feb 2013.

12. H. Hu, K.L. Wu, and R.J. Cameron. A design technique for stepped circular waveguide dual-mode filters for broadband contiguous multiplexers. In *Microwave Symposium Digest (MTT), 2011 IEEE MTT-S International*, pages 1–4, June 2011.

13. S. Cogollos, P. Soto, M. Brumos, V.E. Boria, and M. Guglielmi. Novel rectangular waveguide structures for advanced filter characteristics. In *Microwave Symposium Digest, 2014 IEEE MTT-S International*, pages 1–4, June 2014.

14. H. Hu and K.L. Wu. Diagnosis and remedy of manifold spurious mode resonance in waveguide multiplexers. In *Microwave Conference Proceedings (APMC), 2011 Asia-Pacific*, pages 1570–1573, Dec 2011.

15. M. Brumos, S. Cogollos, M. Martinez, P. Soto, V.E. Boria, and M. Guglielmi. Design of waveguide manifold multiplexers with dual-mode filters using distributed models. In *Microwave Symposium (IMS), 2014 IEEE MTT-S International*, pages 1–4, June 2014.

16. ANSYS HFSS, Release 15.0. Available: www.ansys.com.

CHAPTER 6

CONCLUSIONS AND FUTURE WORK

This thesis has been focused on the design of microwave filters and multiplexers in waveguide technology. In particular, the design of the widely used circular-waveguide dual-mode (CWDM) filters has been addressed, which culminates with the creation of an automatic software tool capable of designing these kind of filters in a very efficient way. A procedure to correct manufacturing deviations in CWDM filters without tunning screws has also been proposed, which is able to achieve the required response of the filter in just a few iterations. The following step has been to develop a systematic technique to design classic manifold multiplexers with CWDM filters. Finally, this method was generalized in order to design a non-conventional wideband multiplexer based on a new type of rectangular waveguide filters.

In the present chapter, all the work carried out along this thesis is summarized and reviewed, thus highlighting the most important results obtained. The suggestions for future work provided at the end of the chapter will give an idea of some possible actions for continuing and extending the presented work.

6.1 Thesis Summary

A general introduction to the subjects considered along this thesis report was first presented in chapter 1. The definitions of microwave filters and multiplexers were given, explaining why they are so important for a wide range of communication systems. The suitability of the waveguide technology for satellite communication payloads was also justified. A particular type of waveguide filters, the CWDM filters, was explained with more detail. This chapter also reviewed the state of the art in the design of these waveguide devices.

In chapter 2, a new procedure to design CWDM filters was proposed. The design is accomplished by means of distributed models, which constitute a half-way point between the fast but imprecise analytical models, and the more accurate but costly full-wave electromagnetic (EM) models. The whole design process was described, starting from the design specifications, going through the synthesis of the lumped and distributed models, and finishing with the extraction of the physical dimensions. A very efficient automatic software tool has been developed, which is able to design CWDM filters of different orders (from 4th-order up to 12th-order), as well as topologies and frequency responses. The main features of this new design tool have been detailed in appendix A. Two design examples have been given, corresponding to a 4th-order and an 8th-order filter, providing the numerical results obtained and showing the accurate final responses achieved.

A novel technique to correct manufacturing deviations in CWDM filters was addressed in chapter 3. The proposed method avoids the inclusion of tuning screws in the filters, which are likely to cause problems when handling high power signals. Hence, the screws are replaced by fixed metal insertions that can be manufactured as independent pieces (one piece per cavity containing several insertions). The dimensions of these insertion pieces are calculated, through a space mapping (SM) technique, to compensate the errors produced in the whole structure. Starting with a fabricated filter with a deficient measured response, three SM iterations were performed, manufacturing the designed insertion pieces after each iteration. The response obtained after the third iteration was nearly perfect, which validates this correction technique.

A systematic design method for manifold multiplexers with CWDM filters was proposed in chapter 4. As it was done before for the individual filters, this technique makes use of distributed models of both the channel filters and the manifold waveguides. After synthesizing the lumped model of all the isolated filters, an initial model of the multiplexer is created, which needs to be optimized to achieve the required response. The optimized channel filters are then transformed into their corresponding distributed models, and the obtained multiplexer model is employed to extract the EM model (physical dimensions) of the whole device. The main advantage of the proposed technique is that most of the simulations are performed in the first design stages over circuit models, instead of EM models, which significantly reduces the execution times. Furthermore, thanks to the capability of the distributed models to accurately represent the real structures, the initial EM model obtained

with this design method already provides a very good response, and just a slight final optimization (of real dimensions) is enough to achieve the required one.

In chapter 5, the design of a wideband multiplexer with a novel type of rectangular waveguide filters has been addressed. The procedure explained in the previous chapter has been extended in order to be employed for the design of this non-conventional multiplexer. Due to the wide bandwidth of the device, the problems associated with the spurious EM modes gain importance, since they are likely to appear inside the considered bandwidth, thus significantly deteriorating the multiplexer response. One way to minimize the number of spurious modes is to maintain the lengths of the manifold waveguides as short as possible, but now, the non-propagating EM modes must be taken into account in the equivalent models, in order to properly represent the behavior of the real structure. The multiplexer was designed as part of a test bed to measure passive intermodulation effects in a high power facility. The technique employed to design this complex multiplexer has been thoroughly explained, as well as the multiple pre-manufacturing tests realized to assure the correct operation of the fabricated prototype. The excellent measured results fully validate the proposed design procedure.

6.2 Recommendation for Future Work

Although the different tasks carried out in this thesis have been successfully completed, there are still some further extensions and improvements that can be done. Some suggestions for continuing and improving the work are given below.

6.2.1 Application of the Design Methods to Other Filter Structures

The design procedures employing distributed models presented in chapters 2 and 4 have been particularized for CWDM filters. Nevertheless, they could be easily extended to other filter structures, as well as multiplexers containing other types of channel filters. The initial step should be to obtain the equivalent distributed model of each considered filter structure and, after that, the design procedure would be essentially the same as the one here presented.

6.2.2 Application of the Correction Technique to Other Filter Structures

The technique proposed for correcting manufacturing deviations in CWDM filters could also be applied to other filter structures (i.e. inductively coupled rectangular waveguide filter, or E-plane filters), which traditionally make use of tuning screws, and where they can be replaced by fixed metal insertions that can be manufactured in separated pieces. In this case, the correction procedure would be the same one proposed in this work, regardless of the particular filter considered.

6.2.3 Correction of Manufacturing Deviations in Multiplexers

The correction technique could also be extended to entire multiplexers whose channel filters commonly have tunning screws. The first step in the procedure would be to measure the response of all the channel filters independently (they should be fabricated as independent parts of the structure that can be easily separated from the manifold). Then, the measured response of each filter should be matched with the full-wave EM simulator by only changing the insertion penetrations. A final optimization of the whole structure (where the insertions are the only tuning parameters) could also be done to match the measured response of the whole multiplexer. Finally, the penetrations of the new insertion pieces of all channel filters would be calculated, filter by filter, through the space mapping algorithm. As it happened for the individual filters, more than one iteration may be required.

6.2.4 Automation of the Multiplexer Design Procedure

Although the technique here presented allows to design waveguide manifold multiplexers in a systematic and very efficient way, it still needs of a skilled person to carry out the different steps in the procedure. Nevertheless, as it was done before for the individual filters, the whole process may be fully automated. In this case, the automation of the stages related with the design of the channel filters (i.e. synthesis of the lumped and distributed models of the filters, and calculation of their physical dimensions) would not be very different as for the isolated filters. However, even though the final optimization of the EM model could be left to be performed by an expert user, the intermediate optimization process of the circuit model of the multiplexer should be automatically done (otherwise, the whole design process would be divided into two stages, between which the user would have to perform a manual optimization). Because of that, an also due to the huge number of steps and parameters to be considered in the process, this is probably the most complicated task here suggested for future implementation. Nevertheless, given the great importance of these devices for the industry, the obtained reward might worth the effort.

APPENDIX A

AN AUTOMATIC SOFTWARE TOOL TO DESIGN CWDM FILTERS

A software tool for the automatic design of circular-waveguide dual-mode (CWDM) filters has been developed. It is based on the design procedure described in chapter 2. The design process is completely automatic, and therefore, the user only has to enter the filter specifications, and the tool will be able to provide the required physical dimensions to be fabricated. This design tool is also very versatile, being capable of designing filters with different orders and configurations, and it has been successfully included in the commercial electromagnetic (EM) simulation software tool FEST3D.

A.1 Design Capabilities

The design tool has been developed to consider a great number of possible filter designs, so it is able to satisfy most of the practical cases. The design parameters that can be configured are listed below, together with the different possibilities that they exhibit.

- **Order.** The tool allows the design of CWDM filters with orders 4, 5, 6, 8, 10 and 12. Considering these orders almost all the practical cases are covered, since it is very difficult to find CWDM filters with higher orders.
- **Frequency response.** The frequency response of the filter is fully configurable. It is possible to choose the center frequency of the filter, its bandwidth, the frequencies of the transmission zeros, and the return loss. Nevertheless, only symmetric responses have been considered.
- **Topology.** For eight-pole and twelve-pole filters, it is possible to choose between two different topologies: symmetric or asymmetric. The first one leads to a solution with a symmetric structure, in which all the inner irises are cross-shaped. In the second solution, there are no symmetries in the structure, and some of the cruciform irises are replaced by horizontal rectangular irises. The second option has the advantage of making the tuning process easier.
- **Resonant mode.** It is possible to choose the resonant mode inside the circular cavities of the filter between TE_{111}, TE_{112}, TE_{113}, TE_{114} and TE_{115}. The third number employed to name the mode refers to the number of half wavelengths inside each cavity. The bigger this number is, the greater the quality factor, and the longer the filter will be. Besides, since the screws must be placed in a point where the EM field presents a maximum, depending on the chosen EM mode, they will be placed in a different position. If the EM mode is odd, they will be placed in the middle of the cavity, while if the mode is even, they will be slightly shifted to one side.
- **Equalization.** It is possible to design equalized filters, so their group delay is almost the same for all the frequencies inside the filter bandwidth. This is done by employing the so called equalization zeros, which are complex zeros that are not visible in the modulus of the frequency response. Equalization is made by searching, through a simple minimum search algorithm, the best position for those zeros to achieve a group delay as flat as possible. For a given filter order, the number of transmission zeros (employed to make the filter more selective) plus the number of equalization zeros is constant. Therefore, the bigger the number of zeros employed to equalize, the flatter the response will result, but less available transmission zeros at real frequencies will remain.
- **Geometrical parameters.** It is also possible to configure various geometry aspects, such as screw sizes and positions, iris widths and the corresponding thickness, round corners, cavity radius, or input/output ports dimensions and offset values.

A.2 Graphical User Interface

The filter design specifications are entered by means of a graphical user interface (GUI). The first window the user is going to find is shown in Figure A.1. In this window it is possible to specify the filter order, the symmetric or asymmetric topology (only in case an 8 or 12-order has been chosen) and the resonant EM mode inside the circular cavities.

Another configurable aspect is the design accuracy. This parameter will define the number of EM modes employed for the EM simulations of the different parts of the filter. Therefore, the higher the number of modes is, more exact results are going to be obtained, but higher the execution time will be. It is possible to choose between three different levels of accuracy: medium, high and very high. Assuming an ideal fabrication process (i.e. with no deviations), the fact of choosing a lower precision level would result in a manufactured prototype whose response is slightly different that the simulated one. Nevertheless, for this kind of filters, it has been proven that differences in physical dimensions obtained with the lowest accuracy level are usually much smaller than those due to manufacturing tolerances.

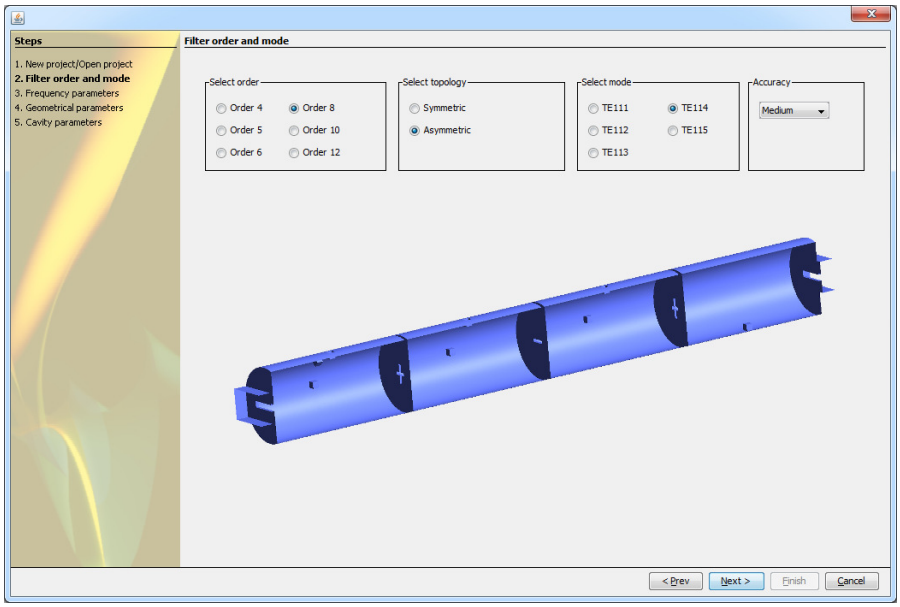

Figure A.1 GUI window for entering the filter order, the topology, the resonant EM mode and the design accuracy.

The next step is to define the frequency response characteristics in a window like the one shown in Figure A.2. The center frequency, the bandwidth and the return loss of the filter must be specified.

If equalization is required, the number of equalization zeros can be chosen, as well as the bandwidth percentage to be equalized (the smaller this bandwidth is, the flatter the group delay can be). The tool will automatically provide the optimum positions of these equalization zeros. It is also allowed to introduce the position of the equalization zeros manually, for those cases in which the user knows them.

The position of the transmission zeros must be also entered, whose number will depend on the filter order and the number of zeros employed to perform the equalization.

Once all the frequency data have been introduced, it is possible to visualize the ideal response of the filter, so the user can check whether it is appropriate, or on the contrary, proceed to change some design parameters.

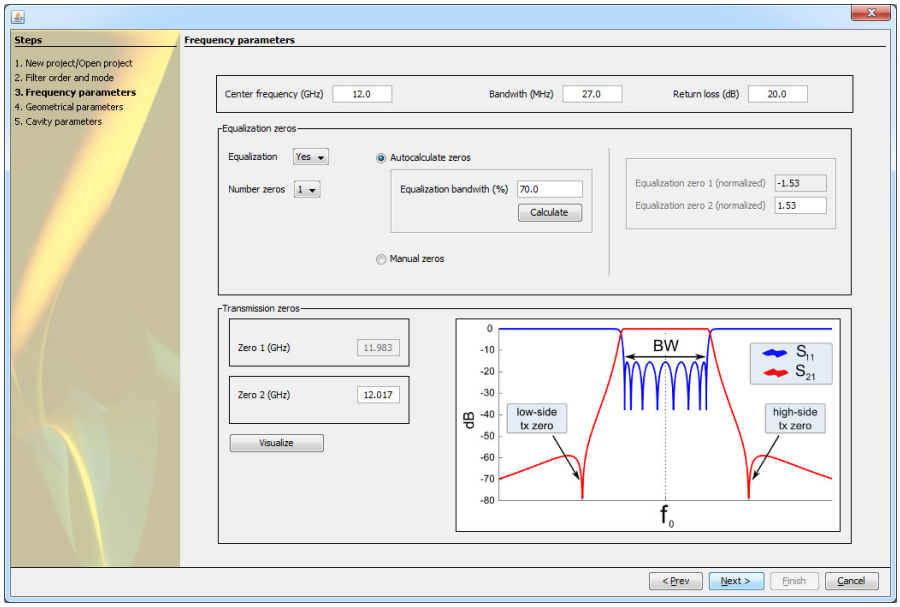

Figure A.2 GUI window for specifying the frequency response characteristics.

In the next window, whose aspect is shown in Figure A.3, it is possible to configure some geometric aspects, such as the input/output waveguides, the cavities or the irises.

One of these parameters is the cavity radius, which is a very important parameter, since the quality of the finally obtained result rely on a good choice of this value. Because of that, the tool automatically provides an optimum value for the cavity radius, which is calculated from the center frequency of the filter. Nevertheless, the user can modify this value, but if it is much smaller or much larger than the optimum one, it is likely that the result obtained will not be good.

Other parameters to be configured are the width of the irises and the corresponding thickness. It is also possible to include round corners in all the irises, thus taking

into account the radius of the drilling tool that will be employed to manufacture the filter pieces. Besides, a vertical and/or horizontal offset can be included in the input/output ports.

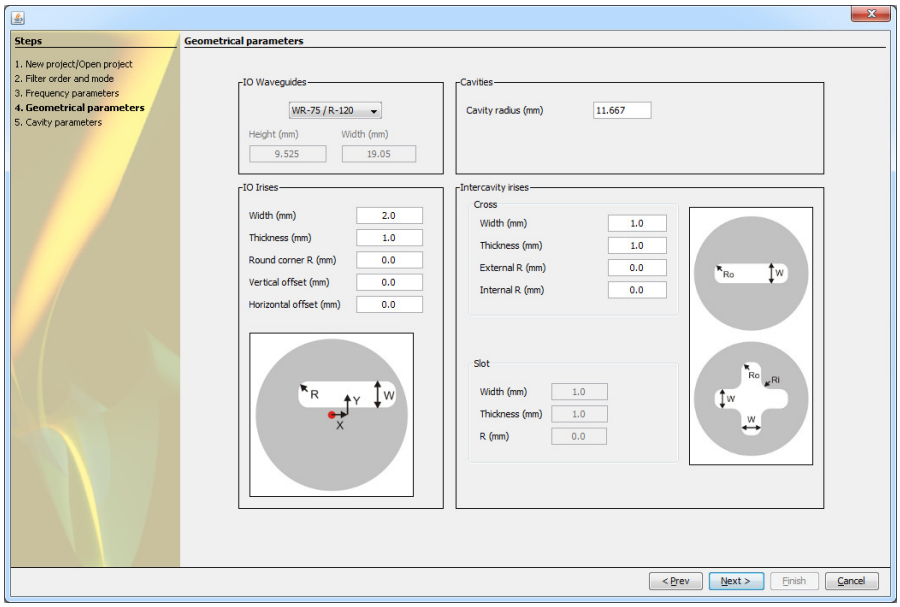

Figure A.3 GUI window for configuring the geometrical parameters.

Finally, the last GUI window is shown in Figure A.4, where it is possible to enter the thickness of the screws and the minimum length of penetration. This minimum length must be long enough to allow an appropriate tuning after the fabrication process, in order to correct manufacturing deviations. The bigger the fabrication tolerances are, the bigger this minimum length must be.

It will also be possible to specify the position of the screws (in degrees) inside each cavity. The difference in position of the oblique screws in adjacent cavities must accomplish certain conditions, so the tool will inform the user if some rule is broken.

Once all the specifications have been entered, the user will press the finish button, and the design algorithm will be executed. The physical dimensions of the required filter will be provided within a few minutes, as well as the simulated EM response in comparison with the ideal one.

A.3 Computational Efficiency

The presented automatic design algorithm for CWDM filters performs a series of steps containing loops which involves EM simulations. Each EM simulation has a certain execution time, which will depend on the simulated structure and the number

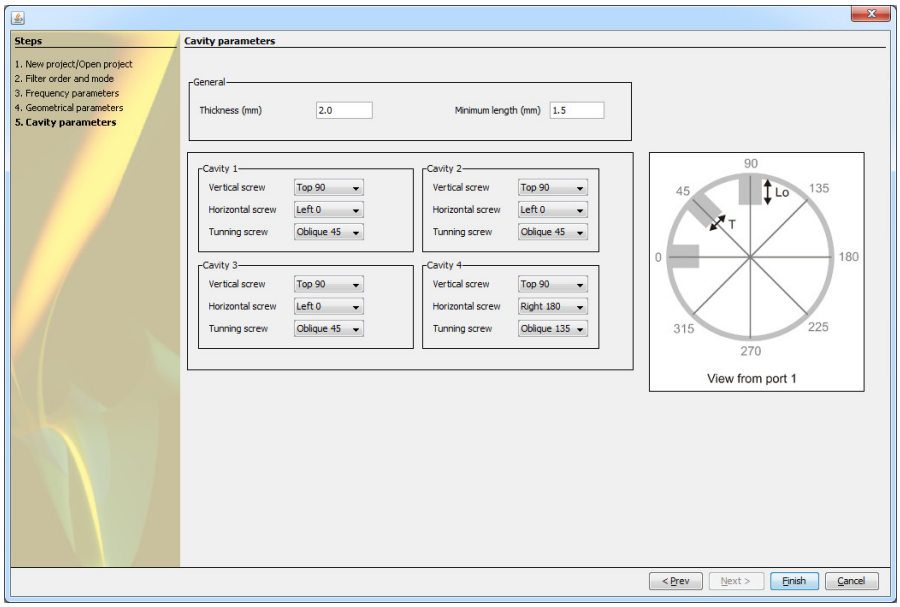

Figure A.4 GUI window for configuring the position and geometry of the screws.

Order	Execution time
4	2min 24s
8	4min 38s
12	7min 21s

Table A.1 Total execution times to design CWDM filters with different orders.

of EM modes considered (given by the selected accuracy). The total execution time will also be different depending on the filter order, because each cavity is designed separately. Therefore, the higher the filter order is, the more cavities the filter has, and the longer the execution time will be.

Table A.1 contains the execution times corresponding to three different designs, whose orders are 4, 8 and 12, respectively. All of them have been designed with medium accuracy, using a CPU with a processor AMD Phenom II X3 710 @ 2.6 GHz with 8 GB of RAM. Thanks to the great efficiency of the EM solver (FEST3D), the execution times are significantly shorter than they could be using other EM simulation solvers.

APPENDIX B

DESIGN OF DOUBLY AND SINGLY TERMINATED FILTER NETWORKS

This appendix describes the concepts of doubly and singly terminated filter networks, and explains how their transmission parameters are defined in each case. The procedure to design both types of networks is also addressed. It starts by obtaining the polynomial forms of the transfer and reflection functions. Then, the $[ABCD]$ and $[Y]$ polynomial matrices are extracted, and finally the full coupling matrix is synthesized and reduced to the canonical folded coupling matrix.

B.1 Doubly and Singly Terminated Filter Networks

B.1.1 Doubly Terminated Networks

A doubly terminated filter network has resistor terminations at both ends, which is indeed the most common case, and is valid for most of the applications. Figure B.1 shows a typical scheme of a doubly terminated network, with a source of a certain impedance connected at the input, and a load connected at its output.

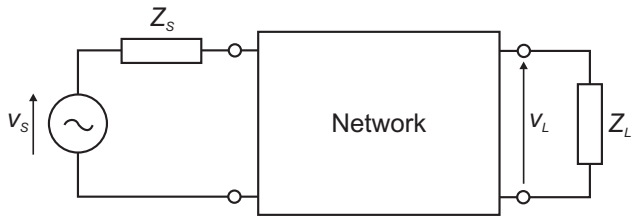

Figure B.1 Doubly terminated filter network.

Here, the power delivered to the load is

$$P_L = \frac{|v_L|^2}{R_L} \tag{B.1}$$

while the available power, or the maximum power the source can deliver to the circuit, is given by the following expression

$$P_{avail} = \frac{|v_S|^2}{4R_S} \tag{B.2}$$

In the previous equations, $R_S = \mathrm{Re}(Z_S)$ and $R_L = \mathrm{Re}(Z_L)$. By combining (B.1) and (B.2), the power transfer function, which is equivalent to the square of the transmission parameter modulus, can be written in logarithmic units as follows

$$|S_{21}|^2 = 10\log\left(\frac{P_L}{P_{avail}}\right) = 10\log\left(4\frac{R_S}{R_L}\left|\frac{v_L}{v_S}\right|^2\right) \tag{B.3}$$

B.1.2 Singly Terminated Networks

Singly terminated filter networks are designed to operate from very high or very low impedance sources. They were originally developed to synthesize networks connected to thermionic valve amplifiers, and certain transistor amplifiers with very high internal impedances. The reason why they are considered in this thesis is because they provide an input admittance response that is very appropriate for the design of contiguous-channel multiplexers.

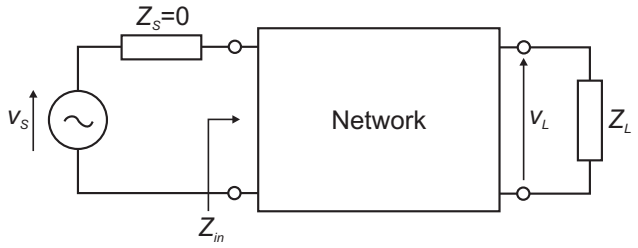

Figure B.2 Singly terminated filter network.

In singly terminated filter networks, the source impedance is equal to zero. A typical scheme of a singly terminated network has been depicted in Figure B.2.

In this case, the power transfer function defined in (B.3) does not apply since, as it can be deduced from equation (B.2), a zero impedance source has infinite available power. Hence, a new definition of the transfer function needs to be obtained, following the procedure explained in [1]. Here, the power absorbed by the circuit is

$$P_{in} = \frac{|v_S|^2}{R_{in}} \tag{B.4}$$

where $R_{in} = \mathrm{Re}(Z_{in})$, and Z_{in} is defined in Figure B.2. If a lossless network is considered, all the power is transferred to the load,

$$\frac{|v_S|^2}{R_{in}} = \frac{|v_L|^2}{R_L} \tag{B.5}$$

and therefore

$$\left|\frac{v_L}{v_S}\right| = \sqrt{\frac{R_L}{R_{in}}} \tag{B.6}$$

Finally, the transmission parameter is obtained from the voltage gain function as

$$|S_{21}| = 20\log\left|\frac{v_L}{v_S}\right| = 10\log\left(\frac{R_L}{R_{in}}\right) \tag{B.7}$$

B.2 Polynomial Forms of the Transfer and Reflection Parameters

For any two-port lossless filter network composed of a series of N coupled resonators, the transfer and reflection functions may be expressed as a ratio of two N-th degree polynomials

$$S_{11}(s) = \frac{F(s)/\varepsilon_R}{E(s)} \tag{B.8}$$

$$S_{21}(s) = \frac{P(s)/\varepsilon}{E(s)} \tag{B.9}$$

where $s = jw$ is the complex frequency variable, and ε_R and ε are normalization constants. The $E(s)$, $F(s)$ and $P(s)$ polynomials can be obtained from the filter specifications (filter order N, return loss RL and position of the transmission zeros), following the procedure described in chapter 6 of [2], and also appearing in [3], which is the same for both doubly and singly terminated networks. The previous polynomials and constants are the starting point for the synthesis of the coupling matrix.

B.3 Calculation of the $[ABCD]$ and $[Y]$ Polynomial Matrices

The next step is to obtain the short-circuit admittance parameters (or y-parameters) from the transfer/reflection polynomials. The procedure differs for the singly and doubly terminated cases and will be treated separately.

B.3.1 Doubly Terminated Networks

As it is demonstrated in chapter 7 of [2], the $[ABCD]$ matrix of a doubly terminated network can be directly expressed in terms of the coefficients of $E(s)$ and $F(s)/\varepsilon_R$ as follows

$$[ABCD] = \frac{1}{P(s)/\varepsilon} \begin{bmatrix} A(s) & B(s) \\ C(s) & D(s) \end{bmatrix} \tag{B.10}$$

The calculation of the polynomials inside the matrix is slightly different depending on whether the filter degree N is even or odd. For N even we have

$$A(s) = j\,\mathrm{Im}(e_0{+}f_0) + \mathrm{Re}(e_1{+}f_1)s + j\,\mathrm{Im}(e_2{+}f_2)s^2{+}\ldots{+}j\,\mathrm{Im}(e_N{+}f_N)s^N \tag{B.11a}$$

$$B(s) = \mathrm{Re}(e_0{+}f_0) + j\,\mathrm{Im}(e_1{+}f_1)s + \mathrm{Re}(e_2{+}f_2)s^2{+}\ldots{+}\mathrm{Re}(e_N{+}f_N)s^N \tag{B.11b}$$

$$C(s) = \mathrm{Re}(e_0{-}f_0) + j\,\mathrm{Im}(e_1{-}f_1)s + \mathrm{Re}(e_2{-}f_2)s^2{+}\ldots{+}\mathrm{Re}(e_N{-}f_N)s^N \tag{B.11c}$$

$$D(s) = j\,\mathrm{Im}(e_0{-}f_0) + \mathrm{Re}(e_1{-}f_1)s + j\,\mathrm{Im}(e_2{-}f_2)s^2{+}\ldots{+}j\,\mathrm{Im}(e_N{-}f_N)s^N \tag{B.11d}$$

while for N odd

$$A(s) = \mathrm{Re}(e_0{+}f_0) + j\,\mathrm{Im}(e_1{+}f_1)s + \mathrm{Re}(e_2{+}f_2)s^2{+}\ldots{+}j\,\mathrm{Im}(e_N{+}f_N)s^N \tag{B.12a}$$

$$B(s) = j\,\mathrm{Im}(e_0{+}f_0) + \mathrm{Re}(e_1{+}f_1)s + j\,\mathrm{Im}(e_2{+}f_2)s^2{+}\ldots{+}\mathrm{Re}(e_N{+}f_N)s^N \tag{B.12b}$$

$$C(s) = j\,\mathrm{Im}(e_0{-}f_0) + \mathrm{Re}(e_1{-}f_1)s + j\,\mathrm{Im}(e_2{-}f_2)s^2{+}\ldots{+}\mathrm{Re}(e_N{-}f_N)s^N \tag{B.12c}$$

$$D(s) = \mathrm{Re}(e_0{-}f_0) + j\,\mathrm{Im}(e_1{-}f_1)s + \mathrm{Re}(e_2{-}f_2)s^2{+}\ldots{+}j\,\mathrm{Im}(e_N{-}f_N)s^N \tag{B.12d}$$

where e_i and f_i ($i = 0, 1, ..., N$) are the complex coefficients of $E(s)$ and $F(s)/\varepsilon_R$, respectively.

Once the $[ABCD]$ matrix has been calculated, the y-parameter matrix $[Y]$ can be obtained by using the $[ABCD] \rightarrow [Y]$ conversion formula [1] as explained below

$$\begin{bmatrix} y_{11}(s) & y_{12}(s) \\ y_{21}(s) & y_{22}(s) \end{bmatrix} = \frac{1}{y_d(s)} \begin{bmatrix} y_{11n}(s) & y_{12n}(s) \\ y_{21n}(s) & y_{22n}(s) \end{bmatrix} = \frac{1}{B(s)} \begin{bmatrix} D(s) & \frac{-P(s)}{\varepsilon} \\ \frac{-P(s)}{\varepsilon} & A(s) \end{bmatrix} \tag{B.13}$$

where $y_{ijn}(s)$ ($i, j = 1, 2$) are the numerator polynomials of $y_{ij}(s)$, and $y_d(s)$ is their common denominator polynomial. Therefore, these polynomials can be calculated as indicated next

$$y_d(s) = B(s) \tag{B.14a}$$
$$y_{11n}(s) = D(s) \tag{B.14b}$$
$$y_{22n}(s) = A(s) \tag{B.14c}$$
$$y_{21n}(s) = y_{12n}(s) = \frac{-P(s)}{\varepsilon} \tag{B.14d}$$

B.3.2 Singly Terminated Networks

In this case, the procedure starts by obtaining an expression relating the $E(s)$ and $P(s)$ polynomials with the y parameters. Equation (B.7) defines the S_{21} parameter in terms of the input/output voltages, while (B.9) relates the same parameter with the $E(s)$ and $P(s)$ polynomials. On the other hand, considering a network like the one depicted in Figure B.3, the voltages and currents in the network can be related by means of the y-parameters as

$$i_1 = y_{11}v_1 + y_{12}v_2 \tag{B.15a}$$
$$i_2 = y_{21}v_1 + y_{22}v_2 \tag{B.15b}$$

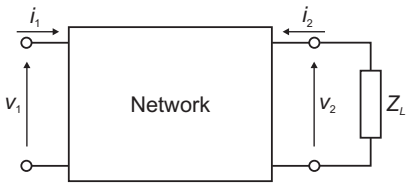

Figure B.3 Network with voltages and currents for the definition of the y-parameters.

By solving the previous system, knowing that $v_2 = -i_2 Z_L$, and renaming the voltages v_1 and v_2 by v_S and v_L, respectively, we obtain

$$\frac{v_L}{v_S} = \frac{-y_{12} Z_L}{1 + Z_L y_{22}} \tag{B.16}$$

Finally, combining (B.9) with (B.16), setting the terminating impedance $Z_L = 1\Omega$, and replacing y_{12} and y_{22} with $y_{12n}(s)/y_d(s)$ and $y_{22n}(s)/y_d(s)$, respectively, we have

$$\frac{P(s)/\varepsilon}{E(s)} = \frac{-y_{12n}(s)}{y_d(s) + y_{22n}(s)} \tag{B.17}$$

The $E(s)$ polynomial can be split into its complex-even and complex-odd components, thus obtaining

$$E(s) = m_1 + n_1 \tag{B.18}$$

where

$$m_1 = \mathrm{Re}(e_0) + j\,\mathrm{Im}(e_1)s + \mathrm{Re}(e_2)s^2 + \ldots + \mathrm{Re}(e_N)s^N \tag{B.19a}$$

$$n_1 = j\,\mathrm{Im}(e_0) + \mathrm{Re}(e_1)s + j\,\mathrm{Im}(e_2)s^2 + \ldots + j\,\mathrm{Im}(e_N)s^N \tag{B.19b}$$

Finally, substituting equation (B.19) into equation (B.17), we write

$$\frac{P(s)/\varepsilon}{m_1 + n_1} = \frac{-y_{12n}(s)}{y_d(s) + y_{22n}(s)} \tag{B.20}$$

As it is explained in [2], $E(s)$ is normalized such that its highest-degree coefficient e^N equals unity. Besides, the coefficients of $y_{12n}(s)$, $y_{22n}(s)$ and $y_d(s)$ polynomials must alternate between purely real and purely imaginary as the power of s increases, and the $y_d(s)$ polynomial must be one degree greater than $y_{22n}(s)$. As a result

$$\begin{aligned}
&\text{For } N\text{even:} && y_d(s) = m_1, && y_{22n}(s) = n_1 \\
&\text{For } N\text{odd:} && y_d(s) = n_1, && y_{22n}(s) = m_1 \\
&\text{For } N\text{even or odd:} && y_{12n}(s) = y_{21n}(s) = \frac{-P(s)}{\varepsilon}
\end{aligned} \tag{B.21}$$

Now, the $A(s)$ and $B(s)$ polynomials of the $[ABCD]$ matrix are also known, since $A(s) = y_{22n}(s)$ and $B(s) = y_d(s)$. However, it remains to find the $C(s)$ and $D(s)$ polynomials, as well as the $y_{11n}(s)$ polynomial. This is accomplished by a method due to Levy [4]. Hence, the $C(s)$ and $D(s)$ polynomials are obtained by solving the following linear system:

$$A(s)D(s) - B(s)C(s) = \left(\frac{P(s)}{\varepsilon}\right)^2 \tag{B.22}$$

The unknown $C(s)$ and $D(s)$ polynomials can be found by writing the relationship (B.22) in matrix form, and solving it with numerical methods. The detailed procedure is explained in chapter 7 of [2]. Once all the parameters of the $[ABCD]$ matrix have been extracted, the remaining numerator polynomial of the y-parameter matrix can be directly obtained as $y_{11n}(s) = D(s)$.

B.4 Synthesis of the Folded Coupling Matrix

The procedure for synthesizing the coupling matrix is the same for both doubly and singly terminated networks and, in the two cases, the starting point is the y-parameter matrix obtained in the previous sections. The method to extract the coupling matrix can be found in section 8.2 of [2].

The obtained matrix is a full matrix, whose elements are all different from zero. It means that, if this matrix is directly translated to a physical structure, all the existing resonators should be coupled with all the others. Since this is clearly impractical to be realized in most of the cases, the full matrix needs to be transformed into a more suitable topology. A more convenient form is the folded configuration [5], that can be realized directly, or can serve as the starting point for further transformations to other topologies. The process to reduce the full matrix to the folded form is explained in section 8.3 of [2]. This procedure involves a series of similarity transforms (rotations), which eliminate the unwanted coupling matrix entries.

REFERENCES

1. G.L. Matthaei, L. Young, and E.M.T. Jones. *Microwave Filters, Impedance-Matching Networks, and Coupling Structures*. Artech House. McGraw-Hill, 1964.
2. R.J. Cameron, C.M. Kudsia, and R.R. Mansour. *Microwave Filters for Communication Systems: Fundamentals, Design and Applications*. Wiley, 2007.
3. R. J. Cameron. General coupling matrix synthesis methods for chebyshev filtering functions. In *Microwave Theory and Techniques, IEEE Transactions on*, volume 47, pages 433–442, Apr 1999.
4. R. Levy. Synthesis of general asymmetric singly- and doubly-terminated cross-coupled filters. In *Microwave Theory and Techniques, IEEE Transactions on*, volume 42, pages 2468–2471, Dec 1994.
5. J.D. Rhodes. A low-pass prototype network for microwave linear phase filters. In *Microwave Theory and Techniques, IEEE Transactions on*, volume 18, pages 290–301, Jun 1970.

APPENDIX C

LIST OF PUBLICATIONS

Journal Papers

- M. Brumos, V. E. Boria, M. Guglielmi and S. Cogollos. Correction of manufacturing deviations in waveguide filters and manifold multiplexers without tuning screws. In *International Journal of Microwave and Wireless Technologies*, submitted.
- M. Brumos, S. Cogollos, P. Soto, V. E. Boria, M. Guglielmi, B. Gimeno and D. Raboso. Efficient design of waveguide manifold multiplexers based on low-order EM distributed models. In *Microwave Theory and Techniques, IEEE Transactions on*, submitted.
- S. Cogollos, M. Brumos, V. E. Boria, C. Vicente, J. Gil, B. Gimeno and M. Guglielmi. A Systematic Design Procedure of Classical Dual-Mode Circular Waveguide Filters Using an Equivalent Distributed Model. In *Microwave Theory and Techniques, IEEE Transactions on*, volume 60, pages 1006-1017, April 2012.

Conference Papers

- M. Brumos, V. E. Boria, M. Guglielmi and S. Cogollos. Correction of manufacturing deviations in circular-waveguide dual-mode filters using aggressive space mapping. In *Microwave Conference, 2014. 44th European*, pages 1-4, Oct 2014.
- M. Brumos, S. Cogollos, M. Martinez, P. Soto, V. E. Boria and M. Guglielmi. Design of waveguide manifold multiplexers with dual-mode filters using distributed models. In *Microwave Symposium Digest, 2014 IEEE MTT-S International*, pages 1-4, June 2014.
- S. Cogollos, P. Soto, M. Brumos, V. E. Boria and M. Guglielmi. Novel rectangular waveguide structures for advanced filter characteristics. In *Microwave Symposium Digest, 2014 IEEE MTT-S International*, pages 1-4, June 2014.
- M. Brumos, C. Carceller, S. Cogollos, V. E. Boria, C. Vicente, J. Gil and B. Gimeno. Diseño de filtros de microondas de modo dual en guía cuadrada y circular. In *XXVI Simposio de la Unión Científica Internacional de Radio*, Sept 2011.
- S. Cogollos, M. Brumos, V. E. Boria, C. Vicente, B. Gimeno and M. Guglielmi. New distributed model for synthesis of classical dual mode filters. In *Microwave Symposium Digest (MTT), 2010 IEEE MTT-S International*, pages 437-440, May 2010.